이학박사 학위논문

Double resonance of Raman transitions in a two-electron degenerate Fermi gas of ytterbium atoms

이터븀 페르미 양자 기체에서의 라만 전이 이중 공명

2017년 8월

서울대학교 대학원

물리 · 천문 학부

이 무 송

Double resonance of Raman transitions in a two-electron degenerate Fermi gas of ytterbium atoms

이터븀 페르미 양자 기체에서의 라만 전이 이중 공명

지도교수 신 용 일

이 논문을 이학박사 학위 논문으로 제출함

2017년 6월

서울대학교 대학원

물리 · 천문 학부

이 무 송

이무송의 박사 학위 논문을 인준함

2017년 6월

위 원 장	제 원 호	(인)
부위원장	신 용 일	(인)
위 원	안 경 원	(인)
위 원	정 현 석	(인)
위 원	이 재 훈	(인)

Double resonance of Raman transitions in a two-electron degenerate Fermi gas of ytterbium atoms

by

Moosong Lee, B.S.

Dissertation

Presented to the Faculty of the Graduate School of

Seoul National University

in Partial Fulfillment

of the Requirements

for the Degree of

Doctor of Philosophy

Seoul National University

August 2017

Abstract

Double resonance of Raman transitions in a two-electron degenerate Fermi gas of ytterbium atoms

Moosong Lee
Department of Physics and Astronomy
The Graduate School
Seoul National University

A Raman transition is a quantum mechanical phenomenon which couples two states by a two photon process accompanied by simultaneous photon absorption and emission. The usage of Raman transitions is very diverse for various purposes in physics, chemistry, biology, and engineering. Especially, in quantum mechanics, Raman transition can be utilized to engineer quantum states of a system.

If a Raman transition couples two different spin states of an atom with imparting non-zero momentum, the spin and momentum are intertwined in the Hamiltonian and the dispersion of the system shows intriguing aspects. This is equivalent to the famous spin-orbit coupling which can be found on atomic fine structure splitting and this is the underlying mechanism of topological insulators in condensed matter physics. So far, experimental and theoretical studies related to the topic have been investigated actively, since the first experimental realization of spin-orbit coupled Bose-Einstein condensates. Spin-orbit coupling of atomic gases has been demonstrated with alkali atoms, fermionic lanthanide atoms and recently, with alkaline-earth(-like) atoms such as ytterbium and strontium.

To study the spin-orbit coupling and its various modifications, we developed a ytterbium quantum gas machine and observed degenerate Fermi gas of ^{173}Yb atoms. We collect atoms with dark-spot Zeeman slower and magneto-optical trap. And atoms are evaporatively cooled in a crossed optical dipole trap. Typical atom number of degenerate sample is $\sim 10^5$ and minimum attainable temperature is $T/T_F < 0.1$. Detection and manipulation of nuclear spin of ytterbium ground state have been performed by optical pumping, optical Stern-Gerlach, and magnetic dipole transitions. Loading atoms on optical lattices is also demonstrated.

With generated degenerate Fermi gas, we study double resonance of Raman transitions. At the double resonance point, where two Raman transitions are simultaneously resonant to atoms, Raman branches in the spectrum show avoided crossing feature which can be quantitatively accounted for the light shift induced by Raman couplings. We discuss that the result can be interpreted to periodic spin-orbit coupling physics without an aid of additional rf coupling. Possible extensions of the experiment to show band structure engineering of spinful optical lattice and adiabatic loading on it are also examined.

Keywords : degenerate Fermi gas, ytterbium, spin-orbit coupling, Raman transition

Student number : 2011-20414

Contents

List of Figures

Chapter 1

Introduction

In this chapter, a brief review of experimental works with ytterbium quantum gases are elaborated. And, starting from quantum statistics, basics of degenerate Fermi gas are also given which are central topics of this thesis. Also, Raman transition, which is another central topic of this thesis, is also discussed. Lastly, an outline of this thesis is given at the end of this chapter.

1.1 Quantum gases of ytterbium atoms

Since the first realization of Bose-Einstein condensates [1–3] and degenerate Fermi gases [4–6] of alkali-metal atoms, ultracold atomic systems have opened new ways to tackle a variety of challenging physics [7,8]. Especially, owing to its fine control of dimensionality by optical lattices [9] and interactions by Feshbach resonance [10,11], many intriguing phenomena such as superfluid-Mott insulator phase transition [12] and BCS-BEC crossover [13–17] have been demonstrated. Moreover, quantum gases have extended their territory to simulating a role of charged particles like an electron, for example, generating synthetic magnetic

field [18–21] and spin-orbit couplings [22–24].

Aside from alkali-metal quantum gases, which have a single valence electron and therefore share some physical properties, atomic species with two valence electrons, such as ytterbium and strontium, have drawn interests. Due to their completely different electronic structure from alkali-metal atoms, there are unique features like $SU(N)$ symmetry [25–27], ultranarrow metastable states [28]. The $SU(N)$ symmetry which stems from zero electronic angular momentum J, makes the total spin F of the ground state completely decoupled from the electronic spin. In cases of fermionic atoms, especially whose total spin (= nuclear spin) is non-zero, the existence of a metastable $^3P_0$ state allows to study two orbital $SU(N)$ magentism [26, 29] with an aid of optical lattice potentials which are used to realize Fermi-Hubbard model [30]. In cases of bosonic atoms, which have zero nuclear spin, the magnetic field cannot affect the ground state at all, so they are good candidates of a precise atom interferometer [31].

Among two-valence electronic atoms, ytterbium has several advantages. First, the natural abundance of isotopes are balanced as summarized in Table 2.2, so both fermionic and bosonic atoms can be utilized easily. The s-wave scattering length for most abundant bosonic and fermionic atoms, ^{174}Yb, ^{173}Yb, respectively, are adequate to solely perform evaporative cooling [32, 33]. Moreover, sympathetic cooling is also experimentally feasible in case of atoms which are inefficient to be cooled by evaporative cooling [34,35]. Therefore, with small modifications in experimental setup, one can study both bosons, fermions, and various combinations of isotope mixtures [32, 34–36]. Secondly, relatively mild requirement of linewidth of intercombination transition ($^3P_1$) which is as $2\pi \times 182$ kHz, and mild temperature range to generate atomic vapor enable one to approach easier than other two-valence electronic atoms. Lastly, its large fine

structure spitting and thus large spin-orbit coupling strength owing to its heavy mass are desirable to study spin-orbit coupling physics [37, 38].

Here I summarize some important experimental works done with ytterbium atoms which gave me impressions. Ytterbium quantum gas experiments have been studied by several groups. The first experimental realizations of both Bose-Einstein condensate of ^{174}Yb and ytterbium degenerate Fermi gas of ^{173}Yb were succeeded by the Kyoto group [32, 33] and many of experiments using isotope mixtures of ytterbium have been performed [32, 34–36]. Photoassociation spectroscopy is extensively studied to determine collisional properties of Yb [39] at the early stage and spin squeezing with ^{171}Yb have been investigated [40]. The pomeranchuk cooling effect of ^{173}Yb is demonstrated also. And, the Washington group reported a mixture of ^{174}Yb and ^{6}Li [41–46]. They also studied about precision atom interferometry using spinless ^{174}Yb [31, 47]. Degenerate Bose-Fermi mixture of ^{87}Rb and ^{174}Yb is also demonstrated [48] by JILA group. The Hamburg group reported the realization of ytterbium Bose-Einstein condensate and degenerate Fermi gas with an apparatus using 2D MOT scheme [49–51]. Later, the LENS group and the MPQ group actively investigated two-orbital spin exchange dynamics using ultranarrow metastable transition of ^{173}Yb atoms [52,53]. A one-dimensional physics of spin tunable fermions [54] and observation of chiral edge current on a synthetic dimension [55] are also reported by LENS group. Later, the Mott plateau of SU(N) fermi gas [56] is reported by MPQ group. Recently, spin-orbit coupling of ^{173}Yb atoms is realized with a clock transition [57] by LENS group and a intercombination transition [58] by Hongkong group.

The main topics of this thesis are a creation of degenerate Fermi gas of ^{173}Yb atoms and an observation of double resonance of Raman transitions which is closely related to spin-orbit coupling. In an extention of studies of spin-orbit

coupling [23, 24], double resonance scheme suggests new type of spinful band structure by fully utilizing possible Raman transition paths which was ignored in previous studies [23, 24, 58]

1.2 Basics of Degenerate Fermi gas

1.2.1 Basics of quantum statistics

The indistinguishability of identical particles is a central concept of quantum statistics. Identical particles are fundamentally indistinguishable since we cannot label them. We cannot even keep sight of a specific particle since every measurement can disturb a quantum state of it, and one cannot guarantee that observed particle is the same one which we observed before.

From the fact that an arbitrary exchange of identical particles (or its combinations) in a system should give the same physically detectable results, every particles can be classified into two classes. Let us consider a wavefunction of N identical particles, $\psi(x_1, \cdots, x_N)$. We define an exchange operator P_{nm} which exchanges the n-th and the m-th particles and its eigenvalue is denoted as p_{nm}. If we perform the same exchange process twice, the wavefunction should be the same, namely,

$$\begin{aligned} & P_{nm}^2 \psi(x_1, x_2, \cdots, x_n, \cdots, x_m, \cdots, x_N) \\ = \; & p_{nm}^2 \psi(x_1, x_2, \cdots, x_n, \cdots, x_m, \cdots, x_N) \\ = \; & \psi(x_1, x_2, \cdots, x_n, \cdots, x_m, \cdots, x_N). \end{aligned}$$

where x_i is a collective index for a complete set of observables. The possible real values of p_{nm} are $+1$ and -1 in which cases the particles follow Bose-Einstein

statistics and Fermi-Dirac statistics, respectively. A wavefunction is totally symmetric in Bose-Einstein statistics and totally antisymmetric in Fermi-Dirac statistics. Particles which obey Bose-Einstein statistics is known as bosons and particles which obey Fermi-Dirac statistics is known as fermions. In case when quantum statistics is negligible, particles are said to obey Maxwell-Boltzmann statistics. Note that the whole story is for a three dimensional world and a complex eigenvalue of permutation operator can be exist in two dimensional case. Such particles is called anyons [59, 60].

Which statistics does the nature choose? It depends on a spin of a particle. According to *spin-statistics theorem*, a particle whose spin is integer is known to be a boson. And a particle whose spin is half integer is known to be a fermion. For example, a photon, a π meson, a Z^0 gauge boson, ^{4}He, ^{7}Li, ^{39,41}K, ^{23}Na, ^{84,86,88}Sr, ^{85,87}Rb, ^{133}Cs, and ^{170,172,174,176}Yb are bosons and an electron, a proton, a neutron, a neutrino, quarks, ^{3}He, ^{6}Li, ^{40}K, ^{87}Sr, and ^{171,173}Yb are fermions.

The crucial difference of bosons and fermions is that bosons can occupy the same states but fermions cannot. Consider a wavefunction of fermions ψ_F whose n-th and m-th particles are in a same state. By the assumption, $P_{nm}\psi_F = \psi_F$, therefore $\psi_F = 0$ which means there is no chance for fermions to be in a same states. This is equivalent to the famous *Pauli's exclusion princple* for electrons. To bosons, there is no such restrictions and it is allowed for particles to occupy any states. There is no restriction on state occupations for Maxwell-Boltzmann statistics. To explore a brief consequence of quantum statistics, let us consider two identical particles which allowed to be in a state $|1\rangle$ or state $|2\rangle$. Possible states satisfying Bose-Einstein statistics are $|1\rangle|1\rangle$, $\frac{1}{\sqrt{2}}(|1\rangle|2\rangle + |2\rangle|1\rangle)$, $|2\rangle|2\rangle$ where the first and the second ket represent the state of particle 1 and particle 2, respectively. For Fermi-Dirac statistics, the only allowed state is $\frac{1}{\sqrt{2}}(|1\rangle|2\rangle -$

$|2\rangle|1\rangle$). For Maxwell-Boltzmann statistics, four states $|1\rangle|1\rangle$, $|1\rangle|2\rangle$, $|2\rangle|1\rangle$, $|2\rangle|2\rangle$ are allowed. The probability of particles to be in a same state is highest when the particles obey Bose-Einstein statistics and is zero when the particles obey Fermi-Dirac statistics. This tendency is generally true with many particles and many states.

According to which quantum statistics particles follow, a ground state configuration of a system is totally different. Allowed energy minimum configuration for bosons is when all partcles occupy a single ground state, i.e., Bose-Einstein condensates which was first realized with alkali atoms [1–3]. In contrast, a fermionic system is in its ground state when atoms fill up from the bottom of the energy level to the top which is called Fermi level. This Fermi degeneracy was realized with atomic gases in [4–6] and we call it degenerate Fermi gas.

1.2.2 Properties of degenerate Fermi gas

According to the quantum statistics, the mean occupation number of single-particle state with energy E and chemical potential μ is given by

$$\langle n(E)\rangle = \frac{1}{\exp[\beta(E-\mu)] \pm 1} \tag{1.1}$$

where $\beta = 1/k_B T$, the plus sign is for fermions and minus sign is for bosons [61]. From now on, we concentrate on the case of fermions. The number of a specific spin σ of an atom is given by

$$N_\sigma = \int_0^\infty \frac{g(E)dE}{\exp[\beta(E-\mu)] + 1} \tag{1.2}$$

where $g(E)$ is density of states with energy E. It is convenient to define fugacity $z = e^{\beta\mu}$ which is frequently used to determine how much the system is in

quantum degeneracy. $z = 0$ for classical case and $z = \infty$ at $T = 0$. The total energy of the system can be written

$$E_{tot} = \int_0^\infty \frac{g(E)EdE}{\exp[\beta E] + 1}. \tag{1.3}$$

If atoms are confined in 3D harmonic trap

$$V(x, y, z) = \frac{1}{2}M(\omega_x x^2 + \omega_y y^2 + \omega_z z^2), \tag{1.4}$$

the density of states corresponds to $g(E) = E^2/2\hbar^3\bar{\omega}^3$ [(1)] ,where $\bar{\omega}^3 = \omega_x\omega_y\omega_z$ is geometric mean of trapping frequencies. At $T = 0$, Eq. 1.2 gives $E_F = \hbar\bar{\omega}(6N_\sigma)^{1/3}$ and Fermi temperature T_F is defined by $T_F = E_F/k_B$. Or, by comparing the total energy and the number of atoms, one can easily find $\mathrm{Li}_3(-z) = -\frac{1}{6(T/T_F)^3}$ where $\mathrm{Li}_\nu(x)$ is polylogarithmic function of order ν.

Density distributions

From the mean occupation number in Eq. 1.1, one can express the desity of states in a phase space with $E = p^2/2m + V(x, y, z)$ as

$$f(r, p) = \frac{1}{h^3}\frac{1}{z^{-1}\exp[\beta(p^2/2m + V(x, y, z))] + 1} \tag{1.5}$$

where the factor $1/h^3$ comes from the fact that each state on a phase space possess a volume of h^3 [(2)]. Therefore, the density on position and momentum space can be expressed as

$$n(\mathbf{r}) = \int f(\mathbf{r}, \mathbf{p})\, d\mathbf{p}, \tag{1.6}$$

$$n'(\mathbf{p}) = \int f(\mathbf{r}, \mathbf{p})\, d\mathbf{r}, \tag{1.7}$$

[(1)] One can easily show this expression considering the energy of 3D harmonic oscillator $E = \hbar\omega_x(1/2 + n_x) + \hbar\omega_x(1/2 + n_y) + \hbar\omega_x(1/2 + n_z)$. The number of possible combinations whose energy is E gives g(E) in the text.

[(2)] Otherwise, we can write $f(r, k) = \hbar^3 f(r, p)$. $f(r, k)$ is more common but we choose to write $f(r, p)$ because we are more familiar to p than k.

respectively. Here we applied Thomas-Fermi approximation [7, 62] which assumes exact sum of the eigenstates of given potential is equivalent to the approximated value in a large N limit. In this approximation, particles are labeled not by the quantum numbers of each eigenstates but a position and a momentum only. Resulting expressions for 3D harmonic oscillator are given by

$$n(\mathbf{r}) = \left(\frac{2\pi m k_B T}{h^2}\right)^{3/2} \mathrm{Li}_{3/2}\left(-z e^{\beta V(x,y,z)}\right), \tag{1.8}$$

$$n'(\mathbf{p}) = \left(\frac{2\pi k_B T}{m\bar{\omega}^2 h^2}\right)^{3/2} \mathrm{Li}_{3/2}\left(-z e^{\beta p^2/2m}\right). \tag{1.9}$$

Note that the spatial distribution $n(\mathbf{r})$ is asymmetric and the momentum distribution $n'(\mathbf{p})$ is symmetric.

For most of experiments, we measure the momentum distribution of fermi gases which is integrated along imaging direction. Therefore, what we really measure follows

$$\tilde{n}(x,y) \propto \mathrm{Li}_2\left(-z\ e^{-x^2/2\sigma_x^2 - y^2/2\sigma_y^2}\right), \tag{1.10}$$

where $\sigma_i = \frac{k_B T}{m\omega_i^2}[1 + (\omega_i t)^2]$ [63]. After sufficient time of fight, typically 15 ms which gives $\omega t = 4$, momentum distributions become radially symmetric and we can safely regards that the image represents momentum distribution. To determine the degree of degeneracy T/T_F, we fit our radially averaged data with Eq. 1.10 to have z.

1.3 Ramans transition

Raman transition is a kind of two photon processes in which a system *simultaneously* absorbs and emits photons. Under certain conditions, a system never affected by the excited state and we cannot separately deal with absorption

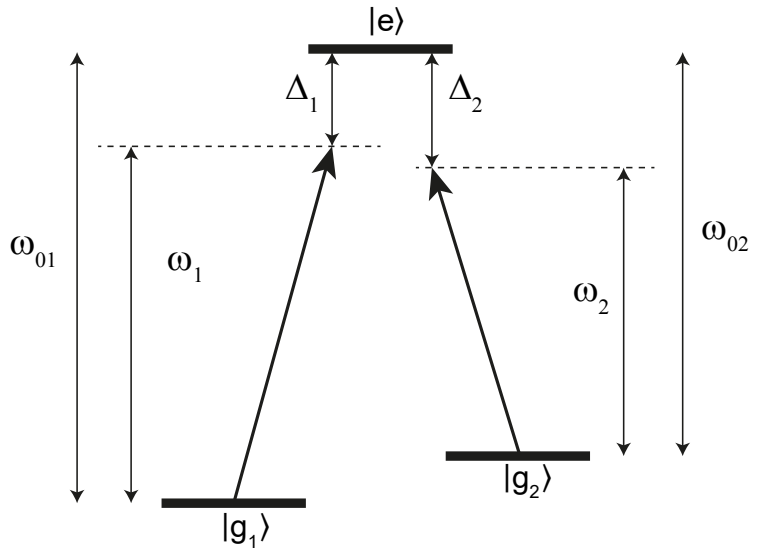

Figure 1.1: Schematic diagram of Raman transitions. See the text.

and emission. The applicability of Raman processes is very versatile for wide range of areas like biology, chemistry, engineering, etc. By Raman process, it is possible to take *a detour* to a target state or to give strong coupling which is impossible to realize, directly.

Here I summarize some steps describing Raman transition and its consequences. The detailed derivation can be found in the Ch. 6 of [64]. Consider a energy structure in the Λ-configuration where two ground states $|g_1\rangle$ and $|g_2\rangle$ are coupled with an excited state $|e\rangle$ by two optical fields

$$\mathbf{E}(\mathbf{r},t) = \hat{\epsilon_1} E_1 \cos(\mathbf{k_1}\cdot\mathbf{r} - \omega_1 t) + \hat{\epsilon_2} E_2 \cos(\mathbf{k_2}\cdot\mathbf{r} - \omega_2 t) \tag{1.11}$$

where ϵ_i are a unit polarization vectors, $\mathbf{k_i}$ are wavevectors, and ω_i are the angular frequency of the lasers. The atomic Hamiltonian can be written

$$H_{\text{atom}} = \frac{p^2}{2m} - \hbar\omega_{01}|g_1\rangle - \hbar\omega_{02}|g_2\rangle \tag{1.12}$$

where we set the energy of the excited state to zero. And, with the dipole approximation, the atom-photon interaction Hamiltonian is

$$H_{\text{dip}} = -\mathbf{d} \cdot \mathbf{E} \tag{1.13}$$

where $\mathbf{d}$ is dipole moment of the atom. By separating a positive and a negative rotating term in $\mathbf{E}(\mathbf{r}, t)$ and $\mathbf{d}$ with the rotating approximation, the atom-photon interaction Hamiltonian is

$$\begin{aligned} H_{dip} =& \frac{\hbar\Omega_1}{2}\sigma_1 e^{-i\mathbf{k_1}\cdot\mathbf{r}} e^{i\omega_1 t} \\ &+ \frac{\hbar\Omega_2}{2}\sigma_2 e^{-i\mathbf{k_2}\cdot\mathbf{r}} e^{i\omega_2 t} + H.C. \end{aligned} \tag{1.14}$$

where $\Omega_i = -\langle g_i|\hat{\epsilon_1} \cdot \mathbf{d}|e\rangle E_i/\hbar$, and $\sigma_i = |g_i\rangle\langle e|$ [64]. For convenience, let us remove a time dependent part $e^{i\omega_i t}$ by transforming the ground states into a rotating frame of the lasers. Then the total Hamiltonian is

$$H = \frac{p^2}{2m} + \hbar\Delta_1|g_1\rangle + \hbar\Delta_2|g_2\rangle \tag{1.15}$$

$$+ \left(\frac{\hbar\Omega_1}{2}\sigma_1 e^{-i\mathbf{k_1}\cdot\mathbf{r}} + \frac{\hbar\Omega_2}{2}\sigma_2 e^{-i\mathbf{k_2}\cdot\mathbf{r}} + H.C.\right) \tag{1.16}$$

where $\Delta_i = \omega_i - \omega_{0i}$.

With this simplified Hamiltonian, let us discuss the wavefunction dynamics of Raman transition. If we take a transformation which boosts the energy of all states by $\Delta = (\Delta_1 + \Delta_2)/2$, and assume $\Delta \gg |\Delta_1 - \Delta_2|$, only ψ_e rotates in a much faster time scale than $\psi_{g1,g2}$. So we can neglect the time dependence of the excited state and the dynamics happends only between the two ground states. This indicates simultaneous photon absorption and emission which does not populate the excited state. The resulting equations of motions of the two

ground states are

$$i\hbar\partial_t\psi_{g_1} = \frac{p^2}{2m}\psi_{g_1} + [\hbar\Delta_1 + \hbar\omega_{AC1}]\psi_{g_1} + \frac{\hbar\Omega_R}{2}e^{i(\mathbf{k_2}-\mathbf{k_1})\cdot\mathbf{r}}\psi_{g_2} \tag{1.17}$$

$$i\hbar\partial_t\psi_{g_2} = \frac{p^2}{2m}\psi_{g_2} + [\hbar\Delta_2 + \hbar\omega_{AC2}]\psi_{g_2} + \frac{\hbar\Omega_R}{2}e^{i(\mathbf{k_1}-\mathbf{k_2})\cdot\mathbf{r}}\psi_{g_1} \tag{1.18}$$

where $\Omega_R = \frac{\Omega_1\Omega_2}{2\Delta}$ is effective Rabi frequency of Raman process, and $\omega_{AC1,AC2} = \frac{\Omega_{1,2}^2}{4\Delta}$ are AC Stark shifts. Accounting the two ground states only, effective two-level Hamiltonian is

$$\begin{aligned} H_{\text{eff}} =& \frac{p^2}{2m} + \hbar(\Delta_1 + \omega_{AC1})|g_1\rangle\langle g_1| + \hbar(\Delta_2 + \omega_{AC2})|g_2\rangle\langle g_2| \\ &+ \frac{\hbar\Omega_R}{2}\left(|g_1\rangle\langle g_2|e^{i\delta\mathbf{k}\cdot\mathbf{r}} + |g_2\rangle\langle g_1|e^{-i\delta\mathbf{k}\cdot\mathbf{r}}\right) \end{aligned} \tag{1.19}$$

where $\delta\mathbf{k} = \mathbf{k_2} - \mathbf{k_1}$.

1.3.1 Raman transitions and spin-orbit couplings

The $e^{\pm i\mathbf{k_r}\cdot\mathbf{r}}$ terms on off-diagonal elements mean momentum transfer during state changing. If the two ground states are regarded as pseudo-spins, the Raman coupling can be explained with a term of the spin-orbit coupling [22]. After a unitary transformation which shifts the momentum states of $|g_1\rangle$ by $+\delta\mathbf{k}/2$ and $|g_2\rangle$ by $-\delta\mathbf{k}/2$, exponential term on the off-diagonal parts are vanished and quasi momenta which allow energy minimum of each state are non-zero. In a matrix form,

$$H'_{\text{eff}} = \begin{bmatrix} \frac{(\mathbf{q}-\hbar\delta k/2)^2}{2m} + \hbar(\Delta_1 + \omega_{g_1}) & \frac{\hbar\Omega_R}{2} \\ \frac{\hbar\Omega_R}{2} & \frac{(\mathbf{q}+\hbar\delta k/2)^2}{2m} + \hbar(\Delta_2 + \omega_{g_2}) \end{bmatrix} \tag{1.20}$$

or, equivalently in an operator form,

$$H'_{\text{eff}} = \frac{(\mathbf{q} - \sigma_z\hbar\delta k/2)^2}{2m} + \frac{\hbar\delta}{2}\sigma_z + \frac{\hbar\Omega_R}{2}\sigma_x + const. \tag{1.21}$$

where $\mathbf{q}$ is a quasi-momentum, σ_i are Pauli 2×2 spin matrices, $\hbar\delta/2 + const. = \hbar(\Delta_1 + \omega_{AC1})$ and $-\hbar\delta/2 + const. = \hbar(\Delta_2 + \omega_{AC2})$. The term proportional to $-\mathbf{q}\sigma_z$ represents spin-orbit coupling with an equal sum of Rashba and Dresselhaus spin-orbit coupling.

1.4 Outline of the thesis

This thesis mainly covers experimental realization of a degenerate Fermi gas of ^{173}Yb atoms and experiments on Raman transitions. The first four chapters from Ch. 2 are about how to prepare degenerate Fermi gases. In Ch. 2, basic properties of ytterbium atoms are summarized from physical properties to interactions with electric fields. In Ch. 3, detailed information of the experimental apparatus is elaborated. I tried to make the chapter helpful for those who are unfamiliar with but has to do something with the machine. In Ch. 4, experimental sequences to reach quantum degeneracy from a bulk Yb metal are explained including practical characterizations of the machine during cooling steps. As the last chapter about the sample preparation, in Ch. 5, detecting and manipuating nuclear spin states of Yb are discussed.

From Ch. 6, experimental studies on the Raman transitions are discussed. Chapter 6 introduces a double resonance of Raman transitions which can be extended to a concept of periodic spin-orbit coupling. Experiments with periodically spin-orbit coupled atoms are presented in Ch. 7. And, a summary of this thesis is given in Ch. 8. I hope this thesis would be a helpful material for someone might be in a trouble with the machine.

Chapter 2

Basic properties of ytterbium atoms

2.1 Physical properties and precautions

Ytterbium is soft, silverly white metal with a pale yellow tint. The crystal structure of the ytterbium is face-centered cubic. It melts at 1097 K and boils at 1469 K. The vapor pressure of the ytterbium at 736 K is 7.5×10^{-3} Torr. It slowly reacts with cold water and and oxidizes in the air slowly [65]. Therefore, ytterbium must be stored away from the atmosphere and moisture.

All compounts of ytterbium atoms are known to be highly toxic. These can irritate human skin and eyes. Metalic dust of ytterbium can burn spontaneously, and resulting gas is very hazardous. In case of fire, one should use dry chemical class D fire extinguisher, not water [66].

2.2 Electronic properties of ytterbium

Ytterbium is lanthnide atom with $Z = 70$. The electronic configuration of the ground state is $[\mathrm{Xe}]4f^{14}6s^2$. Since the f-shell is fully occupied, the atomic properties of the atom are mainly determined by the two electrons in $6s$ shell. Thus, its properties are very similar to alkaline-earth atoms like strontium.

2.2.1 Atomic level structure of two-valence-electron atoms

The hamiltonian of the system can be written as

$$H = \sum_{i=1}^{N} \big[-\frac{-\hbar^2}{2m}\nabla_i^2 + V_{CF}(r_i) + \big\{ \sum_{j>i}^{N} \frac{e^2/4\pi\epsilon_0}{r_{ij}} - S(r_i)\big\}\big], \tag{2.1}$$

where $\hbar$ is reduced Plank's constant, m is mass, N is a number of electrons, r_{ij} is the relative distance between i-th and j-th electrons, ϵ_0 is permittivity of free space, e is the charge of an electron, $V_{CF}(r) = -\frac{Ze^2/4\pi\epsilon_0}{r} + S(r)$ and $S(r)$ is the central part of the electron-electron repulsion which stems from spherically symmetric charge distribution [67]. We can partition the Hamiltonian as $H = H_{CF} + H_{re}$, which represent central potential part and residual electrostatic interaction where

$$H_{CF} = \sum_{i=1}^{N} \big[-\frac{-\hbar^2}{2m}\nabla_i^2 + V_{CF}(r_i)\big], \tag{2.2}$$

$$H_{re} = \sum_{i=1}^{N}\sum_{j>i}^{N} \big[\frac{e^2/4\pi\epsilon_0}{r_{ij}} - S(r_i)\big]. \tag{2.3}$$

For H_{CF}, the Hamiltonian is spherically symmetric. The eigenstates of the system is well described by the good quantum numbers, n_i, l_i and s_i where n_i is principal quantum number, l_i is orbital angular momentum quantum number and s_i is the spin for i-th electron. The residual electrostatic repulsion term

cannot change the sum of the angular momentum quantum number L since the electronic repulsion is internal force and the spin is irrelevant to electronic repulsion. Therefore, the eigenstate of the system can be labeled by L, m_L, S and m_S. This is well known LS-coupling (or Russel-Saunders) scheme.

The total wavefunction ψ is given by the product of spatial wavefunction ψ_{space} and spin wavefunction ψ_{spin} and should be anti-symmetric under a particle exchange. Since the Hamiltonian is separable for each electron, the spatial wavefunction is given by the product of each electronic wavefunction.

For example, the ground state wavefunction of ytterbium is given by $\psi = u_{6s0}(1)u_{6s0}(2)\psi_{spin}$ where $u_{nlm}(i)$ is spatial wavefunction of i-th electron. Note that the energy of the states does not depend on m so we can discard it from now on. ψ_{spin} should be anti-symmetric, namely, singlet spin state $\psi^A_{spin} = \frac{1}{\sqrt{2}}(|\uparrow\downarrow\rangle - |\downarrow\uparrow\rangle)$ with $S = 0$. For the excited states, two solutions of spatial wavefunctions $u_{6s}(1)u_{nl}(2)$ and $u_{6s}(2)u_{nl}(1)$ are degenerate and possible spatial wavefunctions are linear combinations of the two, $\psi^A_{space} = (u_{6s}(1)u_{nl}(2) - u_{6s}(2)u_{nl}(1))/\sqrt{2}$, $\psi^S_{space} = (u_{6s}(1)u_{nl}(2) + u_{6s}(2)u_{nl}(1))/\sqrt{2}$. The total wavefunction satisfying anti-symmetry should be $\psi = \psi^A_{space}\psi^S_{spin}$ or $\psi = \psi^S_{space}\psi^A_{spin}$ where ψ^S_{spin} is tripplet spin wavefunction with $S = 1$. Therefore, in spectroscopic notation ${}^{2S+1}L$, the possible states of ytterbium atoms are ${}^1S$, ${}^1P$, ${}^1D$, ${}^3S$ and so on.

the effect of spin-orbit interaction

The Hamiltonian in Eq. 2.1 is not exact. There are additional spin-orbit interaction term

$$H_{so} = \alpha_1 \mathbf{l_1} \cdot \mathbf{s_1} + \alpha_1 \mathbf{l_1} \cdot \mathbf{s_1}. \tag{2.4}$$

This term in principle adds coupling between the states with L, m_L, S, m_S bases. When $H_{so} \ll H_{re}$, spin-orbit interaction term can be treated perturbatively leaving L and S constant and changing their direction. Since orbital angular momentum l_i and spin s_i for each electron precess around $\mathbf{L}$ and $\mathbf{S}$, it is possible to take $\mathbf{l_i} \propto \mathbf{L}$ and $\mathbf{s_i} \propto \mathbf{S}$ in time averaging sense, semi-classically. Then H_{so} is proportional to $\mathbf{L} \cdot \mathbf{S}$ and is diagonal in $\mathbf{J} = \mathbf{L} + \mathbf{S}$ basis. The eigenstate of the system is diagonal to L, S, J, m_J bases and spectroscopic notation is ${}^{2S+1}L_J$ like ${}^1S_0$,${}^1P_1$,${}^3P_2$,${}^3P_1$ and ${}^3P_0$.

When $H_{so} \gg H_{re}$, spin-orbit interaction term can be diagonalized by introducing $\mathbf{j_i} = \mathbf{l_i} + \mathbf{s_i}$. Since H_{re} term causes mixing between $\mathbf{j_1}$ and $\mathbf{j_2}$, and again, total angular momentum of the system $\mathbf{J} = \mathbf{j_1} + \mathbf{j_2}$ is good basis to describe the system. In this case, j_1, j_2, J, m_J are good quantum numbers. This is so called jj-coupling scheme.

In case of light atoms, spin-orbit interaction is small so LS-coupling scheme is appropriate to portray the system. In contrast, heavy atoms show stronger spin-orbit interaction and LS-coupling bases are not diagonal to eigenstates. Therefore, there is a mixing between states with different L, S but same J. What we call ${}^3P_1$ state is not diagonal in pure L, S bases. This is why the electronic-dipole-forbidden transition from ${}^1S_0$ to ${}^3P_1$ state which I will cover later.

2.2.2 Level structure of ytterbium

The transition lines and level structure of the ytterbium is displayed in Fig. 2.1 and Fig. 2.2. As shown in table 2.1, ${}^1P_1$ transition is strong and suitable to slow down atoms from high velocities so we use for Zeeman slowing which I describe

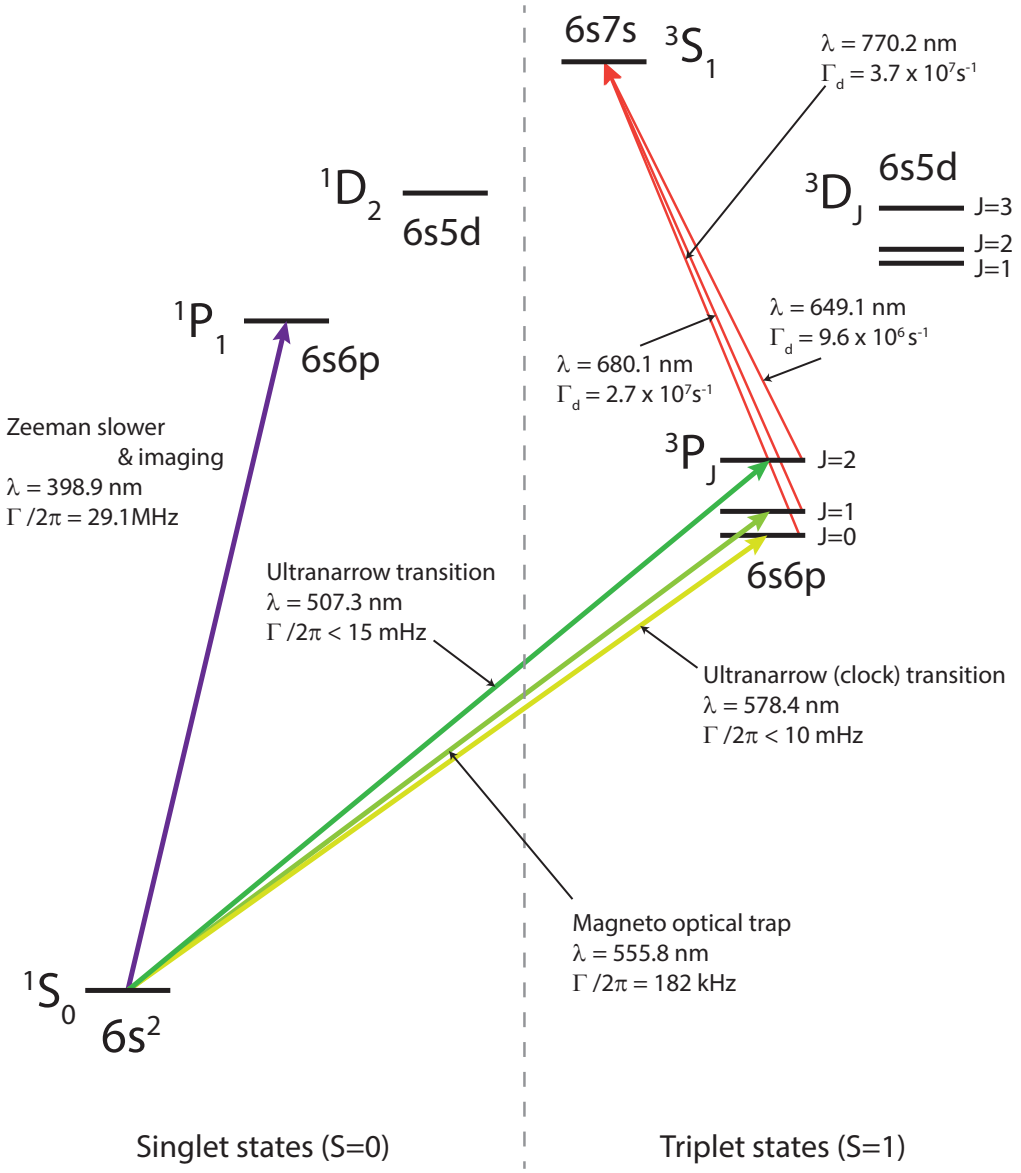

Figure 2.1: The level diagram of ytterbium. Colored solid arrows represent optical transitions. We use singlet transition to $^1P_1$ as a Zeeman slowing beam and imaging. And triplet transition to $^3P_1$ is used as magneto optical trap, optical Stern-Gerlach, and spin dependent imaging. Γ is natural linewidth for closed transition and Γ_d is decay rate [68, 69].

in detail in Sec. 4.1. On the other hand, $^3P_1$ transition is quite narrow and the Doppler temperature is only 4.4 μK which offer colder MOT than the singlet transition.

Parameters	$^1S_0 \rightarrow {}^1P_1$	$^1S_0 \rightarrow {}^3P_1$
λ	398.9 nm	555.8 nm
$\Gamma/(2\pi)$	29.1 MHz	182.4 kHz
τ	5.464 ns	866.1 ns
g_J	1.035	1.493
I_{sat}	59.97 mW/cm^2	0.139 mW/cm^2
T_d	699 μK	4.4 μK
v_r	5.8 mm/s	4.2 mm/s

Table 2.1: Parameters related to the $^1S_0 \rightarrow {}^1P_1$ and $^1S_0 \rightarrow {}^3P_1$ transitions. $\lambda, \Gamma, \tau, g_J, I_{\text{sat}}, T_d, v_r$ represent the wavelength, natural linewidth, lifetime, g-factor, saturation intensity, Doppler temperature and recoil velocity, respectively [39, 70].

2.3 Isotopes of ytterbium

There are seven stable isotopes of ytterbium. There are five bosons and two fermions which makes ytterbium very charming element. Natural abundance is quite balanced. Quantum degeneracy of six isotopes have been reported [32, 33, 35, 36, 71, 72]. All kinds of mixtures like Bose-Bose, Bose-Fermi, Fermi-Fermi mixtures are realizable with simpler setup than two species machine. In experiments, Bose-Fermi, Fermi-Fermi mixtures have been demonstrated [35, 73].

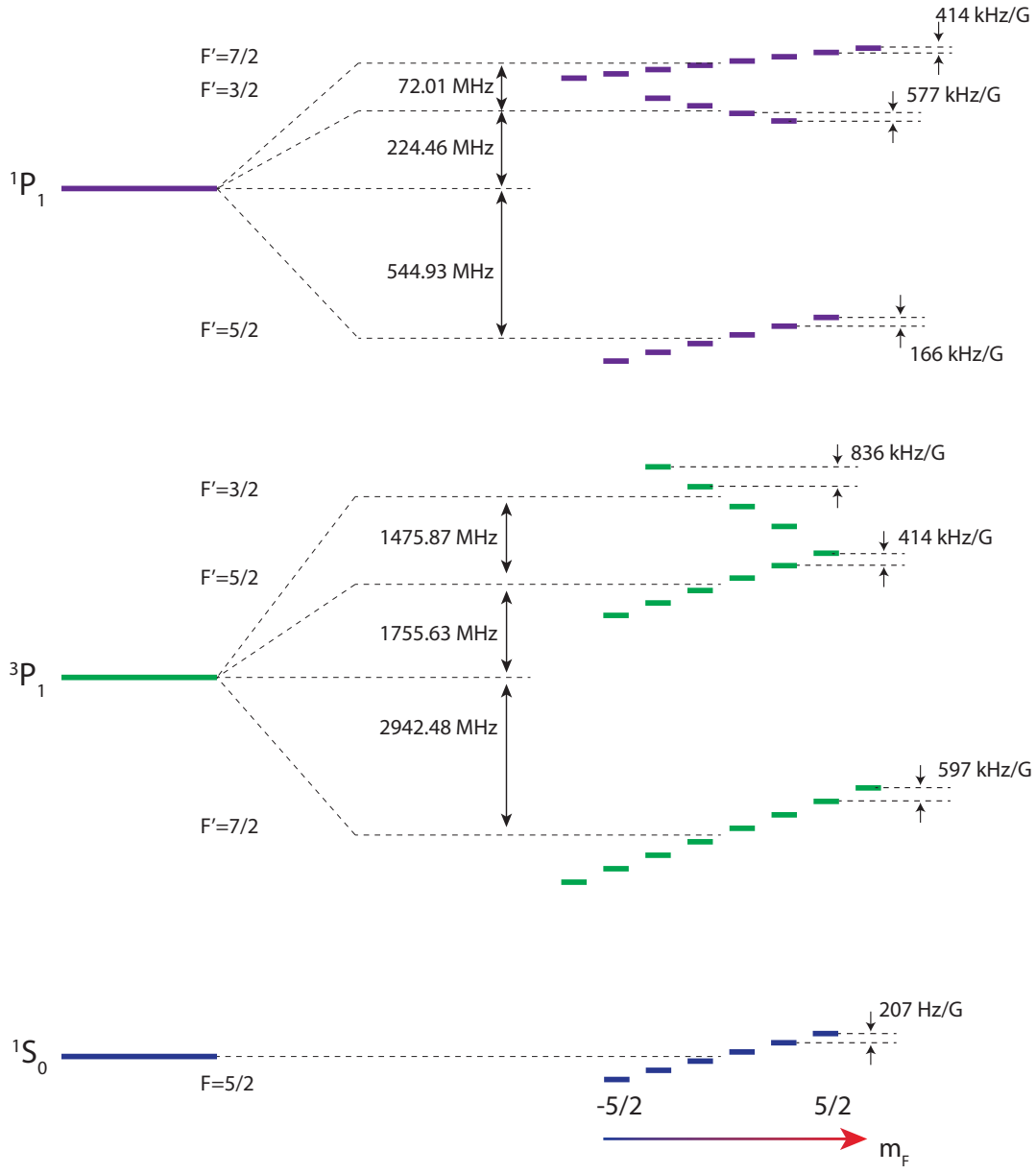

Figure 2.2: The most frequently used transition line of ^{173}Yb. The hyperfine splittings and relevant Zeeman splittings are displayed. The figure is not drawn to scale.

Isotopes	mass	nuclear spin	natural abundance (%)	magnetic moment(μ_I)
^{168}Yb	167.933894	0	0.13	
^{170}Yb	169.934759	0	3.05	
^{171}Yb	170.936323	1/2	14.3	+0.4919
^{172}Yb	171.936378	0	21.9	
^{173}Yb	172.938208	5/2	16.12	-0.6776
^{174}Yb	173.938859	0	31.8	
^{176}Yb	175.942564	0	12.7	

Table 2.2: A summary of physical parameters for ytterbium isotopes [74].

2.4 Scattering properties

Scattering property of an atom is a crucial factor which determines the cooling ability to quantum degeneracy by evaporative cooling, solely. Scattering length, which govern the scattering properties, should be large enough to perform evaporative cooling which accompanied by fast thermalization through collision process. Also, scattering length should not be large to prevent unwanted three-body collision which cause atom loss and heating.

2.4.1 Scattering between isotopes

Isotopes	^{168}Yb	^{170}Yb	^{171}Yb	^{172}Yb	^{173}Yb	^{174}Yb	^{176}Yb
^{168}Yb	**252.0(34)**	117.0(15)	89.2(17)	65.0(19)	38.6(25)	2.5(34)	359.2(30)
^{170}Yb		**63.9(21)**	36.5(25)	-2.1(36)	-81.3(68)	-518.0(51)	-209.5(23)
^{171}Yb			**−2.8(36)**	-84.3(68)	-578(60)	-429(13)	141.6(15)
^{172}Yb				**−599(64)**	418(13)	200.6(23)	106.2(15)
^{173}Yb					**199.4(21)**	138.8(15)	79.8(19)
^{174}Yb						**104.9(15)**	54.4(23)
^{176}Yb							**−24.2(43)**

Table 2.3: S-wave scattering lengths of ytterbium atoms in ground state in units of Bohr radius a_0 for complete combinations of isotopes. The bold numbers are values for homonuclear pairs. Data are taken from [75].

The ground state of ytterbium atoms show a variety of s-wave scat-

tering lengths as shown in table 2.3. Luckily, the most abundant boson and fermion,^{174}Yb and ^{173}Yb, are appropriate to perform evaporative cooling, solely. Also, these two isoptes serve as good coolants for other isotopes whose s-wave scattering length is not proper for evaporative cooling. For example, ^{171}Yb whose scattering length is too small, can be successfully sympathetic-cooled by ^{173}Yb [75].

2.4.2 Control of interaction strength

Typically, for alkali atoms, the tunability of interaction strength by changing scattering length with magnetic Feshbach resonance (MFR) allows many fruitful studies such as BCS-BEC crossover [76, 77]. However, this is not the case for the ground states of two-valence electron atoms. As an alternating way, optical Feshbah resonance (OFR) is studied [78–81]. Compared to conventional MFR, OFR has several advantages. First, using OFR, one can modulate the scattering length in much faster time scale than MFR which is experimentally limited by the inductance of the coil. And, spatial modulation of scattering length is also possible which is experimentally challenging with MFRs. Secondly, OFR can be applied to all atomic species. Moreover, OFR can control scattering properties between two different atomic species.

The most significant disadvantage of OFR is heating issue. Unlike MFR which couples two different stable states, OFR couples the ground state and an excited state which has relatively short lifetime. Therefore, atoms suffer from spontaneous emission. Ytterbium have a strength on using OFR thanks to its intercombination transition to $^3P_1$ state whose natural linewidth is smaller than the alkali atoms, thus the heating is alleviated. Recently, new type of

interaction control between different orbital states using metastable $^3P_0$ has been demonstrated [82,83]. They utilized the mixing of triplet and singlet states of nuclear spin states where each is on different orbital states.

2.4.3 SU(N) symmetry

The lack of hyperfine interaction ($J = 0$) in $^1S_0$ state ensures spin-independent scattering property. The magnetic dipole-dipole interaction between the nuclear spin is negligible: Magnetic dipole-dipole interaction energy between two dipoles, whose magnitude is 10 μ_I and separated by 10 nm, is only 0.77 Hz. Thus the collision process is governed solely by the interaction between electron clouds, not nuclear spin. This feature gives interesting property, so called SU(N) symmetry [29].

The presence of $^3P_0$ state, which is also SU(N) symmetric, provides many rich aspect regarding to SU(N) symmetry. The interplay of the two-orbital states, $^1S_0$ and $^3P_0$, and almost totally decoupled nuclear spin states opens new possiblity to explore an exotic quantum magnetism. Moreover, it is shown that two-orbital SU(N) system can be used to realize theoretical models, such as Kugel-Khomskii model in transition-metal oxides [84, 85], Kondo lattice model in heavy fermion physics [86–89] and other Hamiltonians whose ground state is valence-bond-solid or spin-liquid states [29, 90–93]. As a first step, two-orbital nuclear spin exchange interaction is observed [52, 53, 94]. More detailed discussions about the SU(N) symmetry and orbital magnetism are well described in [29, 69] and references there in.

Notice that the SU(N) symmetry is no longer preserved under an additional coupling with an excited state, such as $^1P_1$ and $^3P_1$. For example, $^3P_1$

state-dressed atoms have a mixing between electronic part and the nuclear spin part of the Hamiltonian. Therefore, the collisional processes which mainly governed by the electronic clouds are not decoupled with nuclear spins, which breaks SU(N) symmetry.

2.5 Interaction with magnetic field

The magnetic-dipole-interaction Hamiltonian under the magnetic field $\mathbf{B}$ considering hyperfine-structure is given by

$$\begin{aligned} H_B &= -(\boldsymbol{\mu}_S + \boldsymbol{\mu}_L + \boldsymbol{\mu}_I) \cdot \mathbf{B} && (2.5)\\ &= -(\boldsymbol{\mu}_J + \boldsymbol{\mu}_I) \cdot \mathbf{B} && (2.6)\\ &= -\boldsymbol{\mu}_F \cdot \mathbf{B} && (2.7)\\ &= \frac{\mu_B g_F}{\hbar} \mathbf{F} \cdot \mathbf{B} && (2.8)\\ &= \mu_B g_F m_F B && (2.9) \end{aligned}$$

where $\boldsymbol{\mu}_S, \boldsymbol{\mu}_L, \boldsymbol{\mu}_J, \boldsymbol{\mu}_I, \boldsymbol{\mu}_F$ are magnetic dipole moments of electronic spin, electronic orbital angular momentum, total electronic angular momentum, nuclear spin, and total angular momentum. μ_B is Bohr magneton, g_F is landé g-factor, m_F is magnetic quantum number along the direction of magnetic field. The landé g-factor is given by

$$\begin{aligned} g_F = g_J \frac{F(F+1) - I(I+1) + J(J+1)}{2F(F+1)} && (2.10)\\ + g_I \frac{F(F+1) + I(I+1) - J(J+1)}{2F(F+1)} && (2.11) \end{aligned}$$

where

$$g_J \approx 1 + \frac{J(J+1+S(S+1)-L(L+1)}{2J(J+1)}, \tag{2.12}$$

$$g_I = \frac{\mu_I}{\mu_B|I|}. \tag{2.13}$$

For the bosonic isotopes, ${}^1S_0$ state does not have magnetic sublevels. This is a useful feature in precision measurement and atomic interferometry [31, 95]. For the fermioinc ${}^1S_0$ state, total electronic angular momentum J is zero and the only contribution to the magnetic moment is the second term in 2.11 which stems from the nuclear spin. Its order of magnitude is $m_p/m_e \approx 1836$ times smaller than non-zero J case where m_p and m_e are the mass of a proton and an electron. Therefore, the ground state is insensitive to magnetic field than $J \neq 0$ states. In case of ^{173}Yb, for instance, the Zeeman shift between adjacent spins is only 207 Hz/G. Note that, despite of small magnetic moment of the ground state, magnetic dipole transition of ^{173}Yb between nuclear spin states is possible as we described in Sec. 5.4.2.

In contrast, for ${}^3P_1$ and ${}^1P_1$ states, where spin-orbit interaction exists, Zeeman splitting is three orders of magnitude larger than the ground state. The summary of Zeeman splittings of ^{173}Yb atoms is given in Fig. 2.2.

2.6 Interaction with optical field: optical dipole potential

Here, I will cover the response of atoms under the optical field. The most dominant part of the atom-photon Hamiltonian is dipole potential term $H_d = -\mathbf{d}\cdot\mathbf{E}/2$ where $\mathbf{d}$ is an electric dipole moment and $\mathbf{E}$ is an electric field. The

factor of 2 comes from the fact that the dipole moment is induced one, not permanent. Semiclassical approach helps to get an intuition of the phenomena. First, the electronic clouds covering the nucleus deformed as an external electric field is applied. That cause induced electric dipole moment and the induced dipole moment interact with the external electric field. So an atom feels the potential [96]. We call it optical dipole potential, or equally, AC Stark shift or light shift.

Quantum mechanically, optical dipole potential can be explained by the second-order time-independent perturbation theory, or by dipole matrix element calculation. The optical dipole potential term in Hamiltonian is given by $H' = -\mathbf{p}\cdot\mathbf{E}$, resulting the optical dipole potential

$$\Delta E = -\sum_b \frac{|\langle b|\mathbf{d}\cdot\mathbf{E}|a\rangle|^2}{\hbar}\Big(\frac{1}{\omega_{ba}-\omega_L}+\frac{1}{\omega_{ba}+\omega_L}\Big) \tag{2.14}$$

where $|a\rangle = |\alpha\ F\ m\rangle$ is the ground state, $|b\rangle = |\alpha'\ F'\ m'_F\rangle$ is an excited states, $\hbar\omega_{ba} = E_b - E_a$, and $\hbar\omega_L$ is the energy of a photon of the laser. $\alpha_{a,b}$ reprensents the radial part of the wavefunction. We include counterrotating term which is not negligible in far-off resonant cases. From now on, let us consider the dipole moment and the electric field is well aligned.

By virtue of Wigner-Eckart theorem, one can decompose the dipole matrix element into its radial part and angular part [64, 97]. The former is related to the decay rate of an excited state and the latter Clebsch-Gordan coefficients as

$$\langle b|\mathbf{d}|a\rangle \;=\; e\langle\alpha F||r||\alpha' F'\rangle \times \langle F\ m_F|F'\ m'_F;1\ q\rangle \tag{2.15}$$

where q is a polarization of the light, and

$$\begin{aligned}\langle \alpha F||r||\alpha' F'\rangle &= \langle \alpha J||r||\alpha' J'\rangle (-1)^{F'+J+1+I} \\ &\times \sqrt{(2F'+1)(2J+1)} \left\{ \begin{array}{ccc} J & J' & 1 \\ F' & F & I \end{array} \right\}.\end{aligned} \tag{2.16}$$

The curly brace means Wigner's 6-j symbol. The reduced dipole matrix element can be calculated using the decay rate as

$$\Gamma_{\alpha' J', \alpha J} = \frac{\omega_{ba}^3 e}{3\pi\epsilon_0 \hbar c^3} \frac{2J+1}{2J'+1} |\langle \alpha J||r||\alpha' J'\rangle|^2 \tag{2.17}$$

where ϵ_0 is the vacuum permittivity, c is the speed of light. The angular part of the matrix element is

$$\langle F\ m_F|F'\ m'_F; 1\ q\rangle = (-1)^{-F'+1-m_F} \sqrt{(2F+1)} \begin{pmatrix} F' & 1 & F \\ m'_F & q & m_F \end{pmatrix},$$

where the round bracket means Wigner 3-j symbol. We define a constant C_{ba} that includes all the complications as

$$\begin{aligned} C_{ba} &= (-1)^{J+I-m_F} \sqrt{(2F'+1)(2F+1)(2J'+1)} \\ &\times \begin{pmatrix} F' & 1 & F \\ m'_F & q & -m_F \end{pmatrix} \left\{ \begin{array}{ccc} J & J' & 1 \\ F' & F & I \end{array} \right\}. \end{aligned} \tag{2.18}$$

Note that due to selection rule, $m'_F = m_F + q$.

With all this together, resulting optical dipole potential can be expressed as

$$\Delta E = -\sum_b \frac{3\pi c^2}{2\omega_{ba}^3} \Gamma_b |C_{ba}|^2 \Big(\frac{1}{\omega_{ba} - \omega_L} + \frac{1}{\omega_{ba} + \omega_L} \Big), \tag{2.19}$$

where we used $I = 2\epsilon_0 c|E|^2$. In case the beam is near resonant, whose detuning is smaller than the hyperfine splitting, one should count all the contributions

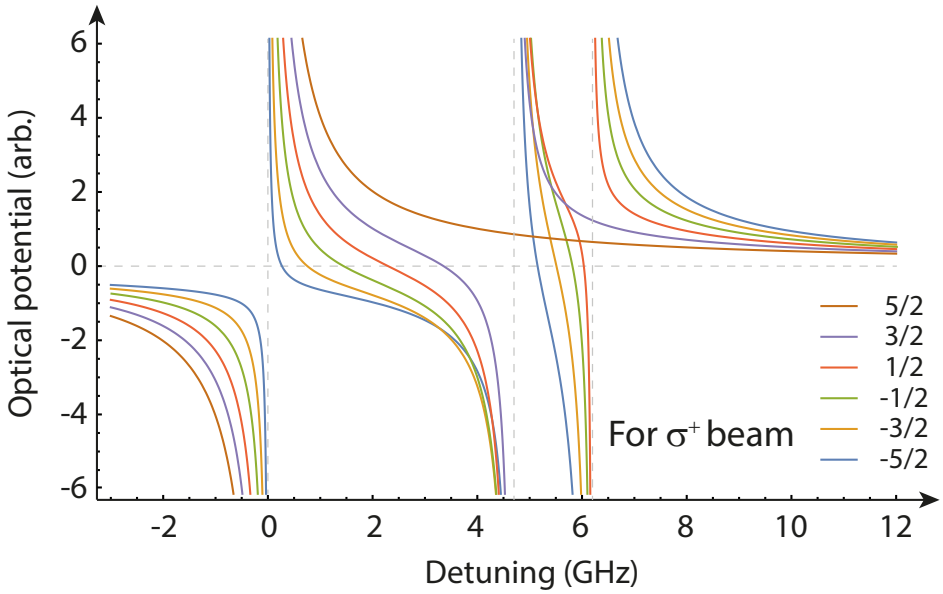

Figure 2.3: Optical potentials around ${}^3P_1$ transitions. The horizontal dashed line is a guide for zero potential line and the vertical dashed lines are the resonant positions of $F' = 7/2, 5/2$ and $3/2$ transitions from left. We can see some spins are immune to the resonances on $F' = 5/2$ and $3/2$ due to the selection rule.

of excited hyperfine states with different weights. Figure 2.3 shows optical potentials of ${}^3P_1$ transitions of each spin as a function of detuning from $F' = 7/2$ which is used frequently.

Chapter 3

Experimental Apparatus

In this chapter, I will introduce our experimental apparatus for generating ytterbium quantum gasses. The machine can be divided into three parts: laser system, vacuum system, and control system. Each part will be covered in following sections.

3.1 Brief history – At the beginning

I participated the ytterbium team at 2013 after almost finishing Rubidium MOT project. At that time, members of ytterbium team were Min-Seok Kim and Min-Sik Kwon. They were struggling to build up 399 nm laser systems with Nichia laser diodes (LDs). With Nichia LDs, we found a spectrum of $^3P_1$ transitions and got error signals. However, they were severely unstable; Single mode state was easily broken, therefore frequency stabilization was impossible despite success in KRISS, Korea university group, and Kyoto group.

We took a detour to generate 399 nm lasers. We decided to build up second harmonic generator (SHG). The prototype of SHG was already designed

and was ready at the time I joined the team and the first mission of mine was to assemble an SHG. We used Toptica TA pro 798nm (1.1W) as a fundamental laser and 15mm Castech LBO crystal. We used two mirrors and two curved mirrors made by CVI Melles griot Korea. The reflectivity of input coupling mirror was 99.5%.

With the first design, I only got the 399 nm output of about 70mW which was insufficient for Zeeman slower, spectroscopy, and imaging. The efficiency was too lower than I expected. We spent some time (it was not short, sadly.) and found out aligning labor is not helpful to overcome that situation. We found out that the calculated value of beam waist at the crystal center was wrong because the walk-off angle of the LBO crystal was not considered. So we needed to calculate new beam waist and reflectivity of input coupler. Right at that time, very helpful paper "efficient frequency doubling at 399 nm" was uploaded on the arXiv and we followed some parameters on that paper. I should mention that in developing the 399 nm laser system that I will cover in the following subsection, [98] gave lots of useful information and was very helpful.

3.2 399 nm and 556 nm laser systems

To gather ytterbium atoms, two optical transitions are used; 399 nm $^3P_1$ transition and 556 nm $^3P_1$ transition. Unfortunately, so far, laser diodes for the two wavelengths are not well developed so we built two frequency doublers for each 399 nm and 556 nm. In this section, I will describe fundamentals of SHG and introduce the two laser systems briefly. For practical informations about how to build the SHG cavity system, the thesis of Min-Seok Kim would be also helpful [99].

3.2.1 principles of second harmonic generator

The basic principle of second harmonic generator (SHG) is given in this section. Conventions and logical flow follows that of [100].

SHG is based on non-linear effect of a material. Non-linear effect means the polarizability of a material does not have linear relationship with electric field. The polarizability of non-linear material can be described by $P = \epsilon_0 \chi\, E + P_{\mathrm{NL}}$ with non-zero P_{NL} whereas for linear dielectric material, $P_{\mathrm{NL}} = 0$. As we use oscillating electric fields, it is natural to expand a polarizability in a Taylor series about $E = 0$, namely, $P = a_1 E + \frac{1}{2} a_2 E^2 + \frac{1}{6} a_3 E^3 + \cdots$. In the traditional form, $P = \epsilon_0 \chi E + 2dE^2 + 4\chi^{(3)} E^3 + \cdots$ [100].

If an electric field $E = E_0 e^{i\omega t}$ propagates in this non-linear medium, the polarizability of the medium oscillates in the angular frequency $m\omega$ where m is an integer. Therefore, the medium radiates frequency doubled, tripled or multiples of lights with non-linear medium.

Mathematically, electric fields must obey Maxwell equation,

$$\nabla^2 E - \frac{1}{c_0^2} \frac{\partial^2 E}{\partial t^2} = \mu_0 \frac{\partial^2 P}{\partial t^2}. \tag{3.1}$$

Using $c = c_0/n, n^2 = 1 + \chi$ and $c_0 = 1/(\epsilon_0 \mu_0)^{1/2}$, the equation becomes

$$\nabla^2 E - \frac{1}{c^2} \frac{\partial^2 E}{\partial t^2} = -S \tag{3.2}$$

$$S = -\mu_0 \frac{\partial^2 P_{\mathrm{NL}}}{\partial t^2}. \tag{3.3}$$

S plays a role of a source of electric fields which is the function of electric field itself and the source contains multiple frequency components with respect to the incident light.

For a nonlinear medium whose second-order nonlinearity is dominant, one can write $P_{NL} = 2dE^2$. For a monochromatic electric field $\mathcal{E}(t) = E(\omega) cos(\omega t)$,

$P_{NL}(t) = P_{NL}(0) + dE^2(\omega)cos(2\omega t)$. The intensity of the generated light $I(2\omega)$ from the source is proportional to $|S(2\omega)|^2$, which is proportional to d^2 and $I(\omega)^2$, where $I(\omega)$ is the intensity of the incident light.

For a second harmonic generation, the frequency-matching condition $2\omega_1 = \omega_2$ and the phase-matching condition $2\vec{k}_1 = \vec{k}_2$ between the incident fundamental laser and second harmonic generated light have to be satisfied, namely $n(\omega) = n(2\omega)$ where $n(\omega)$ is the refractive index of the material. This condition can be satisfied by carefully choosing orientation or the temperature of the crystal. We matched the phase by temperature tuning for the green laser, and angle tuning for the blue laser. For angle matching, there arises unavoidable walk-off to the output beam and that cause divergent beam profile along one axis.

The efficiency of second harmonic generation of Gaussian beam is given by Boyd-Kleinman formula [101] as

$$E_{\mathrm{NL}} = \frac{16\pi^2 d_{\mathrm{eff}}^2 L}{\epsilon_0 c \lambda_1^3 n^2} e^{-\alpha L} h_m(B, \xi), \tag{3.4}$$

where d_{eff} is effective non-linear coefficient of the crystal, λ_1 is the wavelength of the fundamental beam, α is the absorption of the laser beam, L is the length of the crystal, and $h_m(B, \xi)$ is Boyd-Kleinman parameter. B is related to the walk-off angle ρ as $B = \rho\sqrt{\pi L n_1 / 2\lambda_1}$ and ξ is focussing of the Gaussian beam $\xi = L/2z_R$ where $z_R = \pi w_0^2/\lambda_1$ and w_0 is the beam waist. The total output power of SHG is $P_{\mathrm{SHG}} = E_{\mathrm{NL}} P^2$. Our mission is to maximize the overall efficiency E_{NL} along the non-linear medium.

The power which can be obtained by typical tapered amplifier is about $\sim$ 1W and this is way too weak to reach $\sim$10 % efficiency. For example, the SHG efficiency of our blue SHG system is 7.3×10^{-5} W which only gives 73 μW for

the input power of 1 W. To overcome this limitation, people have used optical cavity to boost the input power of the fundamental laser. We use the bow-tie configuration and carefully chose the reflectivity of the input-coupling mirror which determines the efficiency of the cavity: Maximum efficiency is achieved if "the total loss of one round trip" equals to the transmission of the mirror [98,99]. It was the most cost-inefficient step to determine the optimum reflectivity of the input-coupling mirror and we finally followed the value presented in [98] for 399 nm cavity. (However, I believe that the reflectivity value we have chosen to use is not the optimum value for both systems and there are still some rooms to optimize the cavities.)

3.2.2 The 399 nm laser system

The 399 nm cavity

We generate 399 nm laser by frequency doubling the 798 nm fundamental laser which is generated with commercial laser (Toptica TA pro 798). After a careful beam shaping, the fundamental laser beam incident to the SHG cavity where we used AR coated LBO crystal from Raicol company. We typically achieved 270 mW of 399 nm laser beam from 1.3 W of 798 nm fundamental laser. The SHG efficiency dropped as we increased the power of the fundamental laser, and the maximum 399 nm power reached 500 mW with input power of 2.8 W.

It is reported that the performance of the LBO crystal degrades because of humidity and oxygen vacancies as a result of aging. To guard the crystal from this detrimental effect, we sealed the whole blue cavity part of the system with acryl box, which is filled with pure oxygen and we frequently injected oxygen. After the first oxygen injection, we observed a slight increase of the output

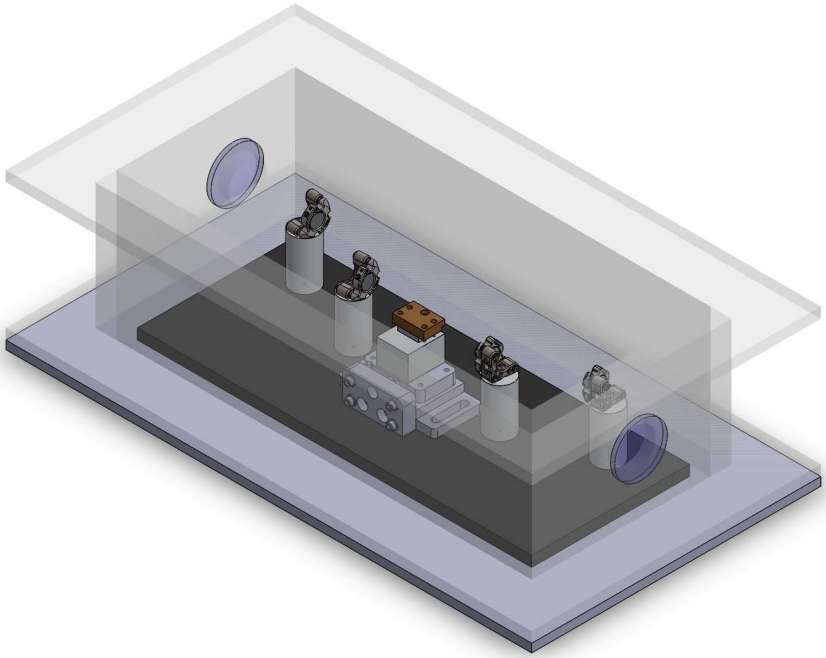

Figure 3.1: CAD model of the blue SHG system with outer acryl box and windows.

power of about 10 mW.

For cavity optics mounts, we use Thorlabs 0.5" Polaris mounts which provides a pleasing stability of the system. Thanks to the mounts and air sealing, our system provides constant efficiency over a year without a realignment of the cavity optics inside the box. Most frequently drifting parts were input coupling mirror and TA optics inside the toptica TA pro box which also gave a gratifying stability.

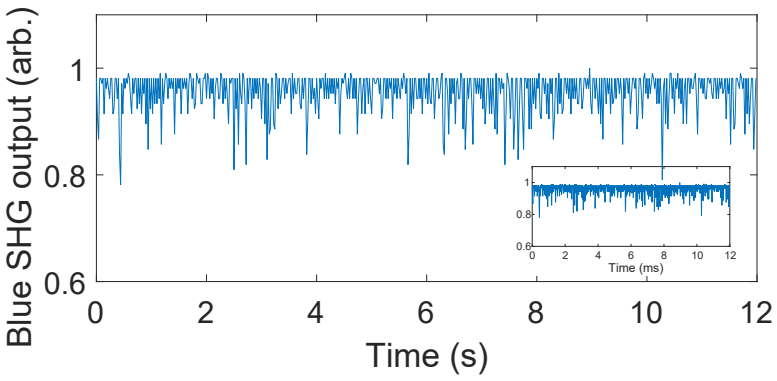

Figure 3.2: Output power stability of 399 nm SHG cavity normalized by the maximum value of the data. The RMS error of the data are 12%. inset: stability for a short period.

We used Thorlabs achromatic half waveplate (AHWP05M-600) and observed large variance of the SHG efficiency as we vary the angle between the laser and the surface of the waveplate. We attribute this effect to a slight difference of the retardation from $\lambda/2$ and slight displacement of the beam path. The temperature of the crystal is stabilized at 23.2 °C.

We stabilize the SHG cavity to the 798 nm fundamental laser which gave us a well-defined single frequency mode along the scanning range. The error signal for cavity stabilization is acquired by differentiating absorption spectrum of different polarizations, namely, Hänsch-Couillaud scheme. The stability of the output signal strongly depends on the alignment of Hänsch-Couillaud optics and the voltage applied to PZT inside the cavity. Our cavity stabilization is achieved by SRS SIM960 PID controller and is fast enough to follow fundamental laser scanning of about 5 Hz for the stabilization to an atomic reference.

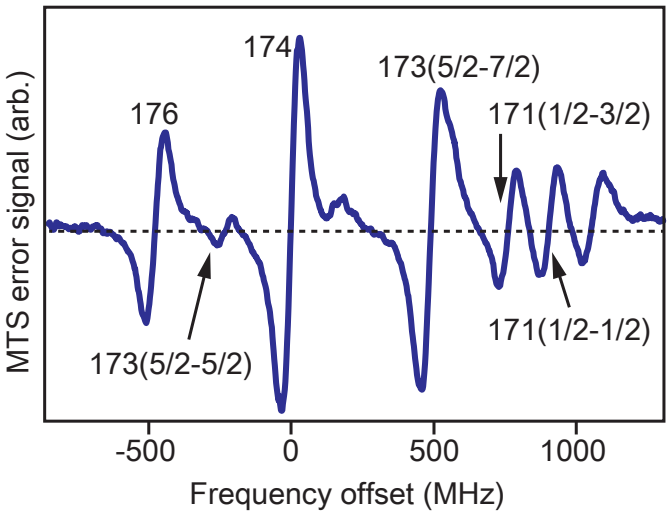

Figure 3.3: Modulation transfer spectroscopy signal of 399 nm $^1P_1$ transition.

Spectroscopy

To stabilize the laser frequency to atomic reference, we perform modulation transfer spectroscopy [102]. We choose the modulation frequency of the pumping beam as 25MHz which is the same order of magnitude as the natural linewidth of $^1P_1$ laser of 29 MHz because it is known that the signal is clear under that condition [102]. We built home-made MTS lock-in box to extract the error signal from the MTS signal. We use Toptica Digilock module to stabilize the frequency of fundamental laser to the extracted error signal which is delivered to the module via auxiliary port.

For an atom source for the spectroscopy, we use hollow cathode lamp HCL, Hamamatsu L2738 Yb-Ne operated by high voltage power supply (PS310/1250V-25W, SRS). Typically, we used 177V and 1mA to drive HCL. The nominal life-

time of a HCL is 5000 mA hour. However, surprisingly, we have used more than 10000 hours with 1mA. To perform experiments with 173Yb, the laser is stabilized to the resonance of 174 Yb which provides us about 500MHz shift without using an acousto optic modulator (AOM). Similarly, we use ^{176}Yb transition line for ^{174}Yb experiment.

Other issues with the 399 nm laser

We suffered by a detrimental effect of 399 nm lasers on polarizing beam splitters (PBS). Polarizing beam splitters are easily burnt and we observed a yellow bright spot at the cube interface. This effect was observed nevertheless we used high power version of polarizing beam splitter (PBS25-405-HP, Thorlabs). As a result, the power of the laser and the fiber coupling efficiency dropped. We couldn't avoid this effect so we shifted the PBS to move the beam point, occasionally.

Optical fibers also get damaged by 399 nm laser. At the first time, when we had not enough laser power, we used (QPMJ-3A3A-400-3/125-3-7-1) from OZ optics and it was not a problem. But as we succeeded to increase the SHG efficiency, the fiber coupling efficiency slowly dropped. So we changed to high power compatible optical fiber (QPMJ-A3HPC-400-7, OZ optics) which have shown reliable performance.

3.2.3 The 556 nm laser system

The 556 nm cavity

We built another SHG cavity system to generate 556 nm laser beam. The fundamental 1112 nm laser is generated by a commercial fiber laser system from

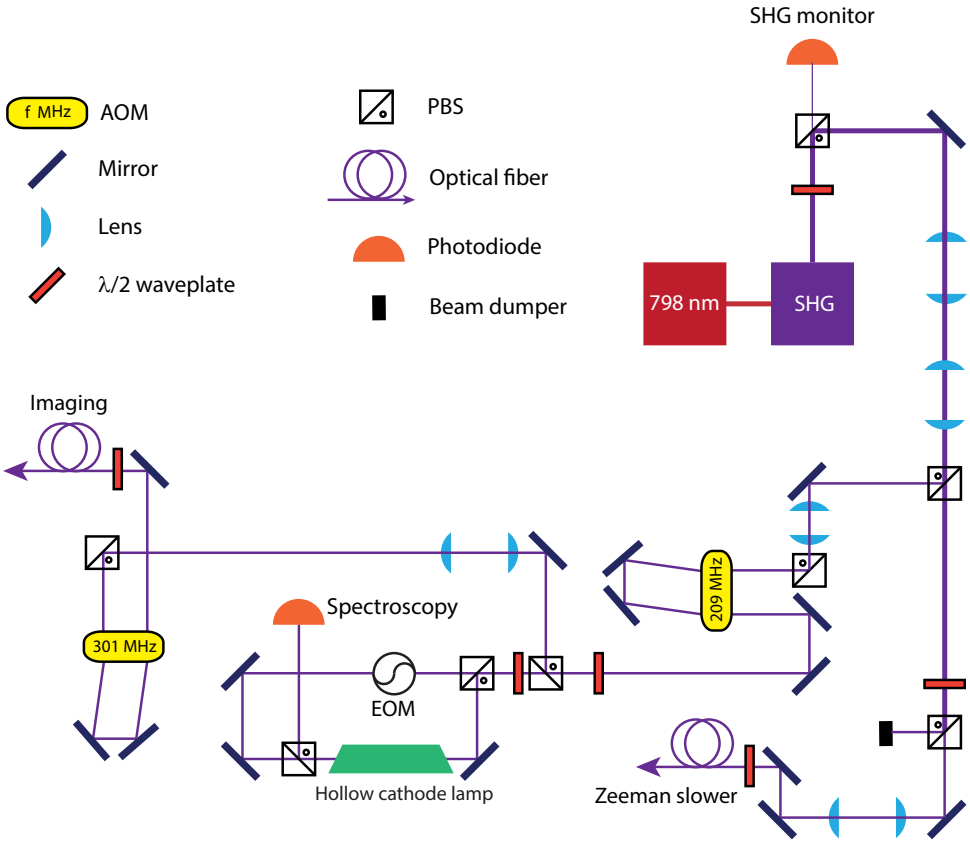

Figure 3.4: The 399 nm laser system optics diagram.

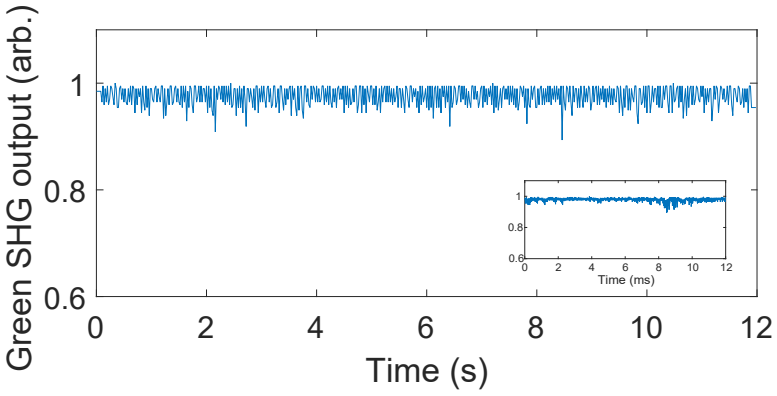

Figure 3.5: Output power stability of 556 nm SHG cavity normalized by the maximum value of the data. The RMS error of the data are 3.8%. inset: stability for a short period.

Menlo systems (Orange 1). We used an AR coated LBO crystal from Castech company. We typically achieved green laser output of 220 mW with 1.1 W of the fundamental beam. Since the phase-matching is achieved by temperature tuning around 105°C, there is no walk-off angle for the green laser resulting nearly perfect Gaussian beam shape. As in the 399 nm cavity setup, cavity power stailization is achieved by the Hänsch-Couillaud scheme. The output power stability of the 556 nm laser is shown in Fig. 3.5.

Spectroscopy

Modulation transfer spectroscopy is achieved with a atomic reference cell and an electro-optic modulator (EOM) driven by RF freqeucny of 3 MHz. Since the signal is weak for $^3P_1$ transition due to its small saturation intensity of 0.14 mW/cm^2, very weakly reflected 556 nm laser severly distrubs the MTS sig-

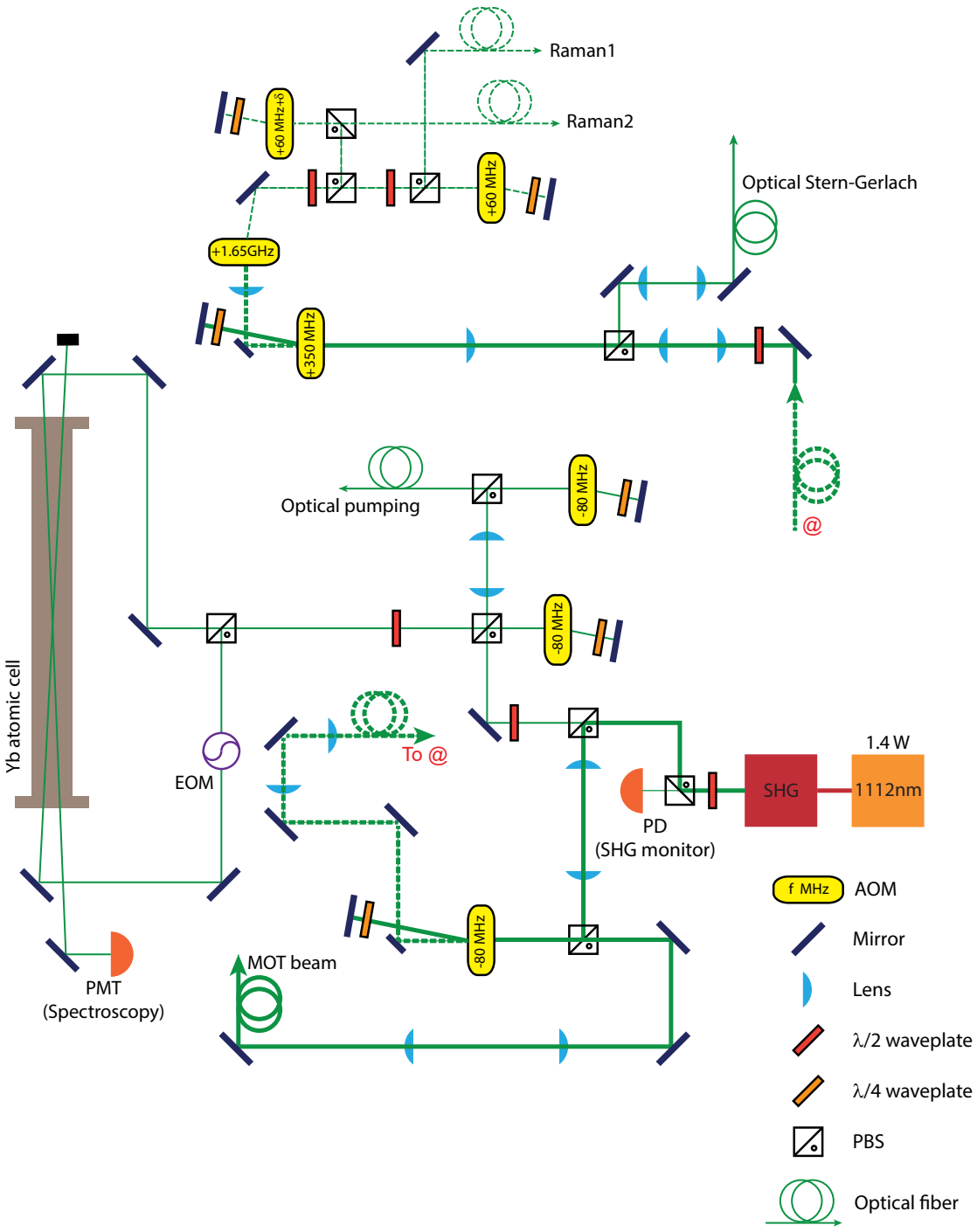

Figure 3.6: The 556 nm laser system optics diagram.

nal. We located the photo-multiplier tube (PMT) as far as possible and misaligned the spectroscopy beams incident on the atomic cell to avoid unwanted reflection on PMT. Otherwise, we suffered from the oscillating MTS error signal which affects the lock stability and drifting. It would be better to attach atomic cell windows obliquely.

For atomic reference, we use atomic cell which is operated about 460°C. To prevent ytterbium atoms from depositing on the windows of atomic cell, windows are heated to 150°C. Bright flourescence signal can be seen through the window on the cup. The peak value of MTS error signal increases as the temperature of the atomic cell become higher than 430°C. We found MTS error signal for many isotopes and we identify each transition by its relative distance.

3.3 Optical dipole trap system

To achieving quantum degeneracy, two colors of optical dipole trap is used. First, we load atoms in 1070 nm optical dipole trap and transport the atoms to a small, science chamber which provide better optical access and high magnetic field. There we cross 532 nm optical dipole trap and perform evaporative cooling. In this section, I will describe two dipole trap setups and stabilization schemes.

3.3.1 1070 nm optical dipole trap and optical transport

The compressed MOT is loaded on the 1070 nm optical dipole trap. The 1070 nm optical dipole trap perform evaporative cooling and transport to the science chamber. To spatially mode-match with the atoms in the MOT and provide sufficient trapping force against the gravity, the waist of the vertical direction is smaller than the horizontal one. The waists of the trap are 26 μm$\times$72 μm

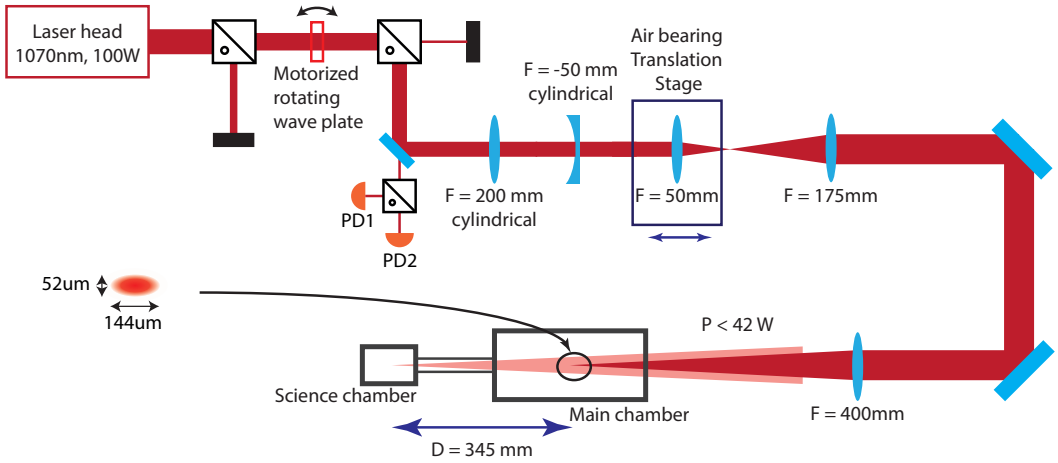

Figure 3.7: The 1070 nm laser system optics diagram.

and are constant during a transport sequence. A schematic optics digram is presented in Fig. 3.7. The two cylindrical lenses are used for the ellipticity and the other three lenses are used for transport and focusing.

We use PID circuits (SIM960, Stanford Research Systems) to stabilize and control the power of the laser beam. The power range of the 1070 nm laser during the evaporative cooling is quite broad, from several tens of watts to around 0.2 W which makes it difficult to maintain stability for both regions. To avoid this problem, we monitor beam power with two photodiodes (DET36A/M, Thorlabs) for different power range. Each voltage serves as a measurement signal to a PID and voltage input is switched by a multiplexer (ADG5209, Analog devices). With this technique, the setpoint is far above than the resolution limit of the analog NI card (5 mV) and we are able to stabilize the power for the entire range.

The power stabilization is performed by two components. One is by ana-

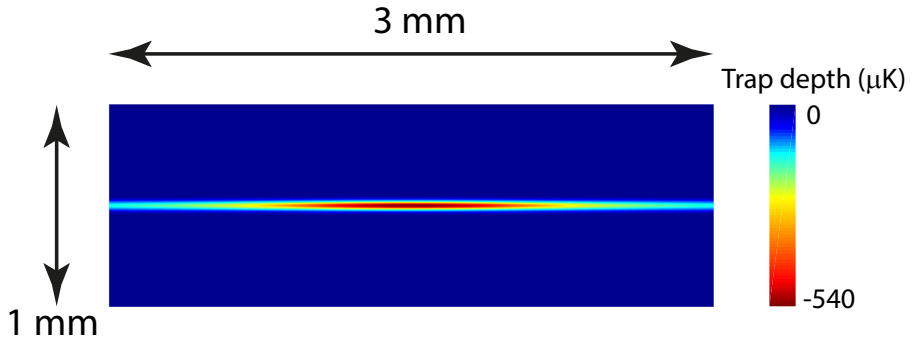

Figure 3.8: The dipole potential of 1070 nm laser at the main chamber.

log control of laser itself and the other is a rotating wave plate. The reason why we don't use AOM is explained on high power optics subsection. Since we use fiber laser, we cannot lower the power below the minimum operating value which is far higher than we need at the final stage of evaporation. So we use the rotating wave plate which attenuates the laser power without reducing output power of the laser. For the evaporative cooling, we coarsely tune the laser power by the rotating wave plate and the power finely follows the setpoint by the analog control of the laser.

Optical transport

By moving the position of a lens, we move atoms from the main chamber to the science chamber which provide easy optical access. The transport system comprises of three 2" achromatic lenses from Thorlabs. The focal lengths of the lenses are 50 mm, 175 mm and 400 mm which are carefully chosen for transport range of 345 mm and to avoid beam clipping during beam propagation.

The optical system can be interpreted as follows. The first lens makes

focus and the other lenses project the focus to the sample. The middle and the last lenses form 4-f system with magnification of $M = 400/175 \approx 2.3$. When the first lens is on its initial position, the focal plane is at the MOT in the main chamber. As we move the first lens with air bearing translation stage (ABL1000, Aerotech) by distance d, the focal plane moves by a distance of $M^2 d$. So our 100 mm translation distance of the first lens can cover the distance between the main chamber and the science chamber. The waist of the beam is not changed during the transportation and we can give the same potential depth to the sample, except the contribution of acceleration along the longitudinal direction.

Aside from ABCD matrix calculation which gives full information of the propagation of Gaussian beam, one can intuitively explain why the moving distance of the focus at the sample plane is $M^2 d$ and why the beam waist is kept constant [103]. First, the phase space density of a beam is constant under a propagation since every point on the initial phase space distribution is projected to the final one following Liouville's Theorem. If we project a beam by a 4-f system, the final distribution of one real space becomes larger by a factor of M and the momentum distribution is decreased by a factor of $1/M$. As a result, it takes M^2 times longer distance to achieve focal plane if the initial position is not a focus. About the constant waist, the 4-f system maps the curvature of the intial beam and the beam waist after the first lens is not affected by its position because the waist of incident beam to the first lens is quite large. Therefore, the beam waist is constant regardless of the position of the first lens.

With this setup, we can successfully transport atoms from the main chamber to the science chamber. The transportation time is 1.6 seconds and the transfer efficiency is 85% which is obtained by comparing the number of atom transported and the number of atom remained in the main chamber dur-

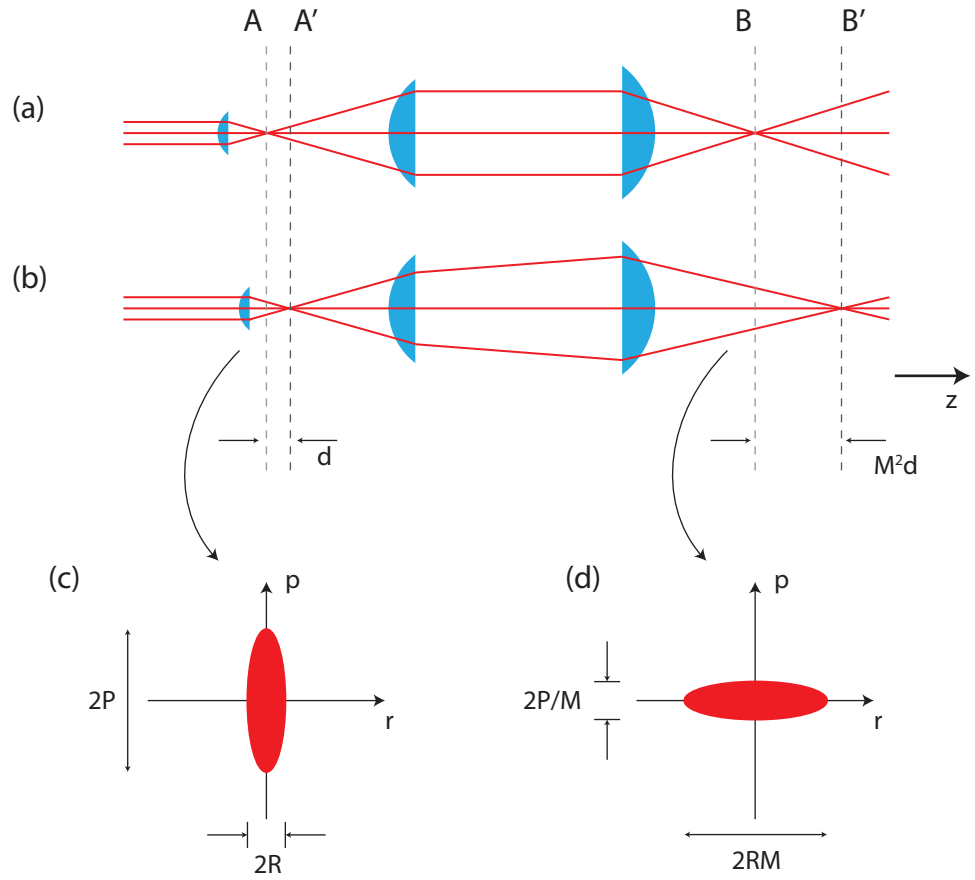

Figure 3.9: (a), (b) Simple ray optics picture for the principle of optical transport. The first lens moves and the focal plane is changed from A to A' by a distance d. The phases space representing spatial extent and momentum are depected in (c), (d) for plane A and B, respectively. By 4-f setup with magnification M, the phase space is deformed as in the figure. On the plane B, the momentum is reduced by a factor of M and the spatial extent which is a distance to go along r direction to make focus is enlarged by a factor of M. Therefore, the total distance from plane B to plane B' is M^2d.

ing the transportation time. The velocity profile of translation stage is a simple triangular shape and I expect further optimization is possible for the transport process.

There are another option for optical transport. That is to make focus by lens with long focal length like 800 mm and to move focus by moving the mirror by translation stage, directly. Or, instead of mirror, the ENS group uses corner cube reflector [104] which gives better beam pointing stability than just moving a mirror. The benefits of our option is that we need shorter moving distance (only 100 mm) of the translation stage which is economic and that we don't need to use long f lens which is better to achieve tight focus. However, with our setup, small vibration can be amplified at the plane of the atoms and this might cause beam pointing unstability, more easily.

Beam pointing stability

We suffered from vibrational noises coming from the cooling water that chills magnetic coils. It was unimportant for the loading sequence from the magneto optical trap. However, the number of degenerate fermi gas severely fluctuated and we couldn't cool atoms under certain temperature even though we have sufficient number of atoms in the trap. To solve this problem, we isolated water flow from the machine with Sorbothane sheets and blocks (Thorlabs), and we installed solenoid valve which can block and open the water flow. We shut the water flow after atoms are loaded on the optical traps. With this, we achieved temperature as low as $T/T_F \sim 0.1$ and increased number of atoms by factor of 1.5.

High power optics

The maximum laser power of the 1070 nm laser is about 42 W. Such a high power cause thermal lensing effect to nearly all optical components. Thermal lensing effect is observed during atom loading sequence from MOT and evaporative cooling. As we vary the hold time before imaging with atoms loaded on the 1070 nm dipole trap, the position of the atoms is moved and the direction is the same as what it has to be when the focal lengths of lenses are increased. Therefore, we tried to minimize the thickness of the optics. We recently replaced thick polarizing beam splitter cube to thin polarizer (TFPN-1064-PW-1025-UV, CVI).

Also, I should mention the history that we experienced deformation of the beam shape and the beam pointing unstability by air turbulence. At the first time we build a setup for 1070 nm optical dipole trap, we planned to control the beam power of 1070 nm laser by an AOM. However, when an incident power of the laser was larger than about 30 W, beam profile was deformed showing flattened shape near the top of the Gaussian profile. And, the AOM we used was operated by rf power of 3.7 W which cause heating and we actively stabilized to 45°C. The temperature difference between the AOM and nearby air cause air turbulence which cause unstablity of the beam pointing. We could use another AOM made with fint glass, but we decided any option with crystal may cause heating and thus an air turbulence. Therefore, currently we do not use AOM for the high power IR laser.

3.3.2 532 nm optical dipole trap and optical lattices

The 532 nm optical dipole trap serves as an additional dipole for the crossed configuration which increases the density of atoms for forced evaporative cooling. We use fiber laser based single frequency mode 532 nm laser by IPG Photonics (GLR-20). The power of the laser is PID stabilized and controlled by AOM (MTS110-A3-VIS, AA opto electronic). After transmit the AOM, the beam is fiber coupled and delievered to near the science chamber. We use an ordinary polarization maintaining fiber (P3-405BPM-FC-2 and P3-488PM-FC-2, Thorlabs), and the maximum power from the fiber output is about 1.8 W which is sufficienct to provide trap depth of 10 μK with beam waist of 55 μm. So far, aging of the fiber is not observed. Instead, we observed a distortion of beam profile after the polarization beam splitter cube (PBS25-HP-532) even though the product was for high power applications and our intensity was not higher than the damage threshold.

Optical lattices

We generate optical lattices by the same laser. The schematic optical lattice setup is depicted in Fig. 3.10. Since we use a hexagonal science chamber, we cannot produce rectangular lattices on horizontal plane by simple retro-reflecting setup. Instead, we generate one horizontal lattice by retro-reflecting setup, and the other horizontal lattice by overlapping a single beam to the 532 nm dipole trap which is controlled by the AOM operated by the same rf source to prevent *moving* lattice. The waist of the lattice beams are 85 μm and the maximum trap depth is 50 E_R. The frequencies of each lattice laser is $\sim$10 MHz detuned so the interference between lattice beams of different directions can be neglected.

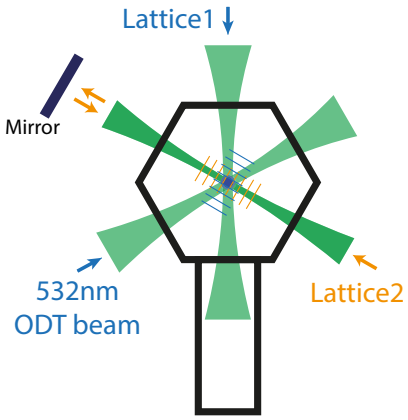

Figure 3.10: Schematic diagram of optical lattice setup near the science chamber. Lattice1 forms lattice potential with 532 nm optical dipole trap. Lattice2 is retro-reflected and lattice3 which is not depicted in the figure is vertically aligned and is also retro-reflected.

3.4 Vacuum system

In this section, I will describe the vacuum part of our ytterbium quantum gas machine. Figure 3.11 depicts overall vacuum system. The vacuum system can be divided into three parts: Oven, Zeeman slower, and main chamber.

3.4.1 History of the vacuum system

The prototype of our vacuum system was made mainly by Min-Seok Kim and Min-Sik Kwon. The vacuum of the main chamber was $\sim 1 \times 10^{-10}$ Torr. With that system, in 2014, we achieved our first Bose-Einstein condensate of ^{174}Yb atoms and degenerate Fermi gas of ^{173}Yb with $T/T_F = 0.8$ [105].

As we planned to improve our vacuum part of the machine at the end of 2014, we had a critical leak in oven part and the vacuum of the oven part

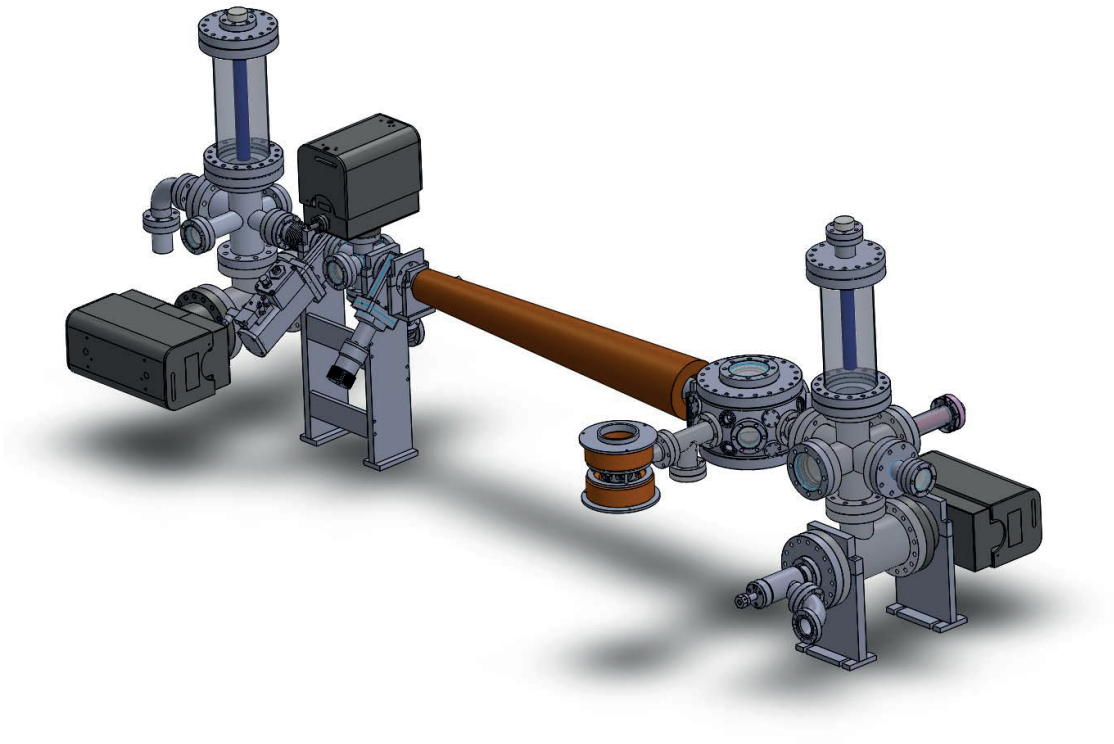

Figure 3.11: CAD drawing of the whole Yb machine.

rose to $\sim 1 \times 10^{-7}$ Torr from 1×10^{-11} Torr because of an unstable support of a heavy ion pump magnet. We decided to reassemble the oven part and to ameliorate main chamber vacuum to make lower vacuum than 1×10^{-10} Torr. We built a new Zeeman slower because we suspected the vacuum component of the Zeeman slower as a reason of bad vacuum and the pumping body of the main chamber is replaced for the same reason. And, we planned to attach a new appendant hexagonal chamber besides the main chamber which was not exist at that time. As a result, we constructed the whole vacuum system again. In following subsections, I'll introduce the newly constructed vacuum system.

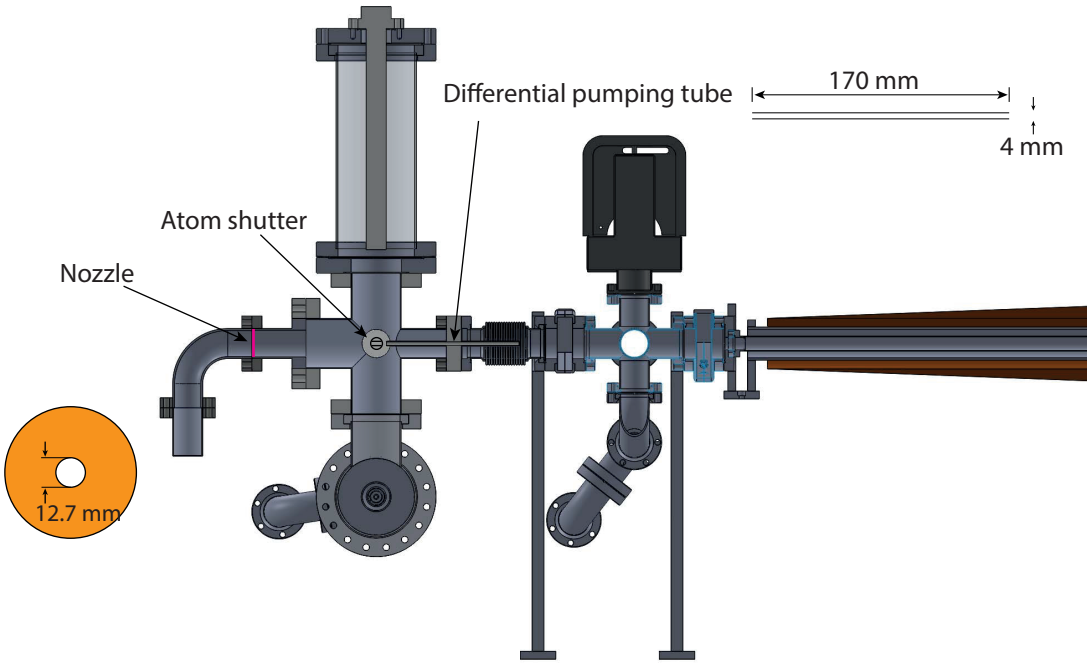

Figure 3.12: CAD drawing of the Yb oven part. The pink line is the position of the nozzle. The insets are the dimensions of the differential pumping tube and the nozzle.

3.4.2 Oven

Figure 3.12 shows CAD model of our oven part. The vacuum of the oven part is maintained by 75 L/s ion pump(Titan 75S, Gamma vacuum) and Ti sublimation pump(9160050, Agilent). The nominal vacuum is $\sim 1 \times 10^{-9}$ Torr at operating condition where the temperature of the Yb cup is 380°C and it drops to $\sim 1 \times 10^{-9}$ Torr at rest condition where the temperature of the cup is 180°C.

Ytterbium metal chunks are loaded in the cup. The cup is heated by ceramic heating band and is surrounded by glass fiber ribbons. The operating temperature of the cup is 380°C for side of the cup and 420°C for the elbow, in order to prevent ytterbium atoms attaching out of the cup. The temperature of

the cup bottom is 350°C. There is a thin nozzle plate at the junction of 6-way cross and the elbow whose hole diameter is 12.7 mm. The differential pumping tube between the oven and Zeeman slower guides atomic beam flux to the main chamber.

3.4.3 Zeeman slower

The Zeeman slower part is connected to the oven part via a bellow. There is 6-way cross which connects the oven part, the Zeeman slower, an angle valve, two viewports, and a 45 L/s ion pump. The nominal pressure of this part is 7×10^{-11} Torr. The two viewports have not used until now but can be used for a spectroscopy of atomic beam source. The main chamber, the oven and the Zeeman slower part can be isolated by two gate valves.

The Zeeman slower coil is wound on a 750mm-long hollow stainless tube. The long vacuum part of the Zeeman slower, whose one end is 1.33" and the other end is 2.75", is inserted into the tube, so we could bake out the vacuum part without concerning the maximum temperature of the coils. Due to slight mismatch of support lengths, long vacuum part is a little bent in a way that the direction of the atomic flux can be affected. This effect is compensated by tuning the aiming of the differential pumping tube which is very critical to the number of the atoms in the MOT.

We isolate Zeeman slower coil and the vacuum part by Sorbothane sheet. It helps to reduce vibrations originated from water flow in the Zeeman slower coils which is very critical in generation of degenerate Fermi gas as I described previously.

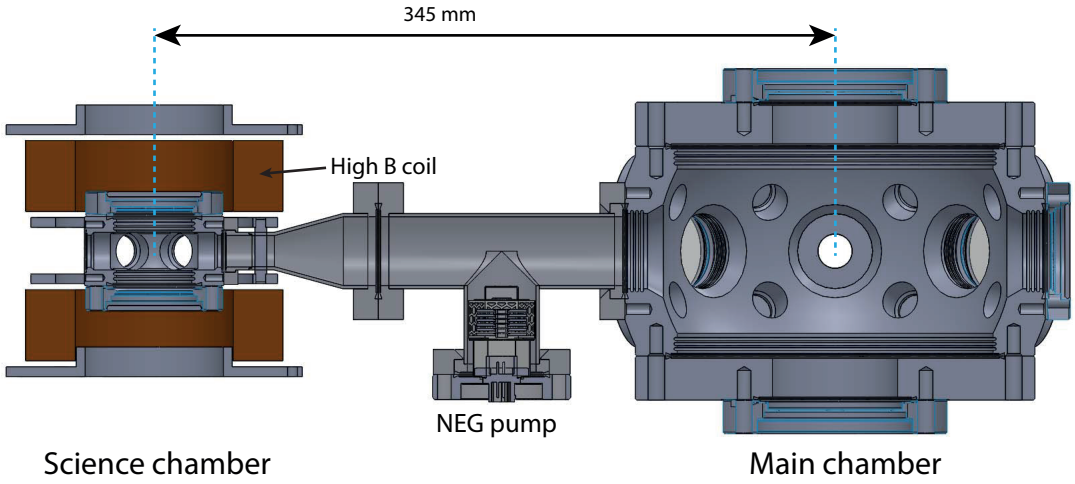

Figure 3.13: CAD drawing of the crosssection of the main chamber and the science chamber.

3.4.4 Main chamber

For the main chamber, we use a commercial spherical octagon chamber (MCF800-ExtOct-G2C8A16, Kimball Physics). There, atoms collected by the MOT and loaded in the ODT. We placed two coils with anti-Helmholtz magnetic field configuration on the top and the bottom of the chamber, additional three pairs of Helmholtz type bias field coils, and slower compensation coils. We used hollow copper wire for the anti-Helmholtz coil and the coil is watercooled through out the loading sequence. There is a pumping body for Ti sublimation pump (TSP) operation, an ion gauge (UHV-24, Agilent) and an ion pump (Titan 75 L/s, Gamma vacuum).

Next to the main chamber, there is a small, hexagonal science chamber (MCF275-SphHex-Cc2A6, Kimball Physics) where most of the experiment after the MOT has been done. The distance between the center of the main chamber and the science chamber is about 345 mm where shorter distance is beneficial for

the optical transport and the stability of a long arm of optical dipole trap laser. In between the two chambers, Non-evaporable getter (NEG, CapaciTorr C35, SAES getters) pump is located. To well split nuclear spin states, we installed Helmholtz type coils on the science chamber which are also wound with hollow copper wire and are watercooled. To minimize the vibration of the water, we isolated the coils and other parts with Sorbothane sheets.

We suffered by a trouble with pressure reading. Right after we finished the whole vacuum job, the lowest pressure reading of the ion pump was 3×10^{-11} Torr. Then it went up slightly, day by day. We tried to find leaks with residual gas analyzer and helium gas, but we couldn't find any. When it finally reached 1×10^{-10} Torr, we fired TSP again but that didn't heal the vacuum. From that time, the nominal pressure reading of the main chamber with the ion pump swings and now it is around 1.0×10^{-9} Torr. We found that there is a large leakage current of the order of 1 μA, and we suspected that TSP poisoned the pump and that our TSP and the ion pump are not far enough. The pressure reading by the ion gauge is quite stable and gives the value of 6.5×10^{-10} Torr which should be slightly higher than the pressure with the ion gauge off.

3.5 Imaging system

For the main chamber, we use typical telescope setup for imaging system with 150 mm and 300 mm achromatic lenses (AC508-150-A-ML, AC508-300-A-ML, Thorlabs). Imaging beam is superimposed on the vertical MOT beam by a long pass dichroic mirror (DMLP425L, Thorlabs) before we enlarge the MOT beam. The imaging beam is separated with the MOT beam by the same kind of dichroic mirror. The size of the imaging beam is 20 mm in diameter which is larger than

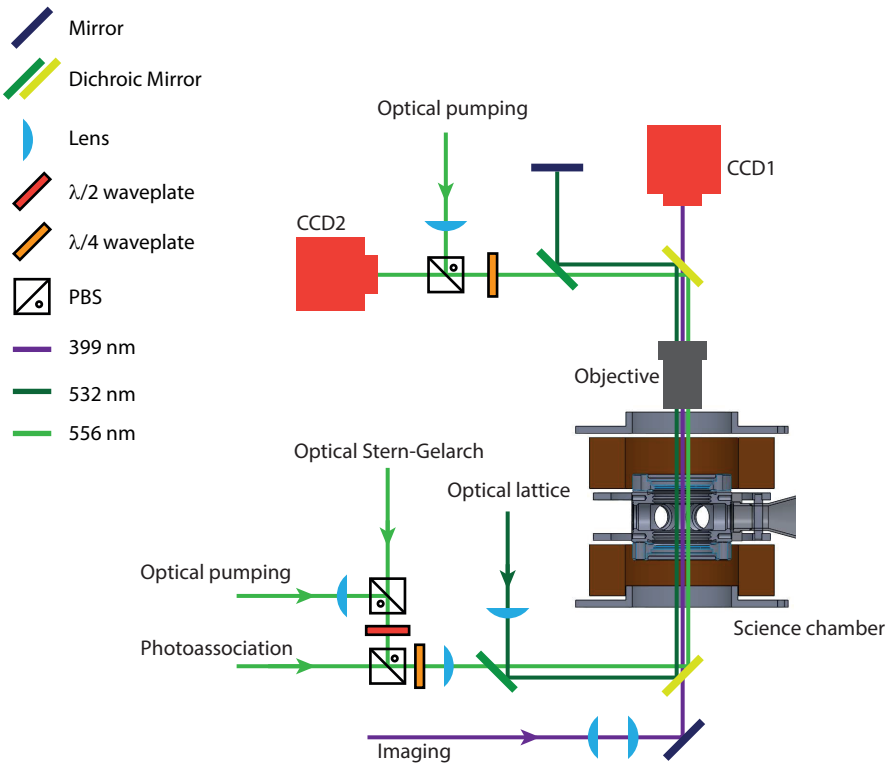

Figure 3.14: Schematic diagram of vertical beam alignment for the science chamber. Six lasers are overlapped to the vertical viewports.

the sample size of 1.3 mm of 20 μK MOT with 15 ms of time-of-flight. The magnification of the imaging setup is 2 and and the region of interest of our camear (Pixelfly usb, PCO) is 4 mm$\times$3.4 mm.

For the science chamber, we use x5 objective lens (375-034-1, Mitutoyo) on the top of the chamber. The resolving power of the objective is 2.12 μm and the smallest line pairs on the 1951 USAF target are resolved. Vertically, six kinds of lasers are aligned so far: (1) imaging beam, (2) σ^+ optical pumping, (3) σ^- optical pumping, (4) optical Stern-Gelarch beam, (5) photoassociation beam, and (6) 532 nm optical lattice beam. Imaging beam is overlapped and separated by a short pass dichroic mirror (SWP-45-RS520-570-TP398.9-2025-UV, CVI Melles Griot Korea) which reflects 532 nm and 556 nm beams and transmit the 399 nm beam. The reason why we chose short pass dichroic is thermal effect of high intensity 532 nm lattice beam. With long pass dichoric mirror, the reflectivity of the 399 nm laser is affected on a region of the mirror which experienced high intensity 532 nm laser. This severly disturbs the absortion imaging. The distance from the center and the topmost part of the chamber is about 30 mm which limits the minimal working distance of our imaging system. The experimental data introduced in this thesis are obtained by Pixelfly usb. Recently, we changed our camera setup to EMCCD (iXon 888, Andor) which provide less noise and high sensitivity.

3.5.1 M camera software

M camera is a C# based basic software developed for taking images from the Pixelfly usb camera and for making optical density (OD) from three images. M camera shows atom numbers of selected reigion of the OD image. Auto calibra-

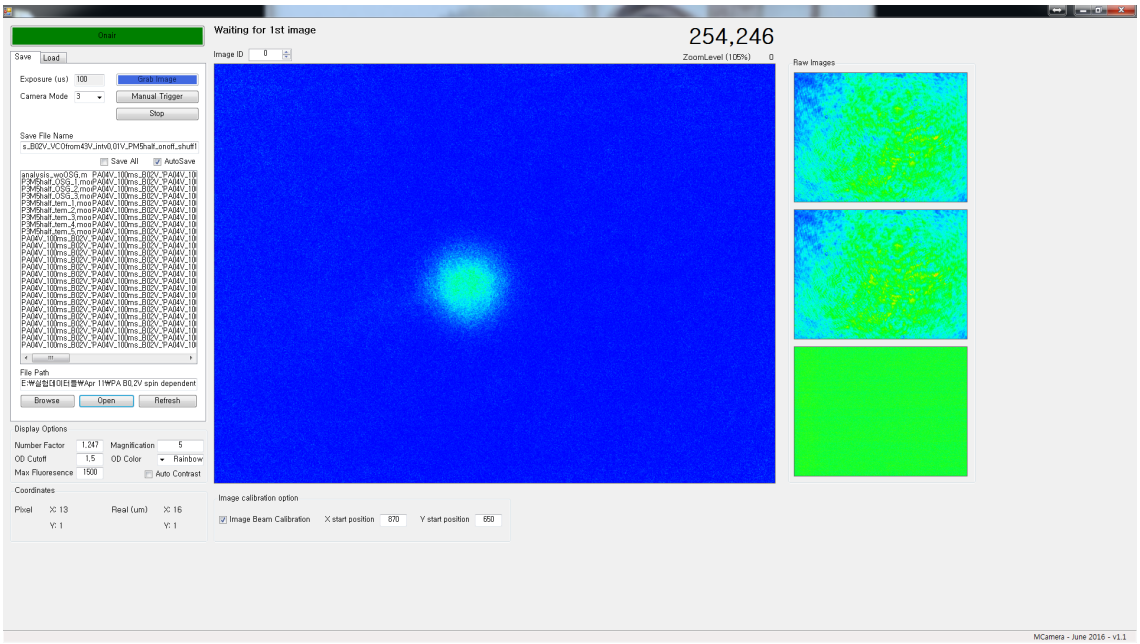

Figure 3.15: Degenerate Fermi gas taken by M camera software.

tion mode is provided which calibrates the power of the imaging beam for the first and the second images.

Chapter 4

Cooling to Quantum Degeneracy

This chapter introduces overall cooling steps from atomic beam to quantum degeneracy. Bulk metalic chunk of ytterbium is heated in the chamber and an atomic beam is produced. The speed of the atomic beam is slowed down from 400 m/s, which covers 85% of atoms according to the Boltzmann distribution, to 15 m/s by the Zeeman slower and captured by the magneto optical trap (MOT). We load atoms on the optical dipole trap (ODT) and then perform evaporative cooling which allows us to have samples of $\approx$ 60 nK. The details about above processes are given in the following sections.

4.1 Zeeman slowing

Zeeman slowing is the most powerful cooling stage among the processes towards quantum degeneracy. The concept of the Zeeman slower is quite simple; compensate the Doppler shifts by the Zeeman shifts so it is possible to slow down atoms, which is slower than a certain velocity, to a target velocity of about 10 m/s. The net momentum transfer is along the direction of the Zeeman slow-

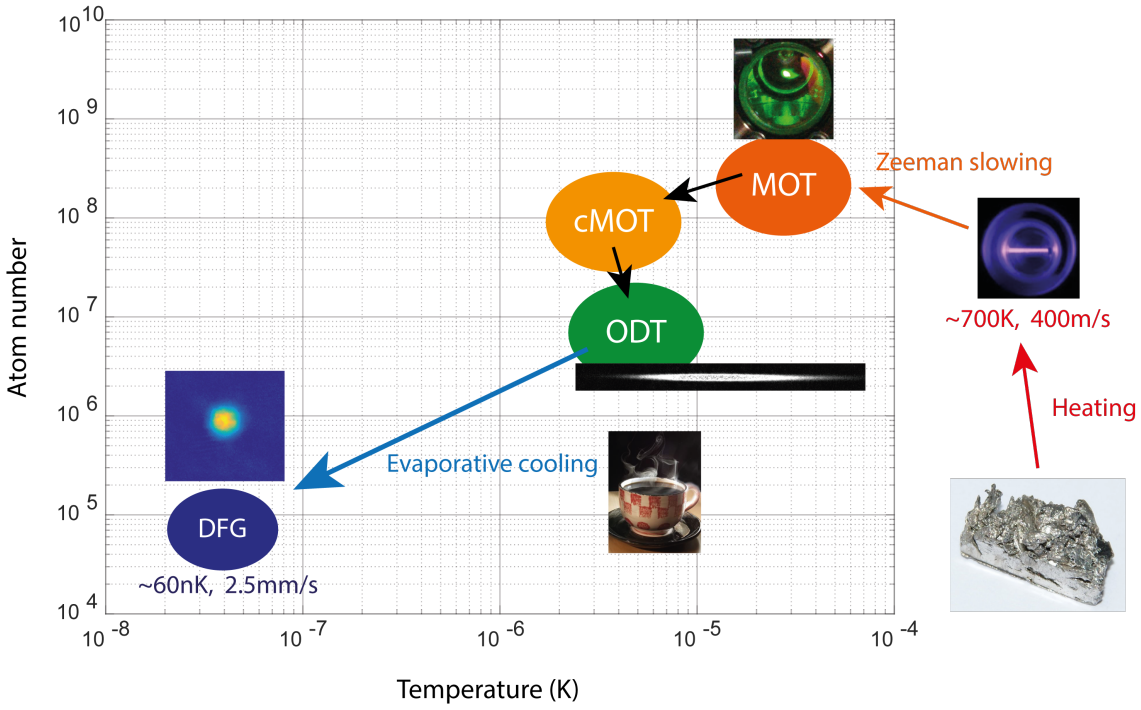

Figure 4.1: Schematic diagram of overall cooling steps from bulk metalic solid to quantum degeneracy.

ing beam since atoms emit photons randomly. With this technique, one can slow down atoms with broad velocity range into narrow and slow velocity which is desirable to trap atoms by MOT.

The magnetic field profile of the Zeeman slower can be obtained by considering the energy conservation of photon scattering process,

$$\frac{1}{2}mv(x)^2 - \frac{1}{2}mv_0^2 = \int F(x)dx \tag{4.1}$$

where m is the mass of ytterbium, $v_{i,f}$ is the initial and the final velocity of an atom, $F(x)$ is the scattering force by photon scattering process. The scattering force is given by $F(x) = \hbar kR$, where $R = \frac{\Gamma}{2}\frac{I/I_s}{1+I/I_s}$ is the scattering rate, I is the intensity of the laser. The intensity of the laser is $I(x) = \frac{P}{\pi r^2(1+\kappa x)^2}$ where P is the power of the laser, r is the radius of the laser at the entrance, and κ is the slope of the beam profile. From this, we can obtain a velocity profile of atoms in the situation where the deceleration by the photon scattering is continously applied. To make atoms be resonant under this velocity distribution, the magnetic field should satisfy $\mu_B g_F m_F B + kv + \hbar\Delta\omega_L = 0$, where $\Delta\omega_L$ is the detuning of the Zeeman slowing laser. The calculated profile of the magnetic field is

$$B = \frac{\hbar}{g_F\mu_B(-7/2)}(\Delta\omega_L - k\sqrt{v_c^2 - 2a_{max}\eta_0 z/(1+2z/L)}) \tag{4.2}$$

where v_c is maximum slowing velocity (400 m/s), $a_{max} = \hbar k\Gamma/2m$, $\eta_0 = \frac{I/I_s}{1+I/I_s}$ and L is the total length of the Zeeman slower. We use a cyclic transition of $^1P_1$ transition, namely, from $F = 5/2$ to $F' = 7/2$, $m_F = -7/2$.

To avoid detrimental photon scatterings at the MOT, owing to the large Γ of the blue transition, we choose increasing field configuration. Our detuning from the cyclic transition is $\Delta\omega_L = 2\pi \times 1$GHz. In case of ^{174}Yb, photon scattering of trapped atoms by Zeeman slowing beam is observed to be negligible.

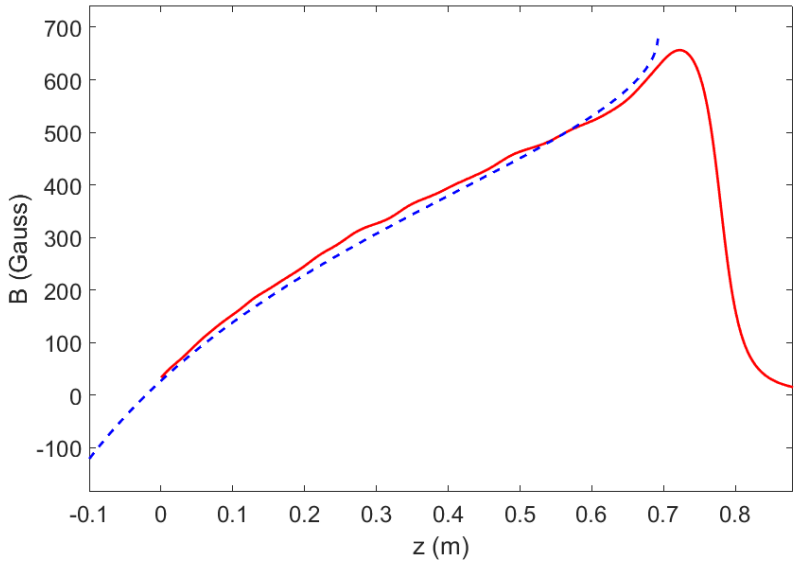

Figure 4.2: The magnetic field profile of our Zeeman slower. The blue dashed curve is theoretically calculated profile and the red solid curve is the optimum field profile which we use in real experiments.

It slightly pushes the atoms from the center and the effects on the number of atoms was not significant.

In case of ^{173}Yb, such a large detuning also cause severe photon scattering to the trapped atoms. That is because the unusual hyperfine structure of the ^{173}Yb. As shown in Fig. 2.2, there is $F' = 5/2$ transition located at -840 MHz from $F' = 7/2$ transition. The detuned laser is only 5.5 Γ away from the $F' = 5/2$ transition and can easily cause photon scatterings. Such photon scattering is not a problem with Zeeman slowing since all atoms are optically pumped to $m_F = -5/2$ state during the slowing process where $F' = 5/2$ transition is forbidden with σ^- polarization of the slowing beam. However, when atoms are magneto optically trapped, the spin of the atoms are mixed and transition to $F' = 5/2$ manifold is not forbidden. The slowing beam induces stronger scattering force than the MOT beam. We could observe trapped atoms only when we turn off the slowing beam.

To avoid this harmful effect on trapped atoms, we project a dark spot on the Zeeman slowing beam. The number of atoms in MOT is very sensitive to the position and the size of the dark spot. We found that the optimal size of the dark spot on the plane of atoms is about by 4 mm in diameter.

For increasing field type of Zeeman slower, residual magnetic field at the center of the trap is not negligible and makes atoms move when the slower is turned off. The longest radius of the Zeeman slower is about 13 cm and it is quite large compared to the distance between the end of the Zeeman slower and the center of the main chamber which is about 20 cm. To reduce residual field, slower compensation coil is used. However, a single compensation coil cannot reduce the field gradient. To further reduce the magnetic field and field gradient from the Zeeman slower, we installed sheets of mu metals right after the end of

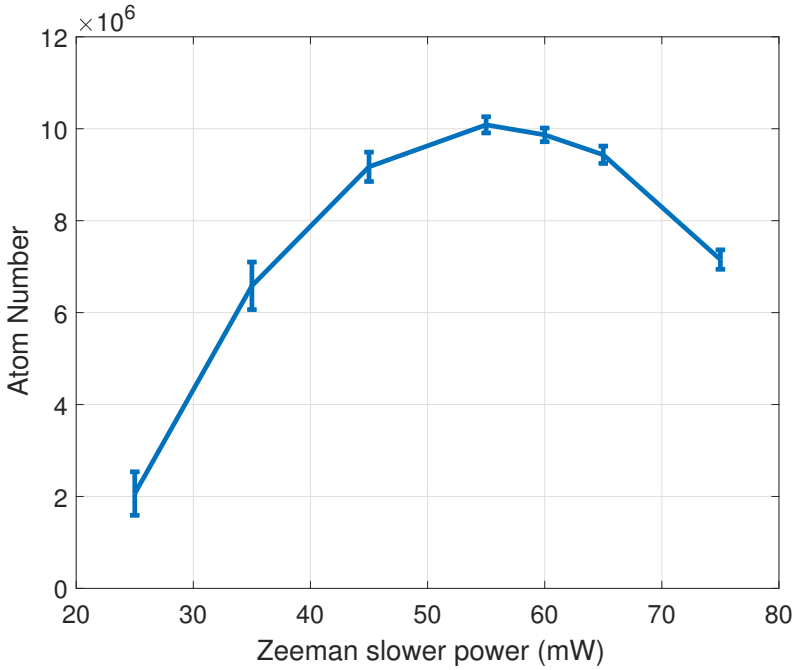

Figure 4.3: Measured atom number in MOT as a function of the power of slowing beam. We observed the decrease in atom number as the slower power exceeds 55 mW. Error bars represent standard deviations.

the Zeeman slower. The current needed to compensate the residual field halved and thus the field gradient from the Zeeman slower is also reduced.

We measure the number of atoms in the MOT for various powers of Zeeman slowing beam. We observed the number of atoms decreases as the power is higher than 55 mW. Possible explanation of this effect is strong pushing by the slowing beam on the trapped atoms and on slowed atoms near the exit of the slower. For slowed atoms near the slower exit, even if the transition to $F' = 5/2$ is forbidden, $F' = 7/2$ transition is strong enough to cause bad effect on the atomic flux. This is also shown in the numerical simulation of our Zeeman slower [106] where the transition to $F' = 5/2$ transition is not considered. Therefore we used

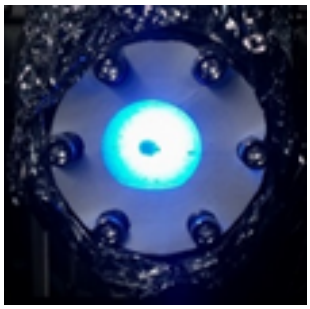

Figure 4.4: The picture of a dark spot imprinted on Zeeman slowing beam. The diameter on the sample plane is about 4 mm in diameter.

slower beam with a power near the optimum value.

4.2 Magento optical trap

The principle of the MOT is to make atoms absorb photons position-sensitively where every photon scattering pushes atoms towards the center by a proper choice of the polarizations and the detuning of the laser under the anti-Helmholtz magnetic field. The MOT allows one to trap atoms in a small spot with temperatures in the order of several times of a Doppler temperature T_d which is defined by $k_B T_d = \hbar\Gamma/2$ where Γ is the linewidth of the transition used for MOT [67, 97]. The doppler temperature of the two main transitions are 696 μK for $^1P_1$ transition and 4.4 μK for $^3P_1$ transition (see Table.2.1).

Magneto optical trap with $^3P_1$ transition

There are mainly two ways of attempting magento optical trap. One is to use $^1P_1$ transition with broad linewidth of 29 MHz and the other is using $^3P_1$ transition with narrow linewidth of 182 kHz. The advantages of the first approach are that the capture velocity of the MOT is higher than the second one, and that

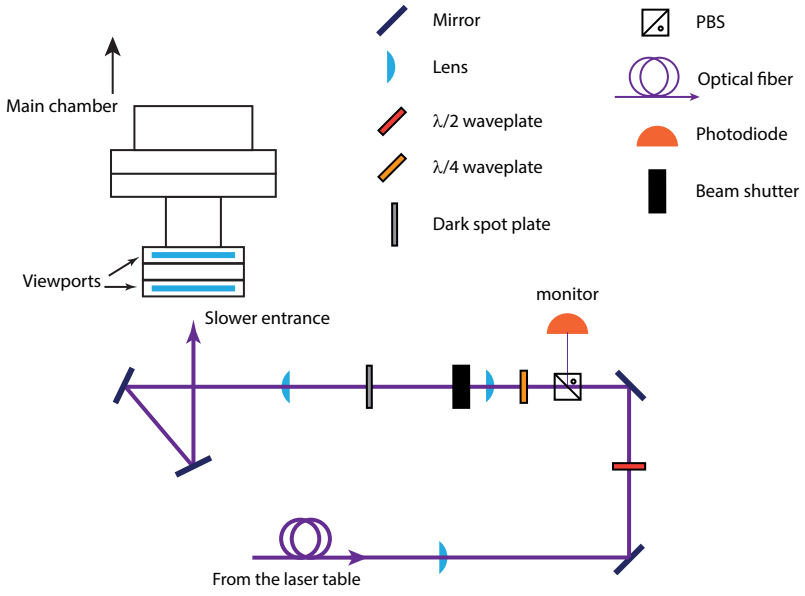

Figure 4.5: Optics for Zeeman slowing beam. A slide glass with a dark spot is located between lenses to block slowing beam from illuminating atoms in the MOT. We installed two viewports in a row to heat up the inner viewports in order to slow down a deposition of ytterbium atoms.

it can gather atoms faster. However, the $^1P_1$ transition is not a perfectly cyclic one and it has leakage paths to the triplet states which restrict the maximum number of trapped atoms to only about 10^7 [107]. Despite some efforts like using repumping laser [108], the gain in number was few tens of percents.

The second solution using $^3P_1$ states have showed better performance except its slow loading rate, which is typically about 15 s. To overcome its small capture velocity, the frequency of the laser is dithered by acousto optic modulator [109]. Thanks to the fact that the $^3P_1$ transition is cyclic, total number of trapped atoms is the order of 10^8 which is ten times larger than the first solution. Also, owing to its narrow linewidth, the temperature of the atoms are much lower. Therefore, we adopted the second approach using $^3P_1$ transition for the MOT.

Note that there is another fancy solution utilizing both transitions. In [110], they use $^1P_1$ beams with "core-shell" beam profile which is overlapped with $^3P_1$ transition lasers. The lasers outside the core provide strong deceleration and the beams penetrating the core trap atoms without leakage path to other states. They succeeded to load 1.5×10^9 atoms of ^{174}Yb with $\tau = 1.2\ s$. We expect implementation of this technique would be helpful to achieve high atom number of the fermionic MOT.

Unusual magneto optical trap for fermionic ytterbium atoms

The magnetic sublevel of the ytterbium is quite different from that of typical alkali-metal atoms (see Fig. 2.2) owing to the lack of electronic spins for the ground state. Especially for fermionic cases, magnetic sublevels for the ground state is very insensitive to the magnetic field compared to the $^3P_1$ states which have non-zero electronic spin. Therefore, unlike alkali-metal atoms like rubid-

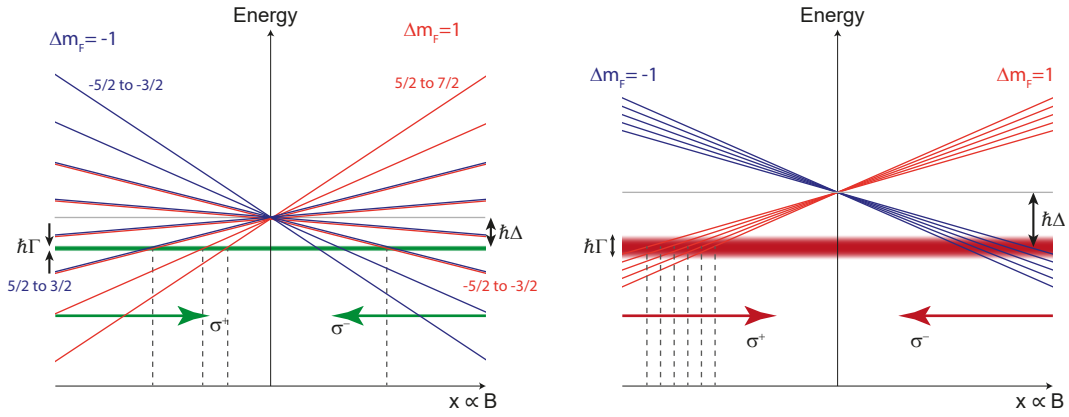

Figure 4.6: Comparision of MOT schemes. Due to small linewidth and large discrepancy of Zeeman splitting of the ground and excited states, ytterbium Fermionic MOT is quite different with rubidium case. See the text.

ium, the energy differencies to excite atoms in different magnetic sublevels of the ground state are very large compared to the linewidth of the laser (see Fig. 4.6) considering typical magnetic field gradient of the order of a several G/cm and beam size of the trapping laser which is about a few tens of milimeters.

This feature is very crucial for the operation of MOT [69,111]. First, the direction of the momentum transfer is not always heading the origin: Though the atoms are in negative coordinate, it can absorb photons coming from the positive direction as shown in Fig. 4.6. As pointed out by [111], the variation of the transition strength ensures that the momentum transfer towards the origin is stronger than the opposite process. For example, if an atom in $m_F = +1/2$ state located at $x < 0$, a photon coming from the negative direction can apply stronger force than the oppsite one (see Fig. 4.6).

However, there are some spin states that cannot be pushed to the origin. Let's consider the $m_F = +5/2$ atoms located at $x < 0$. The atom can only

be pushed by the photons heading towards the positive direction. After the scattering, if the atom is not fast enough to change its spin as it passes the origin, or equivalently, if the atom follows the change of the magnetic field near the origin adiabatically, it should still be in $m_F = +5/2$ state. In this case, it is impossible for atoms to absorb photons coming from the positive direction. Then we lost the atom. Fortunately, despite this loss mechanism, we were able to load atoms in the MOT successfully without implementing other techniques such as applying additional spin mixing beam [111]. We suspect that the temperature of the trapped atom is high enough to cause spin mixing by itself. Because of a similar reason, it is important to choose the direction of the Zeeman slower and an anti-Helmholtz coil in a way that the majority spin of atoms feels strong restoring force of the MOT [99, 111]. Note that the MOT of bosonic atoms, whose spin is zero for the ground state, is operated by the same mechanism as the alkali-metal case due to its simple magnetic sublevels.

Experimental sequence

Experimental sequence of loading atoms in the MOT and the ODT is displayed in Fig. 4.9. We first load ^{173}Yb atoms in MOT for 15 s. The laser frequency is actively broadened by acousto optic modulator by dithering the control voltage of the voltage controlled oscillator. The detuning of the laser is centered at -4 MHz as shown in Fig. 4.8. The lasers are retro-reflected and the atteunation of the intensity of reflected beam is negligible owing to a small saturation intensity of the $^3P_1$ transition. The size of the beam is 20 mm in diameter and the incident powers are 18 mW and 24 mW for horizontal and vertical directions, respectively. The intensities correspond to 41 I_s and 55 I_s. The power of the laser is monitored by a photodiode and is PID-controlled.

After 15 s of the loading sequence, we perform a compression to reduce the size and the temperature of the atoms which is desirable to load on the ODT. First, all coils and Zeeman slowing beam are turned off and we wait 20 ms for atoms to be equilibriate. For another 100 ms, the frequency of laser is narrowed down as the detuning is decreased to -3 Γ. Simulteneously, the power of the laser is decreased to total intensity of 2 I_s. During this sequence, the temperature of the atom is decreased since the effective linewidth of the transition $\Gamma_{\text{eff}} = \Gamma\sqrt{1+s}$ is decreased. Then the magnetic field gradient is increased to 7.9 G/cm in 250 ms and this tightly concentrate atoms around the field zero point. The temperature of the atoms after the compression stage is 20 μK and the number of atoms is about 10^8. Because the force of the vertical trapping beam is small compared to the gravity, the shape of the atoms is vertically squeezed.

	Detuning (Γ)	Intensity (I_s)	Field gradient (G/cm)
Loading	29	273	2.5
Compression	4.3	2	7.9

Table 4.1: Parameters for the MOT loading sequence and the compression sequence. The intensity represents a value for the total six beams.

4.3 Loading on optical dipole trap and optical transport

The atoms are loaded on 1070 nm ODT after the compression sequence. The details about the laser system for ODT are described in Sec. 3.3. The waist of the trap at the center of the main chamber is $(\omega_x, \omega_z) = (64, 21)$ μm, and the

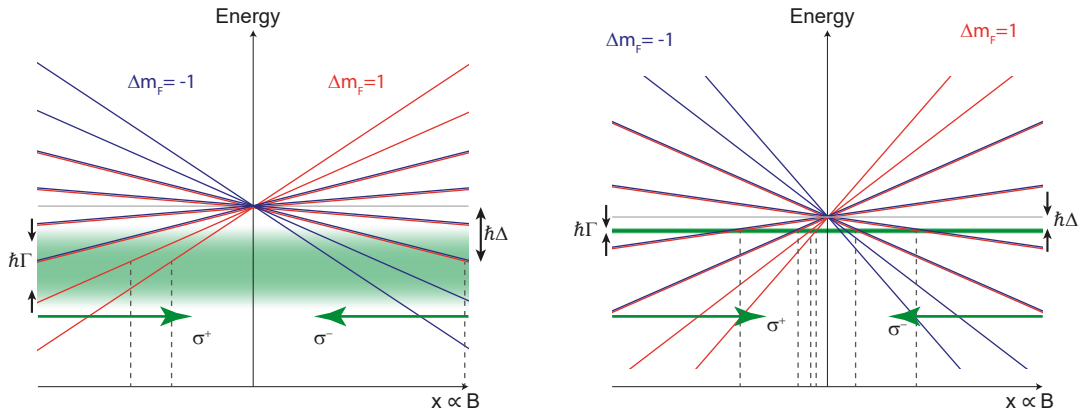

Figure 4.7: Schematic diagram of the frequency broadened MOT and the compressed MOT. To increase capture volume, we actively dither the center frequency of the MOT beams. And to decrease the size and the temperature of the captured atoms, we decrease the detuning and turn off frequency broadening. See the text.

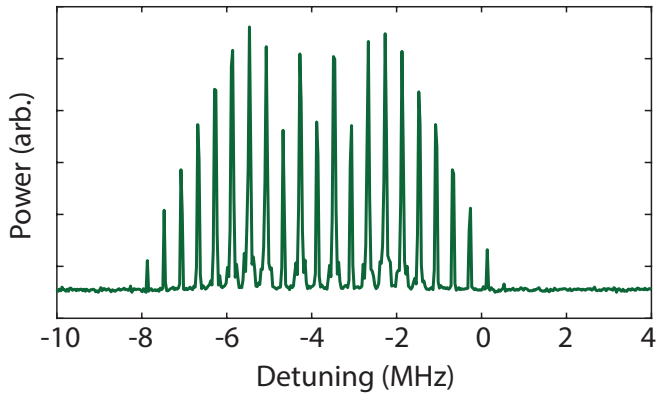

Figure 4.8: The power spectrum of frequency broadend MOT beam. The modulation frequency is 200 kHz and the depth is optimized by numbers of atoms. The scale of the y axis is logarithmic.

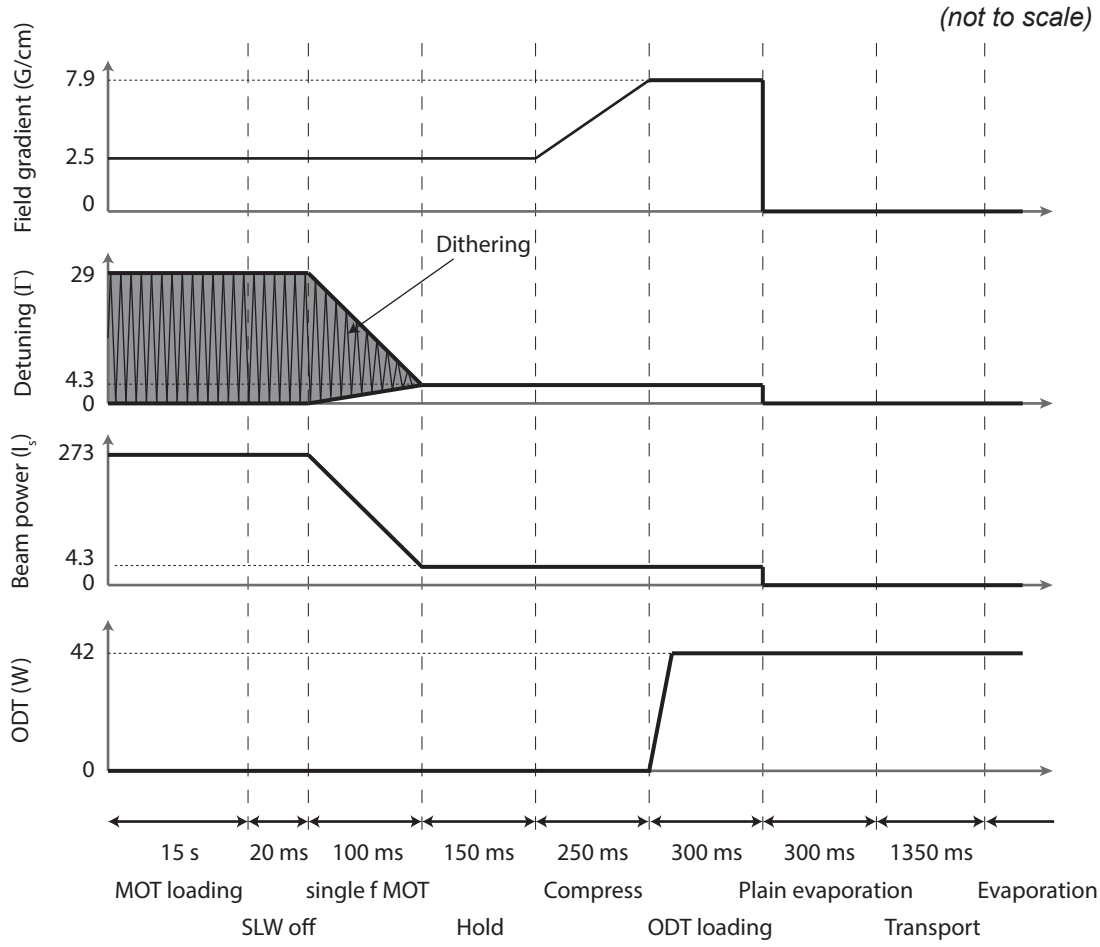

Figure 4.9: Experimental sequence of loading atoms in the MOT and the ODT.

Figure 4.10: The picture of atoms trapped in the MOT. Strong photon scattering by the slowing beam makes a tail of atomic cloud.

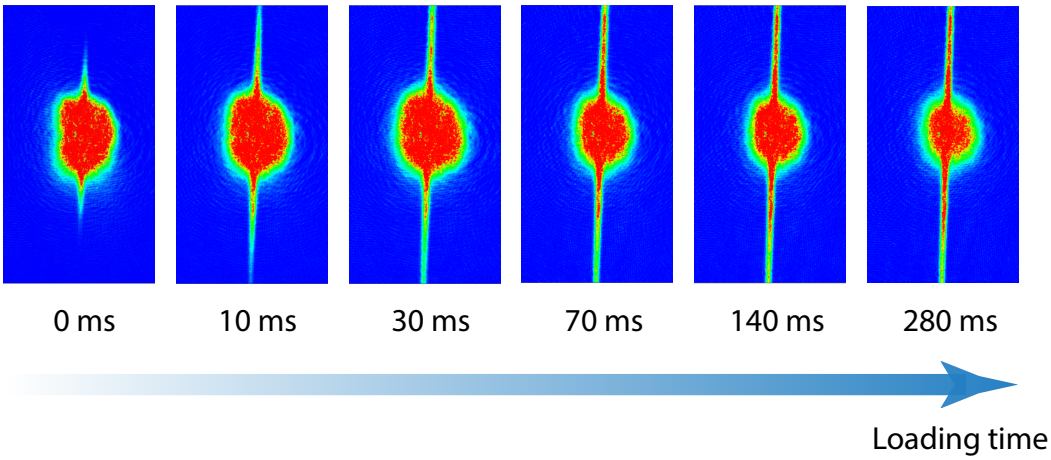

Figure 4.11: The *in situ* image of atoms loaded into ODT. Loading time represents the time when the ODT and MOT were on at the same time, after ODT reaches its final value. As the overlap of MOT and ODT increases which is represented by loading time, the atomic cloud shrinks and elongated along the ODT.

typical maximum power at the loading sequence is 42 W. The trap depth is 540 μK at the center of the trap which is far deeper than the temperature of the compressed MOT.

The power of the dipole trap is linearly ramped up to its final power after the compression step. After the power reaches its final value, the compressed MOT and dipole trap overlaps for 280 ms. The number of loaded atoms is very sensitve to the final power of the MOT beam and the final field gradient, and especially the final detuning of the MOT beam. The number and the temperature of atoms in the ODT is shown in Fig. 4.12. The values are measured after 300 ms of plane evaporation. The temperature of the atoms increases lineary with the power of the dipole trap and the number saturates around 1.2×10^7. From 42 W or more, the power cannot enhance the number but increase the

temperature. Though the temperature is far below the trap depth, trapping volume is insufficient to load more atoms. As we displayed in Fig. 4.11, the size of the ODT is smaller than the size of the compressed MOT. We expect that more efficient loading might be possible if we use larger, better mode matched beam. It is technically possible to load atoms with higher power of the dipole trap, but we use 42 W considering the low gain in number, temperature increase, thermal lensing effect, and thermal damage to the optics. As I mentioned in Sec. 3.3, from this stage, we turn off the water flow for coil cooling in order to reduce vibrational noise which bothers further cooling and stability of the sample condition.

The atoms are optically transported to the science chamber after the loading sequence. The transport time is 1.6 s and we use the maximally smooth curve of the Soloist program for the velocity profile. Further optimization might be possible by considering the axial trapping frequency as depicted in [112].

4.4 Evaporative cooling and quantum degeneracy

After performing the optical transport, we evaporatively cool atoms by reducing the potential depth of the dipole trap. The basic principle of evaporative cooling is to decrease thermal energies by releasing the atoms from the trap. For efficient evaporative cooling, elastic collisional process is necessary to redistribute the thermal energy of the atoms to follow Boltzmann distribution which atoms has to follow in non-degenerate regime. This makes evaporative cooling different from just blowing off atoms which have kinetic energy greater than a

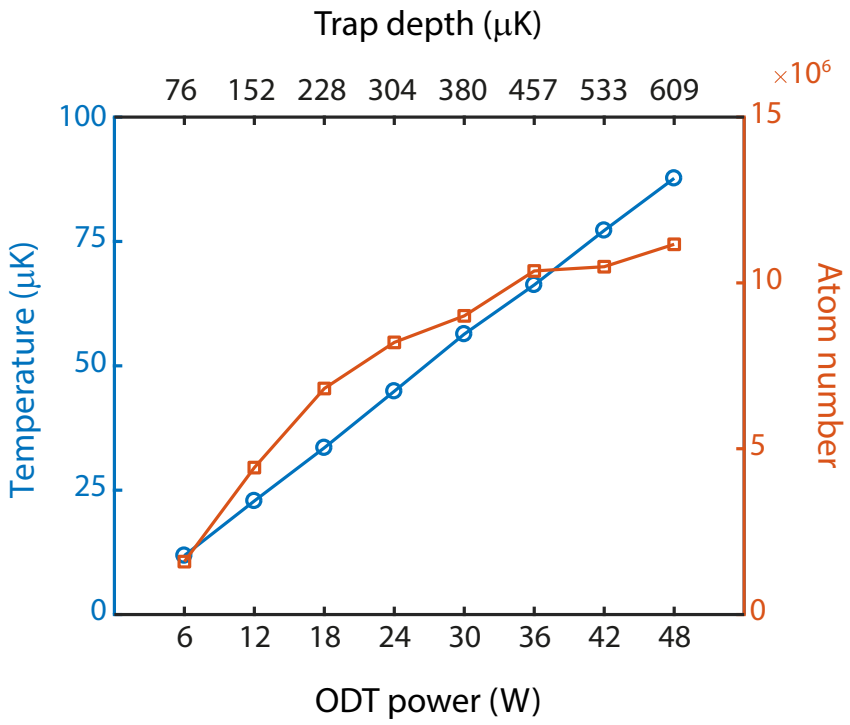

Figure 4.12: The number and the temperature of atoms loaded on optical dipole trap. The temperature linearly increases with the ODT power and the number saturates around 1.2×10^7.

certain value. To achieve high elastic collision rate $R_{el} = n\sigma v$, high density and large s-wave scattering length are desirable where n is the density, σ is elastic crosssection which is proportional to the square of s-wave scattering length a, and v is the mean velocity of atoms. However, considering the inelastic scattering process dominated by three-body collision process which is proportional to $R_{inel} \propto n^2 a^4$ [113, 114], high density and large s-wave scattering length is not always beneficial.

According to [69, 111], a combination large, elliptical beam and vertical ODT is beneficial for efficient evaporative cooling. The first one provides a strong confinement along vertical direction against the gravity and its large trap volume along the horizontal plane is helpful for the early stage of evaporation. The second one controls horizontal trapping frequency and the density. For some reason at the time we setup the ODT, our second ODT is horizontally placed and the angle between the first one and the second one is 60°. Though we cannot control the horizontal trapping frequency and vertical confinement separately, the setup is still good enough to achieve low temperature of $T/T_F \sim 0.1$ with $\sim 10^5$ atoms. We expect that large sample with lower temperature can be generated with vertical ODT setup.

For our atom number on ODT about $\sim 10^7$, a single arm of dipole trap is sufficient for the intial stage of evaporation thanks to the large s-wave scattering length of ytterbium [111]. The transport step to the science chamber conducts a plain evaporation for 1.6 s and then we ramp down the power to the half of its initial value. Then we abruptly turn on another dipole trap whose wavelength is 532 nm and the beam waist is 55 μm. From then, most of atoms are confined in crossed region. The initial trap depth of the two dipole traps are the same. We linearly ramp down the power of the laser for every evaporation step and

we found optimum time for every half of the potential depth. After the reduced temperature T/T_F reaches 0.3, we slightly tune the final potential depth and time to cool further. Total evaporation time is about 5 s.

By evaporative cooling, we achieved degenerate Fermi gas of ^{173}Yb atoms as shown in Fig. 4.13. The Thomas-Fermi distribution is well fitted to radially averaged data for samples with $T/T_F < 1$. Clear suppression of density of the center shows Pauli exclusion of momentum states of degenerate sample. As the temperature does down, the discrepancy of the data points and the Gaussian fittings become large, especially at the wings which means the gas cannot be described by the classical approach. The minimum attainable temperature is $T/T_F < 0.09$ with $N < 10^5$ atoms.

We also achieved a Bose-Einstein condensate (BEC) of ^{174}Yb atoms. However, we did not actively perform experiments with BECs and this thesis is concentrated on the DFG. Detailed explanation about generation of BEC can be found on [99, 105].

4.4.1 Measuring trapping frequencies

We measure the trapping frequencies of the crossed ODT. By giving the sample a jerk with the translational stage which is used for transport to the science chamber, we induce sloshing mode of the sample and measure its oscillation frequencies. Since we do not installed side imaging setup, we measure trapping frequencies of horizontal direction and estimate the value of vertical direction. We found principal axis of the trap by observing the *in situ* density distribution.

The measured trapping frequencies are $(\omega_x, \omega_y) = 2\pi \times (60, 30)$ Hz. The vertical trapping frequency is estimated by the relation $k_B T_F = \hbar\bar{\omega}(6N_\sigma)^{1/3}$

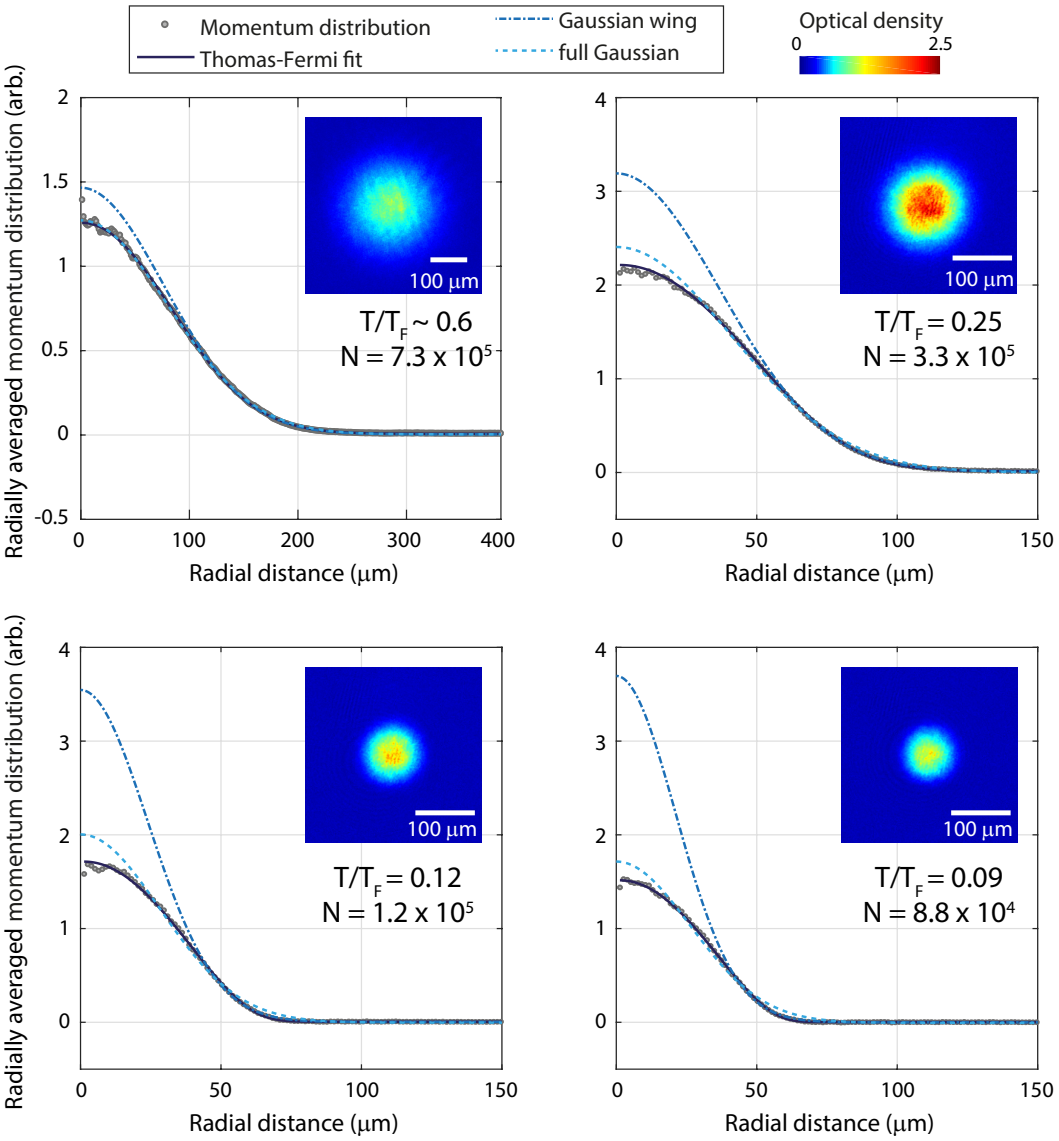

Figure 4.13: Momentum distribution of degenerater Fermi gas of ^{173}Yb atoms. The momentum distributions are radially averaged. As we further cool atoms from (a) to (d), momentum distributions follow the Thomas-Fermi distribution and the Gaussian fittings show large discrepancies. The Gaussian wing curve represents a Gaussian fitting with data only outside of 3 σ where σ is the waist obtained by the full Gaussian fitting. insets: The absoprtion images taken after 15 ms of time of flight.

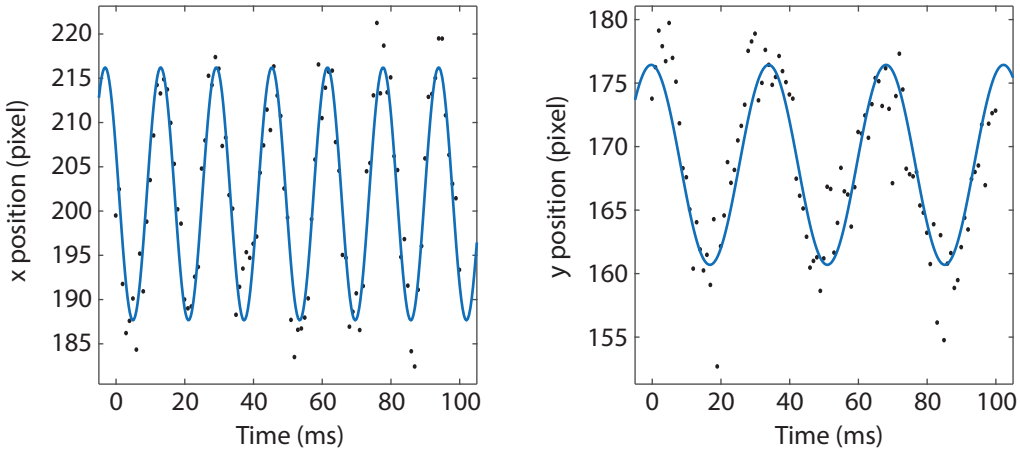

Figure 4.14: Measurement of trapping freuqency. Black dots represent the center of mass of the sample and blue solid curves are sinusoidal fittings.

where $\bar{\omega}$ is geometric mean of trapping frequencies and N_σ is the number of spin σ atoms, resulting $\omega_z = 2\pi \times 450$ Hz.

Chapter 5

Detecting and Manipulating nuclear spin states

In this chapter, we describe experimental methods to detect and to manipulate nuclear spin states of ytterbium atoms including basics of imaging technique. To resolve spin states of a sample, optical Stern-Gerlach separation is implemented. The spin population of the sample is controlled optically and magnetically.

5.1 Absorption Imaging

There are two ordinary ways to get information from the atoms; fluorescence imaging and absorption imaging. We mainly use absorption imaging because it gives clear signal in a quick moment which is order of tens of microseconds. It is possible to acquire the momentum distribution of the atoms via time-of-flight technique which is impossible with fluorescence imaging, technically, because of its long photon integration time. Major disadvantage of absorption imaging is that it destructs the sample every measurement.

The principle of the absorption imaging is very simple. If a resonant light is shined to the atom, atoms make a shadow on it. The reduction of the intensity is proportional to the intensity of the light applied and how easy atoms scatter with the photons which is represented by the scattering crosssection. This is so called the Beer-Lambert law, and the intensity of the light follows

$$I(x,y) = I_0(x,y)\ exp\bigg(-\sigma_0 \int n(x,y,z)dz \bigg) \tag{5.1}$$

where $I_0(x,y)$ is initial intensity, σ_0 is the scattering crosssection, and $n(x,y,z)$ is the density of the sample. The intensity profile of the imaging beam can be acquired by charge coupled device (CCD).

We take total three shots for the absorption imaging: (1) imaging beam with atoms, (2) imaging beam without atoms, (3) without imaging beam for background noise calibration. $(1)-(3)$ gives $I(x,y)$ and $(2)-(3)$ gives $I_0(x,y)$. This gives 2D density profile of the sample $\tilde{n}(x,y) = \int n(x,y,z)dz$ with given $\sigma_0 = 3\lambda^2/2\pi$. Note that the scattering crosssection, which is derived under an approximation that the transition is cyclic, is not have its whole value but only a fraction when the transition is not closed. For example, the scattering cross-section of ${}^1P_1$ transition from $|F, m_F\rangle = |5/2, -5/2\rangle$ to $|F', m'_F\rangle = |7/2, -5/2\rangle$ is smaller than the transition to $|F', m'_F\rangle = |7/2, -7/2\rangle$ by the ratio of the transition strengths.

Using a circularly polarized beam for absorption imaging is not always desirable because the transition strength is very different for the spin states. As shown in Fig. 5.1, the transition strength of weakest transition is 21 times smaller than the strongest one which cause severe underestimation of the number of atoms. To image a spin balanced sample, linearly polarized imaging beam is beneficial thanks to its rather balanced transition strengths for each spin. We

use linear polarization which is the equal mixure of σ^+ and σ^- so that the ratio of the transition strengths are $(11, 10, 8, 8, 10, 11)$ for $m_F = -5/2, \cdots, 5/2$.

Our exposure time of the imaging process is 100 μs and the intensity of the imaging beam is 0.02 I_s which is small enough to safely apply Beer-Lambert law. During the exposure time, photon scattering event occurs 28 times on average, which means most of atoms are finally in stretched states by optical pumping. This further reduce the unbalance of transition strengths otherwise the number of equal spin mixture of atoms are underestimated by a factor of 1.4.

5.2 Fluorescence Imaging

Other research groups use fluorescence imaging to detect position of atoms in optical lattices. They apply an imaging beam which cause fluorescence and an additional cooling beam to prevent atoms from heating induced by an imaging beam [115]. Or, other group choose wavelength of the optical lattice which gives deep potential for $^1P_1$ state [116]. So far, our experiment does not require non-destructive imaging technique and the fluorescence imaging is not implemented.

5.3 Detection of nuclear spin states

In this section, we describe three methods of detection of nuclear spin states. The first one is optical Stern-Gerlach (OSG) separation which spatially separates the spin components by optical potential gradient.

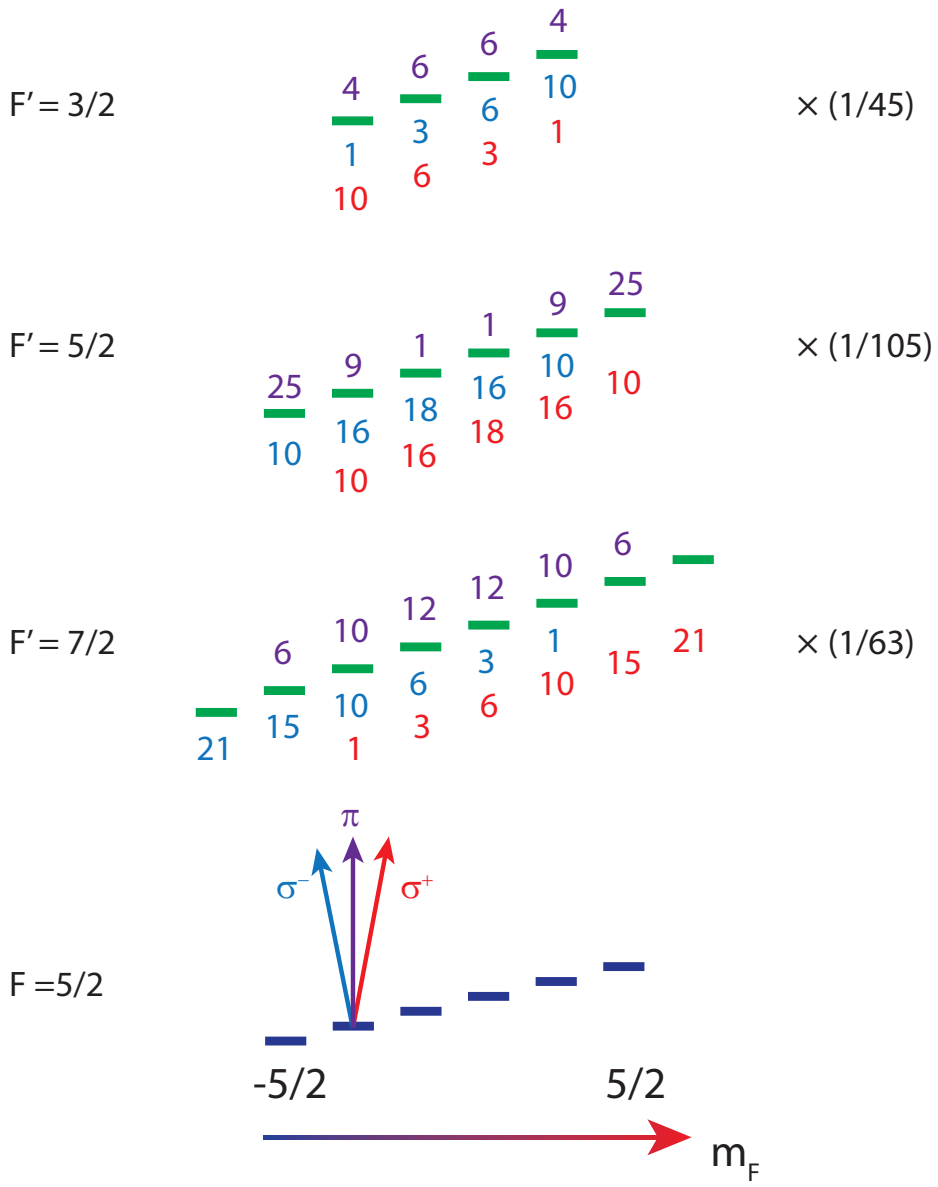

Figure 5.1: The transition strengths for ${}^3P_1$ and ${}^1P_1$ transitions. Note that the transition strength is the same for both cases because the Clebsch-Gordan coefficients do not depend on the S', which is the spin of an excited state.

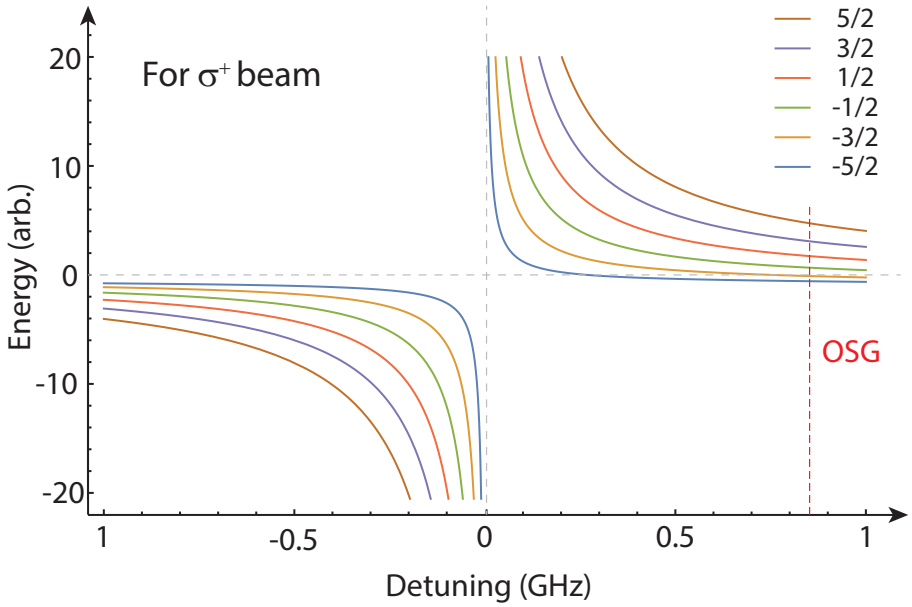

Figure 5.2: Optical potentials applied by a near resonant beam for ${}^3P_1$ $F' = 7/2$ transition. The red dashed line represents the detuning of an OSG beam.

5.3.1 Optical Stern-Gelarch separation

Due to lack of the electronic spin of the ground state, it is pratically impossible to spatially resolve spins of the sample by ordinary magnetic Stern-Gerlach separation. Instead, using an optical field, one can separate the spins and image them separately. This is so called optical Stern-Gerlach (OSG) separation.

The principle of the OSG is to utilize gradient of spin-dependent optical potential of a beam. Figure 5.2 shows relative optical potentials for the ground states. If we place atoms on the slope of an OSG beam as displayed in Fig. 5.3, each spin feels different potential slopes, or forces. After few milliseconds of time of flight, the atoms will fly different distances according to their spins, so we can resolve the spin states of a sample. Our OSG beam is 860 MHz blue detuned from ${}^3P_1$, $F' = 7/2$ transition. This detuning helps to resolve all 6 spins

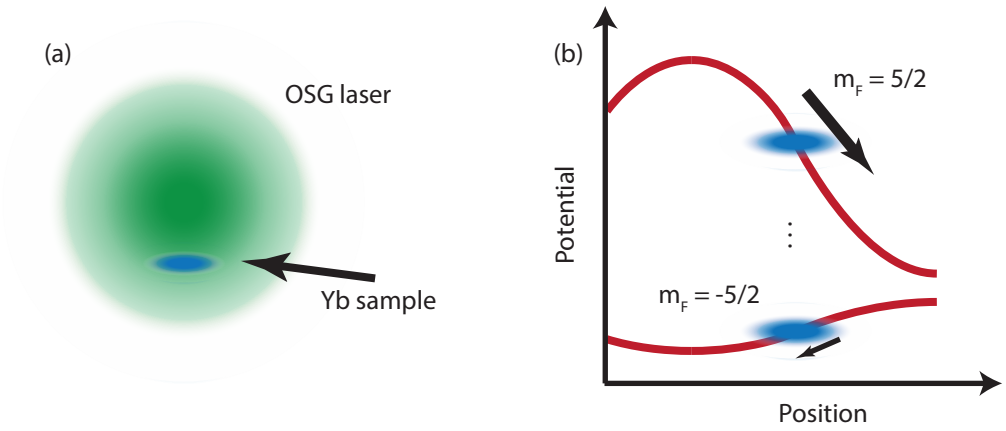

Figure 5.3: Schematic diagram of the princple of OSG. (a) If atoms are located on the slope of an OSG beam, (b) potential gradient is applied according to spins.

because an attractive potential can be applied to a spin component and nearly zero potential is applied for another one.

Figure 5.4 shows exemplery image of OSG. Each blob corresponds to a single spin as depicted in the figure. The beam is typically applied for 4 ms and the images are taken after another 5 ms of time of flight. The separation of spins are very sensitive to the beam power and the relative position of an OSG beam and atoms. The contrast of the outermost cloud can be improved if we use larger, elliptical beam and if we reduce an optical pumping effect of OSG, which will be discussed below, is reduced. And, the small *in situ* sample size would be preferred to have clear signals since the same force is exerted to atoms, simultaneously. Otherwise, the force applied is different depending on the position of an atom and the signal would be rather blurred. In this sence, the vertical separation is beneficial as in [69].

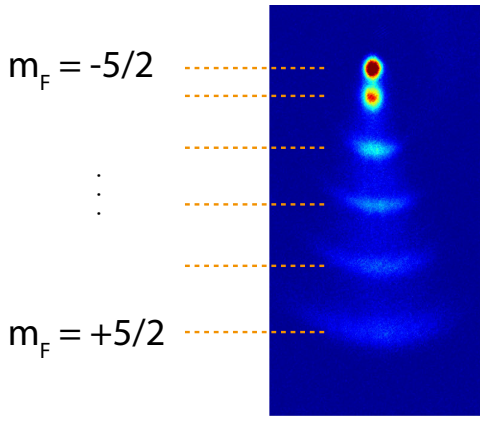

Figure 5.4: A typical optical Stern-Gerlach image for spin balanced sample.

Optical pumping effect of OSG light

Despite its far detuning, OSG beam can also induce optical pumping. The intensity of the OSG light is about 2×10^5 I_s which yields scattering rate of 1.2×10^3 /s. During 4 ms of OSG stage, 4.7 photons can scatter to atoms on average. The far flying spins, the worse the effect due to stronger transition strengths. The reason why far flying spin components are broader can be attributed to this effect. And, remained atoms in between the centers of spin blobs are clearly observed in OSG images of optically pumped sample as shown in Fig. 5.5. We suspect that they changed their spins during OSG so they fly shorter distances than the majority clouds of the spin. So we expect the efficiency of spin manipulation is underestimated.

5.3.2 Spin dependent imaging with $^1P_1$ transition

One drawback of OSG is that the method inevitably destroys information on the momentum space. It is possible to resolve spin states of the sample by applying

magnetic field and using detuned imaging laser. Since the linewidth Γ of the imaging transition ($^1P_1$) is as large as 29 MHz and we need strong magnetic field to split spin states by several Γ. To separates resonant frequencies by 5Γ between adjacent spin components, 350 G is required which can be easily implemented with our setup. We expect that further laser setup would allow us to measure atoms spin-selectively.

5.3.3 Spin dependent imaging with $^3P_1$ transition

With $^3P_1$ transition, whose linewidth Γ is as narrow as 182 kHz, one can spin-selectively measure atoms with more moderate magnetic field and detuning. It only costs 1.5 G for 1 Γ separation between adjacent spins. Instead, the transition is rather weak and the signal to noise ratio is not as good as that of $^1P_1$ imaging. We tried absorption imaging using $^3P_1$ transition but failed to resolve momentum distribution because of its low signal to noise ratio. Only *in situ* images were well resolved.

5.4 Manipulation of nuclear spin states

In this section, we will cover methods to manipulate nuclear spin states of ^{173}Yb atoms. We introduce three ways to enforce the spin manipulation by (1) optical pumping, (2) oscillating magnetic fields, and (3) Raman transitions.

5.4.1 Optical pumping

Optical pumping is a conventional method to change spin population of atoms. By applying resonant light, one can deplete a population of a target spin. Ac-

cording to a polarization of a pumping beam, we can choose which states are populated. We use a pair of pumping beams where one of them is σ^+ polarization and the other is σ^-. The two optical pumping beams are vertically applied to the sample where the vertical axis is a quantization axis defined by a magnetic bias field.

Owing to its large distinction of the Zeeman splittings between the ground states and the excited states, we can seletively deplete the spin states. Figure 5.5 shows exemplary images of spin-manipulated samples which are spin-resolved by OSG. Beyond the examples in the figure, arbitrary spin combinations can be realized with our optical pumping light.

Since an atom undergoes photon scattering processes during optical pumping, there is always a heating. If an atom needs, roughly say, 3 photons to change its spin states, than additional energy of a photon would be 3×180 nK which is not negligible compared to the temperature of our final sample which is about few tens of nK. So it is advantageous to perform optical pumping at the early stage of evaporation sequence where the temperature of atoms is order of 10 μK. We perform optical pumping process right after the transport is finished. The typical timescales of optical pumping is ~ 100 ms for each pumping process.

To generate spin polarized sample of $m_F = -5/2$ state, we optically pump atoms into $m_F = \pm 5/2$ states with a population ratio of 1:2 to ensure the evaporative cooling works which is forbidden if we prepare only a single spin component. After we finish the evaporative cooling, a blast pulse is applied to clean up remained $m_F = +5/2$ atoms. The blast pulse heat up $m_F = +5/2$ atoms only without affecting $m_F = -5/2$ atoms.

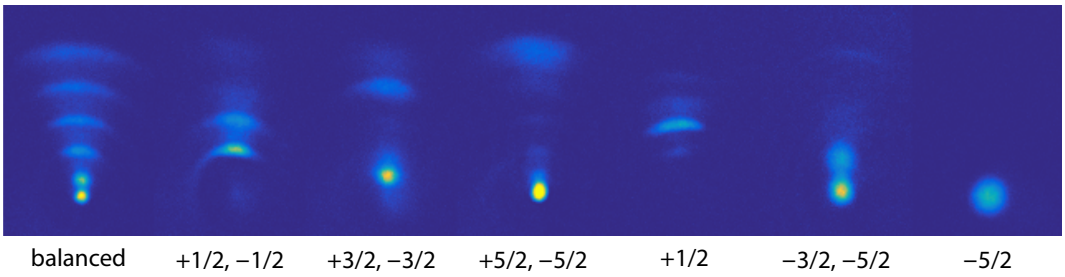

Figure 5.5: An optical Stern-Gerlach image of optically spin-manipulated atoms. Note that the images are taken at different temperatures.

5.4.2 Magnetic transitions

Despite its small magnetic dipole moment, we can drive magnetic dipole transitions by applying an oscillating magnetic fields. We installed a coil to apply a transverse magnetic field which is a superposition of σ^+ and σ^- polarizations with respect to a quantization axis defined by bias magnetic field along z axis. The atoms are prepared in $m_F = -5/2$ states initially and we applied oscillating magnetic field. As the frequency of oscillating magnetic field is varied and we found clear Rabi oscillation between nuclear spins which is resolved by OSG technique as shown in Fig. 5.7. Clear six state Rabi oscillation is observed. The oscillation is sensitive to the driving frequency and only a few Hz of detuning cause dephasing of the oscillation. We could calibrate the bias magnetic field by the resonant frequency.

Precise measurement of light shift

A sensitive responce of Rabi oscillation to the driving frequency is used to measure spin dependent light shift. We applied laser whose polarization is σ^+. The frequency of the laser was +1 GHz detuned from ${}^3P_1$ $F' = 7/2$ transition

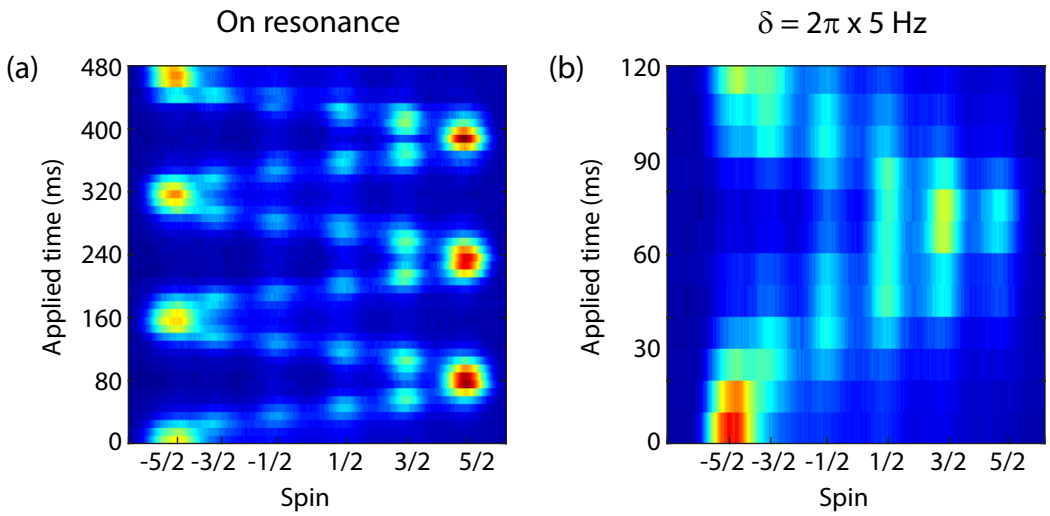

Figure 5.6: The Rabi oscillation between nuclear spin states induced by an oscillating magnetic field. Each horizontal data represents integrated OSG images along the direction perpendicular to the separation.

while we applied the oscillating magnetic field. Due to spin dependency of light shift which makes resonance frequency different, only two level Rabi oscillation is observed at resonance of the $m_F = -5/2$ and $-3/2$ transition.

We observed strong dephasing of Rabi oscillation when the laser power is strong such that the estimated light shift is order of 100 Hz. A possible explanation is that during the slow Rabi oscillation, spontaneous emission is not negligible. Though we couldn't find exact value at strong shift, it is possible to precisely estimate light shift by linear extrapolation from weak field cases. If we could apply stronger magnetic field, with small coils near the sample in the vacuum, it would be easier to measure stronger light shift in a short time.

5.4.3 Raman transitions

Another way to measure a spin-dependent light shift is to utilize Raman tran-

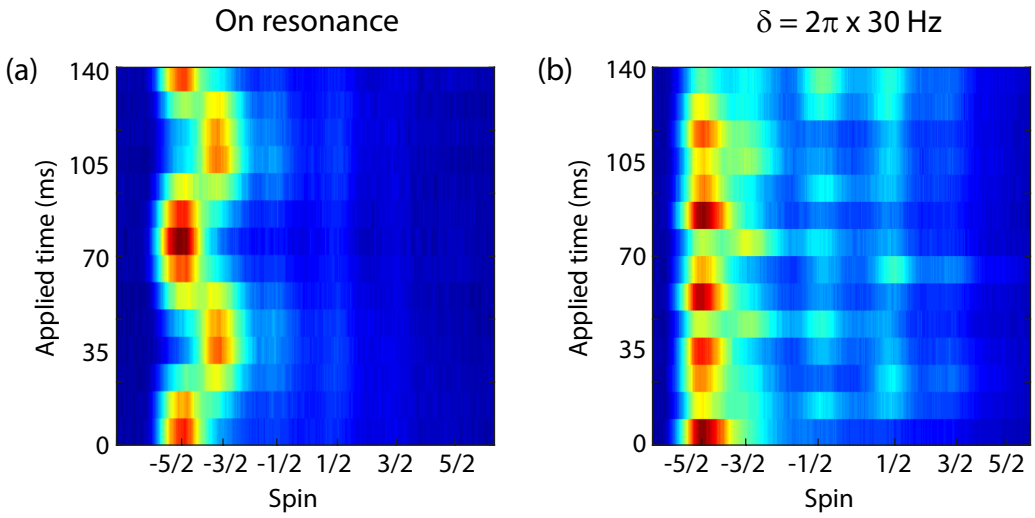

Figure 5.7: Precise measurement of light shift by nuclear spin oscillation. (a) Two level Rabi oscillation is observed because of a spin dependent light shift. (b) Dephased Rabi oscillation signal at a detuning of $2\pi \times 30$ Hz.

sitions [58]. Using copropagating Raman lasers which is detuned by δ, one can induce spin changing Raman process where the momentum transfer is not accompanied. To find detuning which gives minimum Rabi oscillation frequency allows to measure light shift.

Chapter 6

Double resonance of Raman transition

In this chapter, our experimental result on double resonance of Raman transition with ytterbium degenerate Fermi gas is described. This work has been published in the following paper.

- M. Lee, J. H. Han, J. H. Kang, M.-S. Kim, and Y. Shin, *"Double resonance of Raman transitions in a degenerate Fermi gas,"* Phys. Rev. A, **95**, 043627 (2017)

6.1 Introduction

Spin-orbit coupling (SOC) interwines the motional degrees of freedom of a system with its spin part, giving rise to many intriguing phenomena such as the atomic fine structure, the spin Hall effect [117, 118] and topological insulators [119]. In ultracold atom experiments, SOC has been realized using Raman

laser dressing techniques [22,37,120], where a two-photon Raman transition couples two different spin-momentum states. This optical method was successfully applied to many fermionic atom systems [23,24,58,121] and recently extended to two-dimensions [122], boosting the interest in exploring new exotic SOC-driven many-body phenomena [37, 123, 124].

Alkaline-earth-like atoms with two valence electrons such as ytterbium and strontium provide a beneficial setting for studying SOC physics. Their transition linewidth is narrow in comparison to the hyperfine structure splitting, which is helpful to alleviate the unavoidable heating effect due to light-induced spontaneous scattering under the Raman dressing [37, 58] and also to generate spin-dependent optical coupling to the hyperfine ground states. Furthermore, as recently demonstrated with ^{173}Yb atoms [82,83], the interorbital interactions between the $^1S_0$ and $^3P_0$ states can be tuned via a so-called orbital Feshbach resonance [125], which would broaden the research scope of the SOC physics with alkaline-earth-like atoms.

In this chapter, we present momentum-resolved Raman spectra of a spin-polarized degenerate Fermi gas of ^{173}Yb atoms, which are measured in the Raman laser configuration of the conventional SOC scheme. In particular, we measure the Raman spectra over a wide range of magnetic fields as well as laser intensities to investigate the interplay of multiple Raman transitions in the SOC scheme. We observe that two Raman transitions become simultaneously resonant at a certain magnetic field and a doublet structure develops in the spectrum for strong Raman laser intensities. We find that the spectral splitting at the double resonance is quantitatively accounted for by the Autler–Townes doublet effect [126].

In the conventional SOC scheme, since one of the Raman laser beams

has both σ^+ and σ^- polarization components with respect to the quantization axis defined by the magnetic field, the Raman transition from one spin state to another, if any, can be made to impart momentum in either direction along the relative Raman beam propagation axis. In typical SOC experiments, the system parameters are set to make one of the transitions energetically unfavorable such that it can be ignored, but the double resonance observed in this work results from involving both of the Raman transitions. When all the Raman transitions are taken into account, the effect of the Raman laser fields is represented by a spatially oscillating effective magnetic field [127]. We show that our measurement results are consistent with the spinful band structure of the Fermi gas under the effective magnetic field.

6.2 Experiments

Figure 6.1(a) shows the schematic diagram of our experimental apparatus for generating a degenerate Fermi gas of ^{173}Yb atoms [105]. We first collect ytterbium atoms with a Zeeman slower and a magneto optical trap (MOT). For the slowing light, we use a 399 nm laser beam that has a dark spot at its center to suppress the detrimental scattering effect on atoms in the MOT. The frequency modulation method is adopted for the 556 nm MOT beams to increase the trapping volume and capture velocity of the MOT [33]. As a result, more than 10^8 atoms are collected in the MOT within 15 s. We transfer the atoms into an optical dipole trap (ODT) formed by a focused 1070 nm laser beam, where the transfer efficiency is $\approx 13\%$. Then, we transport the atoms by moving the ODT to a small appendant chamber which provides better optical access and allows high magnetic field application, and we generate a crossed ODT by superposing

a focused 532 nm laser beam horizontally with the 1070 nm ODT.

After evaporation cooling, we obtain a quantum degenerate sample in the $F = 5/2$ hyperfine ground state. For an equal mixture of the six spin components, the total atom number is $N \approx 1.0 \times 10^5$ and the temperature is $T/T_F \approx 0.1$, where T_F is the Fermi temperature of the trapped sample. The spin composition of the sample can be manipulated during evaporative cooling with optical pumping or removal of spin states by resonant light. For the case of a fully spin-polarized sample in the $m_F = -5/2$ state, $N \approx 1.2 \times 10^5$ and $T/T_F \approx 0.35$. The trapping frequencies of the crossed ODT are $(\omega_r, \omega_z) = 2\pi \times (52, 450)$ Hz at the end of the sample preparation.

The setup for Raman spectroscopy is illustrated in Fig. 6.2(a). A pair of counter-propagating laser beams are irradiated on the sample in the x direction and an external magnetic field B is applied in the z direction. The two laser beams are linearly polarized in the y and z directions, respectively. With respect to the quantization axis defined by the magnetic field in the z direction, Raman beam 1 with linear y polarization has both σ^+ and σ^- components and Raman beam 2 with linear z polarization has a π component. Thus, a two-photon Raman process, e.g., imparting momentum of $+2\hbar k_R \hat{x}$ by absorbing a photon from Raman beam 1 and emitting a photon into Raman beam 2 changes the spin number by either $+1$ or -1, where k_R is the wavenumber of the Raman beams. This is the conventional Raman laser configuration for SOC in cold atom experiments [22–24, 121].

The Raman lasers are blue-detuned by 1.97 GHz from the $|^1S_0, F = 5/2\rangle$ to $|^3P_1, F' = 7/2\rangle$ transition [Fig. 6.2(b)]. This laser detuning, set between the hyperfine states of $^3P_1$, is beneficial to induce spin-dependent transition strengths for the $F = 5/2$ hyperfine spin states [55, 129]. The frequency differ-

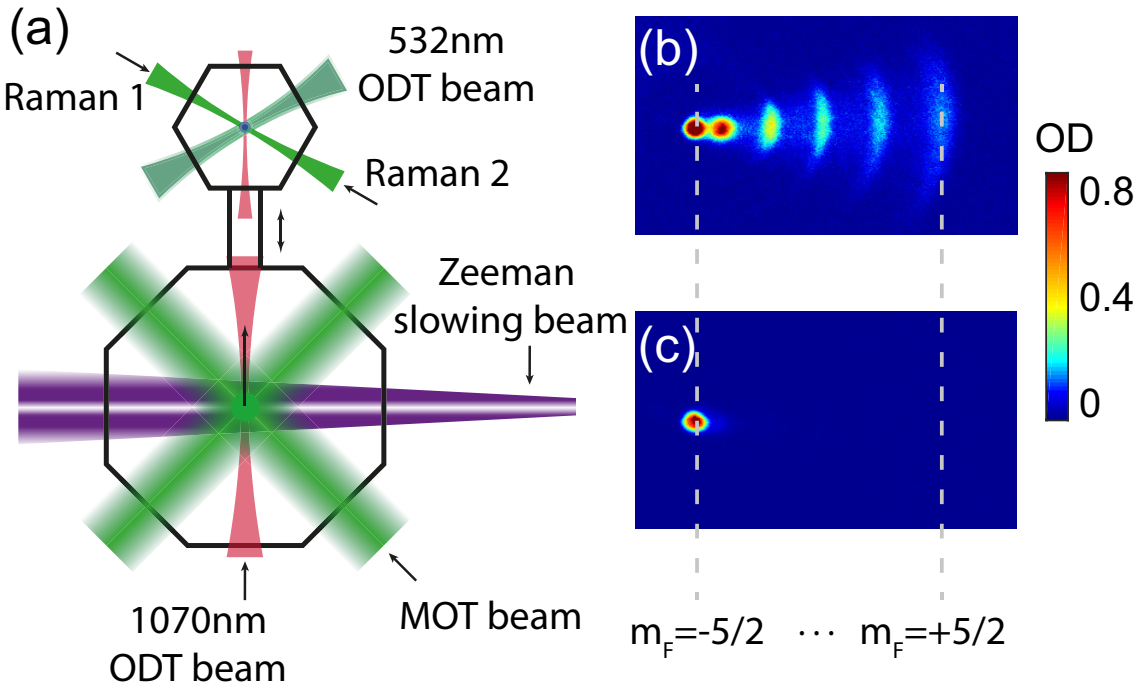

Figure 6.1: (a) Schematic diagram of the experimental apparatus. ^{173}Yb atoms are collected with a Zeeman slower and a magneto-optical trap (MOT), loaded into a 1070 nm optical dipole trap (ODT), and transported to a small hexagonal chamber by moving the ODT. (b, c) Images of atoms after optical Stern-Gerlach spin separation [35, 128]: equal mixture of the six spin components of the $F = 5/2$ hyperfine ground state (b) and fully polarized sample in the $m_F = -5/2$ spin state (c).

ence of the two Raman beams is denoted by $\delta\omega$ [Fig. 6.2(a)]. The two beams are set to the same power P and focused onto the sample. Their $1/e^2$ intensity radii are ≈ 150 μm, which is much larger than the trapped sample size of 30 μm. We assume that the laser intensities are uniform over the sample.

Raman spectroscopy is performed by applying a pulse of the Raman beams and taking a time-of-flight absorption image of the sample. The image is taken at $B = 0$ G along the z-axis with a linearly polarized probe beam resonant to the ${}^1S_0 \rightarrow {}^1P_1$ transition. Two exemplary images are shown in Fig. 6.2(c) and 6.2(d), showing that atoms are scattered out of the original sample with different momenta for different $\delta\omega$. Since the expansion time τ is sufficiently long such that $\omega_r\tau \approx 5$, we interpret the time-of-flight image as the momentum distribution of the atoms. The 1D momentum distribution $n(k_x)$ is obtained by integrating the image along the y direction [Fig. 6.2(e) and 6.2(f)], where $k_x = mx/(\hbar\tau)$ with m being the atomic mass and x the displacement from the center of mass of an unperturbed sample. In our imaging, the absorption coefficient for each spin state was found to vary slightly, within $\approx 10\%$ [Fig. 6.1(b)], which we ignored in the determination of $n(k_x)$.

The normalized Raman spectrum is measured as

$$S_R(k_x) = [n(k_x) - n_{\mathrm{ref}}(k_x)]/n_{\mathrm{ref}}(0), \tag{6.1}$$

where n_{ref} is the reference distribution obtained without applying the Raman beams. In the spectrum, a momentum-imparting Raman transition appears as a pair of dip and peak, which correspond to the initial and final momenta of the transition, respectively. We observe that the spectral peaks and dips exhibit slightly asymmetric shapes, which we attribute to elastic collisions of atoms during the time-of-flight expansion [130]. The Fermi momentum of the sample

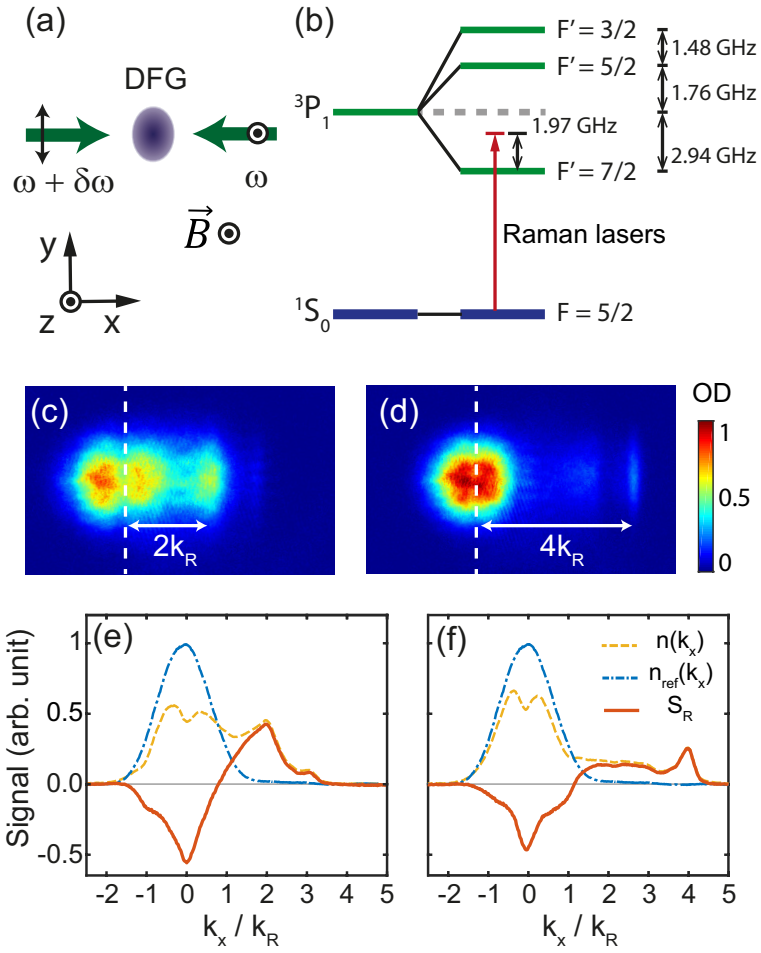

Figure 6.2: Raman spectroscopy of a degenerate Fermi gas (DFG). (a) Raman coupling setup with a pair of counter-propagating laser beams, whose frequency difference is denoted by $\delta\omega$. (b) Energy diagram of the $^3P_1$ state of ^{173}Yb and the relative detuning of the Raman laser. (c, d) Examplary time-of-flight images of Fermi gases after applying a pulse of the Raman beams for $\delta\omega/2\pi = 14.8$ kHz (c) and 29.6 kHz (d). The vertical dashed lines indicate the center of the unperturbed sample. (e, f) 1D momentum distributions $n(k_x)$ of the samples (yellow dashed curve) obtained by integrating the images along the y direction. The normalized Raman spectra $S_R(k_x)$ (red solid curve) are measured as $S_R(k_x) = [n(k_x) - n_{\mathrm{ref}}(k_x)]/n_{\mathrm{ref}}(0)$, where $n_{\mathrm{ref}}(k_x)$ is the reference distribution (blue dash-dotted curve) obtained without applying the Raman beam pulse.

is $k_F/k_R \approx 1.2$ in units of the recoil momentum.

6.3 Results

The atomic state in an ideal Fermi gas is specified by wavenumber k and spin number m_F, and its energy level is given by

$$E(|k, m_F\rangle) = \frac{\hbar^2 k^2}{2m} + g_F \mu_B m_F B + E_S(m_F). \tag{6.2}$$

The first term is the kinetic energy of the atom and the second term is the Zeeman energy due to the external magnetic field B, where g_F is the Landé g-factor and μ_B is the Bohr magneton. The last term E_S denotes the spin-dependent ac Stark shift induced by the Raman lasers. For a Raman transition from $|k_i, m_i\rangle$ to $|k_f = k_i + 2rk_R, m_f = m_i + \Delta m_F\rangle$, which changes the momentum by $2r\hbar k_R$ and the spin number by Δm_F, the energy conservation requires $E(|k_f, m_f\rangle) - E(|k_i, m_i\rangle) = r\hbar\delta\omega$, which gives the resonance condition for the initial wavenumber k_i as

$$k_i = k_R\Big[\frac{\hbar\delta\omega}{4E_R} - \frac{\Delta m_F}{r}\frac{B}{4B_R} - \frac{1}{r}\frac{\Delta E_S}{4E_R} - r\Big], \tag{6.3}$$

where $E_R = (\hbar k_R)^2/2m = h \times 3.7$ kHz is the atomic recoil energy, $B_R = E_R/(g_F\mu_B) = 17.9$ G and $\Delta E_S = E_S(m_f) - E_S(m_i)$. Here we neglect the quadractic Zeeman effect and the atomic interactions which are negligible in our experimental conditions.

We investigate the resonance condition of Eq. 6.3 by measuring its dependence on various experimental parameters. Figure 6.3(a) shows a Raman spectrum measured by scanning the Raman beam pulse duration for $\delta\omega = 4E_R/\hbar$ at $B = 16.6$ G. Spin-polarized samples were used and both of the Raman beams

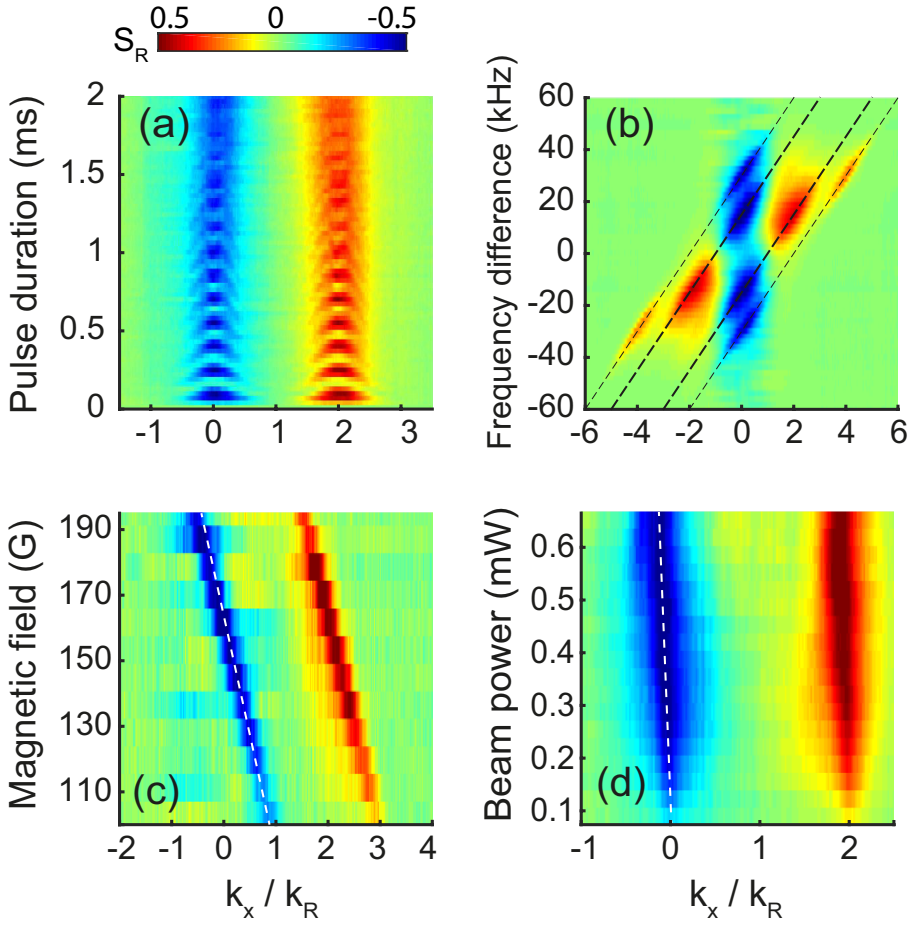

Figure 6.3: Raman spectra measured by scanning various experimental parameters including Raman beam pulse duration t, frequency difference $\delta\omega$, magnetic field B, and Raman beam power P: (a) $\delta\omega = 4E_R/\hbar$, $B =$ 16.6 G, $P = 0.47$ mW; (b) $t = 2$ ms, $B = 0$ G, $P = 1.1$ mW; (c) $t = 2$ ms, $\delta\omega = 13.4E_R/\hbar$, $P = 0.21$ mW; (d) $t = 2$ ms, $\delta\omega = 13.4E_R/\hbar$, $B = 133$ G (see the text for details of the sample condition and the polarization configuration of the Raman beams). The dashed lines in (b) indicate $k = k_R(\frac{\hbar}{4E_R}\delta\omega - n)$ for $n = -2, -1, 1$,and 2, and those in (c) and (d) are guides for the eyes having slopes of $\frac{dk}{dB} = -\frac{k_R}{4B_R}$ and $\frac{dk}{dP} = -0.3k_R/\text{mW}$. Each spectrum was obtained by averaging more than three measurements.

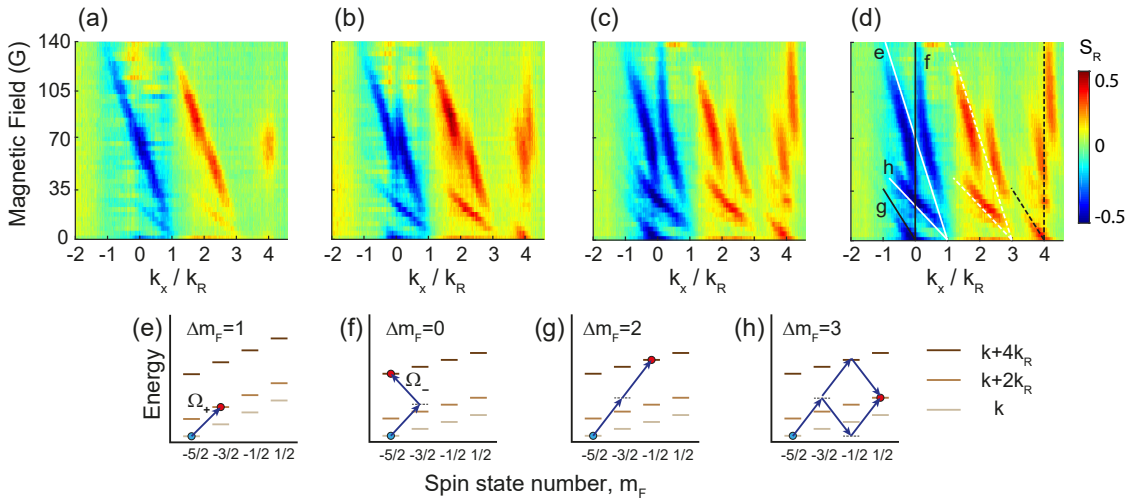

Figure 6.4: Double resonance of Raman transitions. (a–c) Raman spectra of an $m_F = -5/2$ spin-polarized sample as a function of the magnetic field B for $\delta\omega = 8E_R/\hbar$ and various Raman beam powers (a) $P = 0.13$ mW, (b) 0.21 mW, and (c) 0.36 mW. As the Raman coupling strength increases with higher P, a spectral doublet splitting develops at $B = 4B_R \approx 72$ G where the $(r, \Delta m_F) = (1, 1)$ and $(2, 0)$ transitions are doubly resonant. The spectrum in (d) is the same of (c) with the guide lines (solid) indicating the resonant momentum positions for various Raman transitions, which are calculated from Eq. 6.3 without including the ac Stark shift. The dashed lines are the corresponding final momentum positions. (e–h) Diagrams of the Raman transitions observed in the spectra.

were set to linear z polarization to make sure $\Delta m_F = 0$. Momentum-dependent Rabi oscillations are clearly observed and the Rabi frequency is found to be well described by $\Omega(k) = \sqrt{\Omega_0^2 + (\hbar k_R k/m)^2}$ with $\Omega_0 \approx 2\pi \times 7$ kHz. The decoherence time is measured to be ≈ 1 ms, which seems to be understandable with the characteristic time scale for momentum dephasing in the trap, $\pi/(2\omega_r) \approx 5$ ms. In the following, we set the pulse duration of the Raman beam to 2 ms, which is long enough to study the steady state of the system under the Raman laser dressing.

Figure 6.3(b) displays a spectrum of the equal mixture sample in the plane of wavenumber k and frequency difference $\delta\omega$. Here, $B = 0$ G and the Zeeman effect is absent in the measurement. The $r = 1$ and $r = 2$ transitions are identified in the spectrum with their spectral slope of $\frac{dk}{d\delta\omega} = \frac{\hbar k_R}{4E_R}$ and different offsets as predicted by Eq. 6.3. The $(k, \delta\omega) \leftrightarrow (-k, -\delta\omega)$ symmetry of the spectrum indicates that the differential ac Stark shift is negligible in the measurement.

Figure 6.3(c) shows the Raman spectrum of the $m_F = -5/2$ spin-polarized sample over a range of magnetic fields from $B = 100$ G to 195 G for $\delta\omega = 13.4E_R/\hbar$. In the spectral plane of k and B, the Raman transition with $(r, \Delta m_F) = (1, 1)$ appears as a line having the slope $\frac{dk}{dB} = -\frac{k_R}{4B_R}$ as expected from Eq. 6.3. A linear spectral shift is observed with increasing Raman beam power P [Fig. 6.3(d)], which demonstrates the effect of the differential ac Stark shift ΔE_S. In our experiment, $\Delta E_S = E_S(-3/2) - E_S(-5/2) \approx 1.2\ E_R$ for $P = 1$ mW. This is in good a agreement with the Raman beam intensities estimated from the Rabi oscillation frequency $\Omega_+ \propto \sqrt{I_\sigma I_\pi}$, where $I_{\sigma,\pi}$ are the intensities of the Raman beam 1 and 2, respectively. The comparison of ΔE_s and Ω_+ suggests $I_\pi = 0.6 I_\sigma$, which we attribute to a slight mismatch of the beam waists.

Next we investigate a situation where one spin-momentum state is resonantly coupled to two final states simultaneously, which we refer to as a double resonance. When the two corresponding Raman processes are characterized with $(r_1, \Delta m_{F1})$ and $(r_2, \Delta m_{F2})$, we see from Eq. (6.3), neglecting the small ΔE_S term, that the double resonance occurs when

$$\frac{B}{4B_R}\frac{\Delta m_{F1}}{r_1} + r_1 = \frac{B}{4B_R}\frac{\Delta m_{F2}}{r_2} + r_2. \tag{6.4}$$

For the primary transition with $(r_1, \Delta m_{F1}) = (1, 1)$, the double resonance condition is satisfied at $B = \frac{4r_2(r_2-1)}{r_2-\Delta m_{F2}} B_R$.

To observe the double resonance of the $(r, \Delta m_F) = (1, 1)$ and $(2, 0)$ transitions at $B = 4B_R \approx 72$ G, we measure the Raman spectra of the spin-polarized sample in the k-B plane over a range from $B = 0$ G to 140 G [Fig. 6.4]. Here we set $\delta\omega = 8E_R/\hbar$ to have $k_x = 0$ atoms on resonance for the $(2, 0)$ transition, which is insensitive to B for $\Delta m_F = 0$. For low P, the $(1, 1)$ transition appears with the spectral slope of $-\frac{k_R}{4B_R}$ as observed in Fig. 6.3(c) and the double resonance is indicated by a small signal at $(k, B) = (4k_R, 4B_R)$ [Fig. 6.4(a)]. This is understood as enhancement of the second-order Raman transition from $|k = 0, -5/2\rangle$ to $|k = 4k_R, -5/2\rangle$ due to its intermediate state $|k = 2k_R, -3/2\rangle$ being resonant. When the Raman beam power increases, we observe development of a spectral splitting at the resonance [Figs. 6.4(b) and 6.4(c)]. The overall pattern of the high-P spectrum shows the avoided crossing of the spectral lines corresponding to the two $(1, 1)$ and $(2, 0)$ transitions.

Near the double resonance, the system can be considered as a three-level system consisting of $|k, -5/2\rangle$, $|k + 2k_R, -3/2\rangle$ and $|k + 4k_R, -5/2\rangle$ [Fig. 6.5(a)]. For simplicity, we denote them by $|0\rangle$, $|1\rangle$, and $|2\rangle$, respectively. Since the Raman transition between $|0\rangle$ and $|1\rangle$ involves the σ^+ component of Raman beam 1 but

that between $|1\rangle$ and $|2\rangle$ involves the σ^- component, the coupling strengths Ω_+ and Ω_- of the two transitions, respectively, can be different. In our case with ^{173}Yb atoms in the $m_F = -5/2$ state, $\Omega_- = 5.3\ \Omega_+$. Since the coupling between $|1\rangle$ and $|2\rangle$ are much stronger than that between $|0\rangle$ and $|1\rangle$, the observed spectral splitting with increasing Raman beam intensity can be described as an Autler–Townes doublet [126]: two dressed states $|\alpha\rangle$ and $|\beta\rangle$ are formed with $|1\rangle$ and $|2\rangle$ under the strong coupling and their energy level splitting is probed via Raman transitions from the initial $|0\rangle$ state. In the rotating wave approximation, the energy levels of the two dressed states are given by $E_{\alpha,\beta} = \frac{1}{2}[E_1 + E_2 - 3\hbar\delta\omega \pm \sqrt{(E_1 - E_2 + \hbar\delta\omega)^2 + (\hbar\Omega_-)^2}]$, where $E_{1,2} = E(|1,2\rangle)$. The resonant wavenumbers $k_{\alpha,\beta}$ of the initial state $|0\rangle$ are determined from $E(|0\rangle) = E_{\alpha,\beta}$ and for $\delta\omega = 8E_R/\hbar$ and $B = 4B_R$, we obtain $k_{\alpha,\beta} = \pm\frac{k_R}{8\sqrt{2}}\frac{\hbar\Omega_-}{E_R}$. We find our measurement results on the double resonance at $B = 4B_R$ in good quantitative agreement with the estimation [Fig. 6.6(b)]. The coupling strength Ω_- was separately measured from the Rabi oscillation data of the $|0, -5/2\rangle \rightarrow |-2k_R, -3/2\rangle$ transition for $\delta\omega = -13.4E_R/\hbar$ at $B = 166$ G.

The Raman spectra in Fig. 6.4 reveal another double resonance at $B = \frac{4}{3}B_R \approx 24$ G, where the $(r, \Delta m_F) = (2, 0)$ line crosses the $(r, \Delta m_F) = (1, 3)$ line. Although the $(1, 3)$ transition is a third-order Raman transition, its spectral strength is observed to be higher than that of the (2,0) transition. In the intermediate region of $B \approx 35$ G, many Raman transitions are involved over the whole momentum space of the sample and the spectral structure for high Raman laser intensity shows interesting features which cannot be simply explained as crossing and avoided crossing of the spectral lines. It might be necessary to take into account the ac Stark shift effect and a further quantitative analysis of the Raman spectra will be discussed in future work.

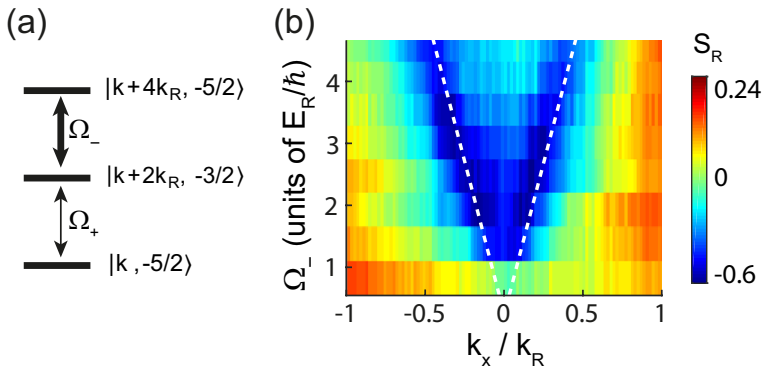

Figure 6.5: Spectral splitting at double resonance. (a) Three atomic states involved in the double resonance at $B = 4B_R$. For a ^{173}Yb atom in the $m_F = -5/2$ state, $\Omega_- = 5.3\ \Omega_+$ and the upper two states are more strongly coupled. (b) Raman spectrum for $\delta\omega = 8E_R/\hbar$ and $B = 4B_R$ as a function of the Raman coupling strength Ω_-. The dashed lines are the theoretical prediction of $k_{\alpha,\beta} = \pm\frac{k_R}{8\sqrt{2}}\frac{\hbar\Omega_-}{E_R}$, which is calculated in the limit of $\Omega_+/\Omega_- \to 0$ (see text).

6.4 Discussion

In the Raman laser dressing scheme described in Fig. 6.2(a), two ways of couplings are allowed between the two spin states because the Raman beam that has linear polarization orthogonal to the magnetic field contains both σ^+ and σ^- components. This means that a Raman transition from one spin state to the other spin state can occur while imparting momentum in either of the x and $-x$ directions. In typical experimental conditions [22–24, 37], one of the couplings is resonantly dominant over the other, giving rise to a form of SOC that has equal strengths of the Rashba and Dresselhaus contributions. However, when the Fermi sea of a sample covers a large momentum space, this approximation cannot be applied and it is necessary to include both of the Raman couplings for the full description of the system. Furthermore, as observed in the previous section, the two Raman couplings can be doubly resonant and play cooperative

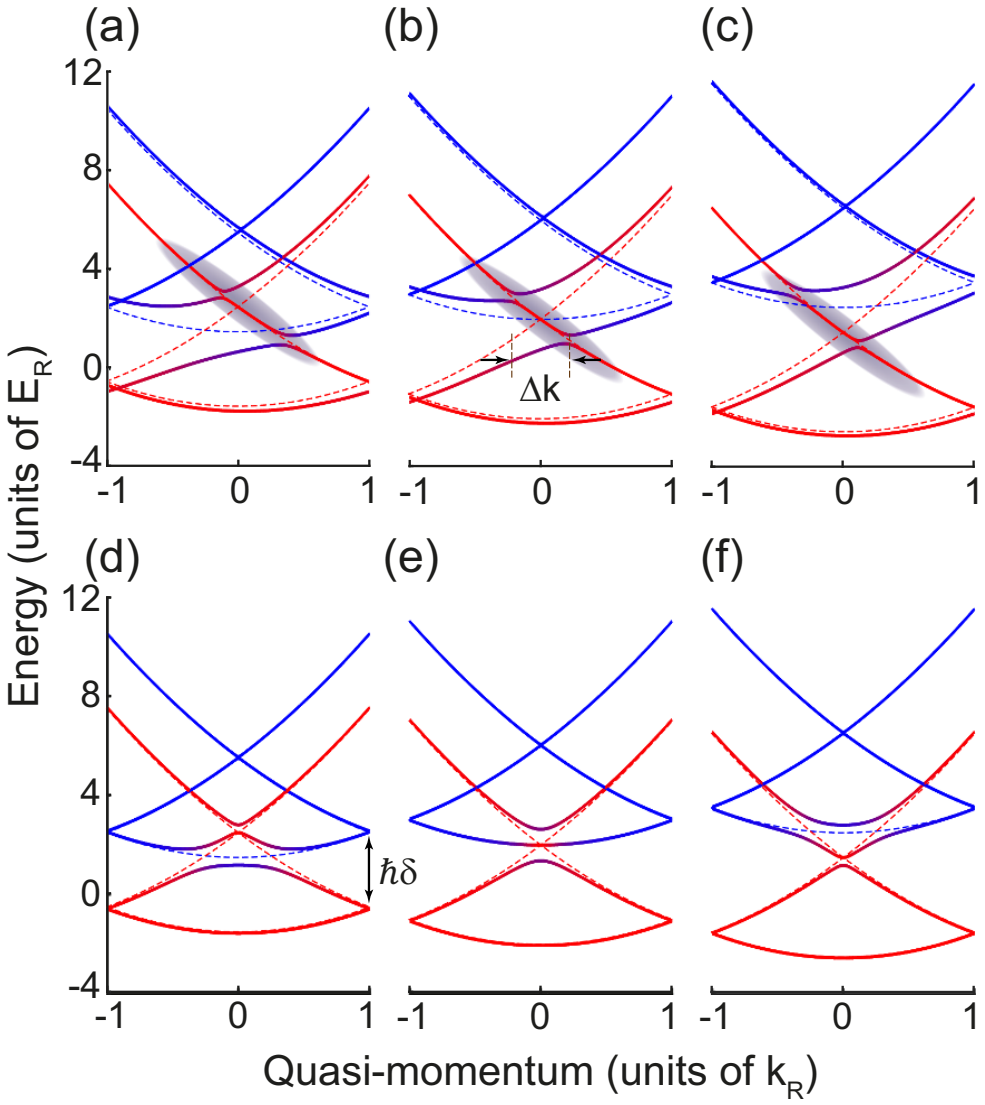

Figure 6.6: Energy band structures of a SO-coupled spin-1/2 atom under the Raman laser dressing: $\Omega_- = 5.3\ \Omega_+$ in (a–c) and $\Omega_- = \Omega_+$ in (d–e), and $\hbar\delta = 3E_R$ in (a, d), $4E_R$ in (b, e), and $5E_R$ in (c, f). The color of the solid lines indicates the bare spin fractions of the energy eigenstates: blue for spin-up and red for spin-down. The dashed lines represent the energy spectrum for $\Omega_\pm = 0$. The gray shadow areas in (a–c) indicate the region corresponding to the momentum states occupied by the sample in the experiment.

roles in the SOC physics of the system.

As an archetypal situation, we consider a spin-1/2 atom under the Raman dressing for $\delta\omega = 0$. Here, the counterpropagating Raman beams form a stationary polarization lattice with spatial periodicity of π/k_R. Including all the allowed Raman transitions, the effective Hamiltonian of the system is given by

$$\begin{aligned} H &= \begin{bmatrix} \frac{\hbar^2 k^2}{2m} + \frac{\hbar\delta}{2} & \frac{\hbar\Omega_+}{2} e^{i2k_R x} + \frac{\hbar\Omega_-}{2} e^{-i2k_R x} \\ \frac{\hbar\Omega_+}{2} e^{-i2k_R x} + \frac{\hbar\Omega_-}{2} e^{i2k_R x} & \frac{\hbar^2 k^2}{2m} - \frac{\hbar\delta}{2} \end{bmatrix} \\ &= \frac{\hbar^2 k^2}{2m} + \frac{\hbar\delta}{2}\sigma_z \\ &\quad + \frac{\hbar}{2}\Omega_x \cos(2k_R x)\sigma_x + \frac{\hbar}{2}\Omega_y \sin(2k_R x)\sigma_y, \end{aligned} \tag{6.5}$$

where $\hbar\delta$ is the sum of the differential Zeeman and ac Stark shifts, σ_i are the 2×2 Pauli matrices, and $\Omega_{x,y} = \Omega_+ \pm \Omega_-$. The final form of H shows that the Raman dressing is equivalent to an effective magnetic field

$$\mathcal{B} = (\delta,\ \Omega_x \cos(2k_R x),\ \Omega_y \sin(2k_R x)) \tag{6.6}$$

which has two parts: a bias field along the z axis and a spatially oscillating field on the x-y plane. Its chirality is determined by the sign of $\Omega_x\Omega_y = \Omega_+^2 - \Omega_-^2$. In the presence of the spatially oscillating magnetic field, the energy dispersion of the atom has a spinful band structure [Fig. 6.6].

Figure 6.6(b) displays a band structure for $\Omega_- = 5.3\ \Omega_+$ and $\delta = 4E_R/\hbar$, which straightforwardly explains the observed spectral splitting at the double resonance. In the experiment, $\delta\omega = 8E_R/\hbar$ and the polarization lattice of the Raman beams moves in the lab frame with velocity of $+2\hbar k_R/m\hat{x}$. Initially, the atoms in the trapped sample occupy the low quasi-momentum region of the second and third bands of the bare spin-down state, which is indicated by a gray region in Fig. 6.6(b), and they are projected to the eigenstates of

the spinful band structure via the Raman spectroscopy process. The quasi-momentum separation between the gap opening positions, which is marked with Δk in Fig. 6.6(b), is the spectral splitting observed in our Raman spectrum. We note that $\Delta k = 0$ in the symmetric case of $\Omega_- = \Omega_+$ [Fig. 6.6(e)] and the spectral splitting would not occur in the Raman spectrum.

6.5 Summary and outlook

We have measured the Raman spectra of a spin-polarized degenerate Fermi gas of ^{173}Yb atoms in the conventional SOC scheme and investigated the double resonance of Raman transitions. We observed the development of a spectral splitting at the double resonance of the $(r, \Delta m_F) = (1, 1)$ and $(2, 0)$ transitions and provided its quantiative explanation as the Autler–Townes doublet effect. Finally, we discussed our results in the context of the spinful energy band structure under the Raman laser dressing.

In general, when the system has multiple SOC paths in its spin-momentum space, a spinful energy band structure is formed because of the periodicity imposed by them. In previous experiments [23, 127], spinful band structures were designed and demonstrated by applying a RF field to the SO-coupled systems under the Raman laser dressing, where the role of the RF field was to open an additional coupling path between the two spin states. The results in this work highlight that the conventional Raman laser dressing scheme provides two ways of SOC and intrinsically generates a spinful band structure without the aid of an additional RF field. An interesting extention of this work is to investigate the magnetic ordering and properties of a Fermi gas in the spatially rotating magnetic field $\mathcal{B}$. In the $F = 5/2$ ^{173}Yb system, the chirality of $\mathcal{B}$ can be con-

trolled to some extent by the choice of the two spin states that are coupled by the Raman lasers. If the $m_F = \pm 1/2$ states are employed, $\Omega_y = 0$ and $\mathcal{B}$ changes from an axial field to a alternating transverse field as a function of $\hbar\delta$. In particular, when $\hbar\delta = 0$, $\mathcal{B} = 0$ points are periodically placed, which might profoundly affect the magnetic properties of the system. It was discussed in Ref. [23] to engineer a flat spinful band structure, which might be pursued via proper tuning of the parameters of our system.

Chapter 7

Periodic spin-orbit coupling of a Fermi gas

In this chapter, periodic spin-orbit (SO) coupling of a Fermi gas is discussed as an extended work of the outlook of Ch. 6. We generate spinful band structure with Raman lasers and succeeded to adiabatically load atoms on a single band. In this configuration, SO coupled point is periodically located in the quasi-momentum space. The occupation on the spinful bands are examined by the momentum distribution of atoms.

7.1 Introduction

As we pointed in Ch. 6, spin changing Raman process can impart momentum in both directions in case we use Raman lasers with π, $\perp$ π (or equivalently, a superposition of $\sigma^{\pm}$) polarizations: (1) absorbing σ^{-} photon and emitting π photon or (2) absorbing π photon and emitting σ^{+} photon resulting the same final spin state but opposite momentum change. For conventional SO coupling

experiments, only one of the two pathes is considered and used because the Zeeman shift between two spin states are far larger than the Fermi energy of the atoms. Large Zeeman splitting is desirable in some experiments to exclude other spin states by quadratic Zeeman shift. It might be experimentally difficult to maintain a small magnetic fields which gives Zeeman shifts between two ground states by the order of recoil energy ($\sim$kHz).

With alkaline-earth-like atoms, it is technically feasible to control Zeeman splitting of ground states in $\sim$kHz order owing to its small magnetic moment. Therefore it is possible to observe two resonant points inside the Fermi momentum and the atoms are coupled in two points in momentum states. As a result, atoms feel periodic potential by Raman transitions. Each coupling point corresponds to SO coupling and the system is periodically SO coupled in the momentum space. By controlling SO coupling parameters, one can engineer spinful band structure. Note that to make atoms with a certain momentum resonant to the two transitions simultaenously, can be interpreted as a double resonance as we discussed in Ch. 6.

7.2 Spinful band structure by Raman transitions

As we discussed in Sec. 6.4, band structure of atoms under Raman coupling shows spinful nature. Let us briefly explain how to display spinful band structure, including the cases of multiple spins. In case of three spins, the Hamiltonian

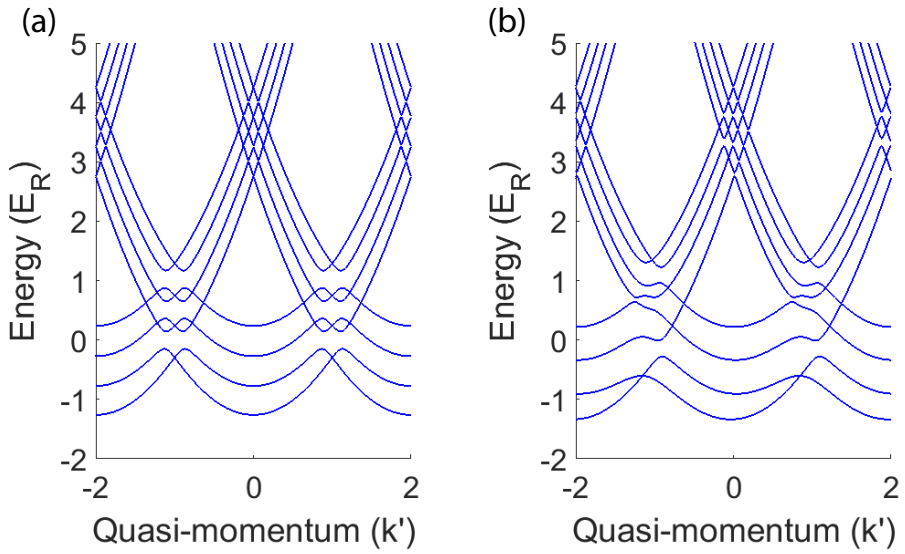

Figure 7.1: Energy diagram of spinful band structure in case of four spin components $m_F = -5/2, -3/2, -1/2$ and $1/2$. The band structures are drawn with a period of $4k'$ since it takes two Raman processes to return to the initial spin which impart $4k'$ momentum transfer. (a) All coupling strength of Raman transitions are $0.3E_R/\hbar$ and the Zeeman shift between adjacent spin components are $0.5E_R$. (b) The coupling strengths of Raman transitions are $(\Omega_{12}, \Omega_{21}) = (0.3, 0.6) \times E_R/\hbar$, $(\Omega_{23}, \Omega_{32}) = (0.3, 0.9) \times E_R/\hbar$, and $(\Omega_{34}, \Omega_{43}) = (0.3, 1.2) \times E_R/\hbar$ (see the text). The Zeeman shift between adjacent spin components are $0.5E_R$.

in Eq. 7.1 can be extended as

$$H = \begin{bmatrix} \frac{\hbar^2\mathbf{k}^2}{2m} + \hbar\delta_1 & \frac{\hbar\Omega_{12}}{2}e^{i\mathbf{k}'\cdot\mathbf{r}} + \frac{\hbar\Omega_{21}}{2}e^{-i\mathbf{k}'\cdot\mathbf{r}} & 0 \\ \frac{\hbar\Omega_{12}}{2}e^{-i\mathbf{k}'\cdot\mathbf{r}} + \frac{\hbar\Omega_{21}}{2}e^{i\mathbf{k}'\cdot\mathbf{r}} & \frac{\hbar^2\mathbf{k}^2}{2m} + \hbar\delta_2 & \frac{\hbar\Omega_{23}}{2}e^{i\mathbf{k}'\cdot\mathbf{r}} + \frac{\hbar\Omega_{32}}{2}e^{-i\mathbf{k}'\cdot\mathbf{r}} \\ 0 & \frac{\hbar\Omega_{23}}{2}e^{i\mathbf{k}'\cdot\mathbf{r}} + \frac{\hbar\Omega_{32}}{2}e^{-i\mathbf{k}'\cdot\mathbf{r}} & \frac{\hbar^2\mathbf{k}^2}{2m} + \hbar\delta_3 \end{bmatrix}$$

where δ_i represents the sum of the Zeeman shift and AC Stark shift of i-th spin. As the system is periodic in the momentum states along the direction of relative wave vector $\mathbf{k}' = \mathbf{k_2} - \mathbf{k_1}$ ($= 2k_R\hat{x}$, for counter propagating beams where k_R is recoil momentum of a Raman beam) of Raman transitions, we take basis for momenta and spins as $\cdots$, $|k - k', m_1\rangle$, $\cdots$, $|k - k', m_n\rangle$, $|k, m_1\rangle$, $\cdots$, $|k, m_n\rangle$, $|k + k', m_1\rangle$, $\cdots$, $|k + k', m_n\rangle$, $\cdots$. The kinetic energy and the Zeeman shifts are on the diagonal terms and Raman coupling terms are on off-diagonal terms. The off-diagonal terms are non-zero when initial state $|k_i, m_i\rangle$ and final state $|k_f, m_f\rangle$ satisfy $|k_i - k_f| = k'$ and $|m_i - m_f| = 1$. According to the direction of momentum transfer, off-diagonal parts are different so the Hamiltonian is not symmetric. By diagonalizing the Hamiltonian, one can obtain spinful band structure as shown in Fig. 7.1. Each band is composed of multiple bare spin states, especially near the coupling points at the band edge.

A two level case

Now, let us discuss a simple two level case where the transition strengths of the two Raman pathes are the same. The Raman lasers are counter propagating as it was in Ch. 6. The Hamiltonian of the system in Eq. 7.1 is simplified to

$$\begin{aligned} H &= \begin{bmatrix} \frac{\hbar^2k^2}{2m} + \frac{\hbar\delta}{2} & \hbar\Omega_+\cos(2k_Rx) \\ \hbar\Omega_+\cos(2k_Rx) & \frac{\hbar^2k^2}{2m} - \frac{\hbar\delta}{2} \end{bmatrix} \\ &= \frac{\hbar^2k^2}{2m} + \frac{\hbar\delta}{2}\sigma_z + \hbar\Omega_x\cos(2k_Rx)\sigma_x, \end{aligned} \tag{7.1}$$

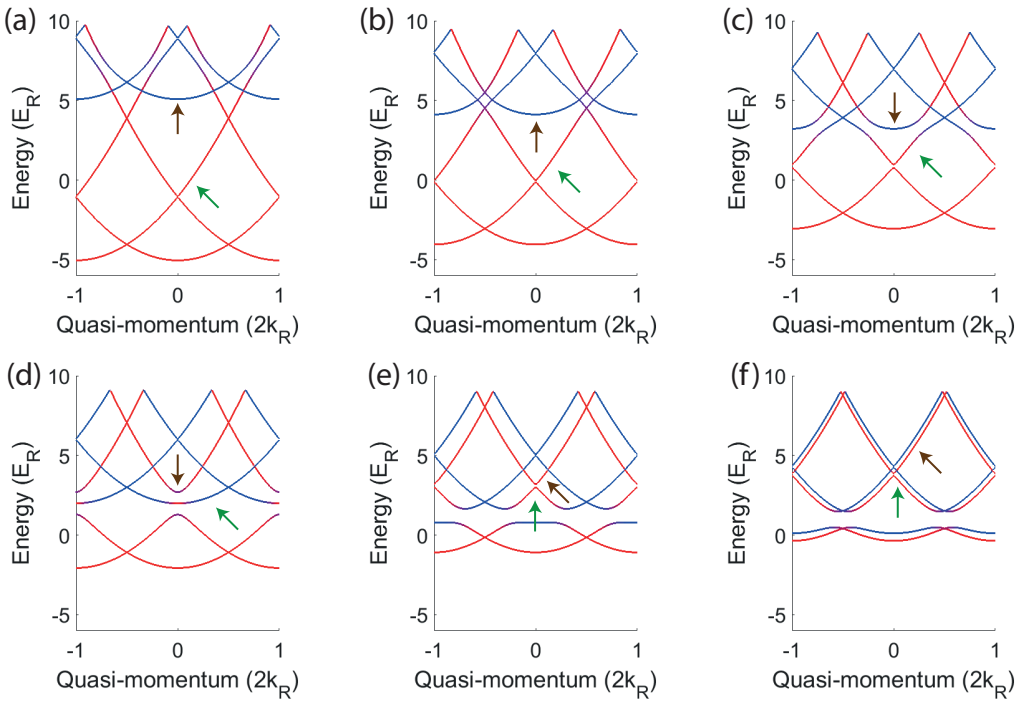

Figure 7.2: Spinful band structure of two level cases at $\Omega_+ = 1E_R/\hbar$, (a) $\delta = 10E_R/\hbar$, (b) $\delta = 8E_R/\hbar$, (c) $\delta = 6E_R/\hbar$, (d) $\delta = 4E_R/\hbar$, (e) $\delta = 2E_R/\hbar$, and (f) $\delta = 0.5E_R/\hbar$. The color of the curves represents the bare spin fraction of energy eigenstates: blue for spin-up and red for spin-down. The brown (green) arrows tracks same eigen states as the bias field is changed. The bare spin fraction of the band indicated by brown arrow is altered from blue to red.

where $\hbar\delta$ is the sum of the differential Zeeman shifts and AC Stark shifts, and σ_i are the 2×2 Pauli matrices. The effective magnetic field are aligned on the beam propagation axis and oscillates as it travels along the x-direction. With a high bias magnetic field $\delta \gg \Omega_x$, the z-component of effective magnetic field dominates and all atoms are aligned to z-axis. As one decrease the bias field, the spatially oscillating feature is recovered and the atoms follow an anti-ferromagnetic spin distribution.

Adiabatic loading on spinful band structure

A band structure of a two level, equal coupling strength case is shown in Fig. 7.2. The figure is equivalent to lower panel of Fig. 6.6 but shows for a wide range of magnetic fieds. As depicted in Fig 7.2 (a), bare spin fraction of the band indicated by brown arrow is almost blue at a high bias field like $\delta = 10E_R/\hbar$. If the Raman beam is applied after we increase the magnetic field to $\delta = 10E_R/\hbar$ with bare spin-up atoms only, all atoms are populated on a single dressed band. By decreasing the magnetic field slow enough for atoms to adiabatically follow the band, the momentum and spin of atoms are changed depending on a final value of bias field. The adiabaticity condition is determined by the energy gap between adjacent bands just as the Landau-Zener sweep.

Atoms can be also loaded on the band indicated by green arrows in Fig. 7.2. At $\delta = 4E_R/\hbar$, the bare spin fraction of most of the atoms are spin-up except around $k = 0$. As we turn up the power of Raman lasers slowly, we can load most atoms on the band indicated by green arrows. The band shows double minima feature at small Zeeman shift. So the shape fermi surface of the atoms will be changed according to the Zeeman shifts [24].

7.3 Experiments and Results

We prepare a polarized Fermi gas of ^{173}Yb atoms in $m_F = +1/2$ states with 2×10^5 atoms. A detailed preparation procedure is the same as what we described in previous chapters. We choose $m_F = 1/2$ states to make equal coupling strength for both Raman transitions where each imparts positive or negative momentum as it change the spin of atoms to $m_F = -1/2$ state. We use counter-propagating Raman beams along x-direction and bias magnetic field is applied along z-direction. The Raman lasers are -1 GHz detuned from $^3P_1$, $F' = -7/2$ resonance and the frequencies of the two lasers are the same. The polarizations of Raman beams are π and $\perp \pi$. The Fermi momentum of atoms are about $\sim 1k_R$.

We first adiabatically load atoms on the spinful band at large Zeeman splitting. At 200 G which corresponds to 11 E_R of Zeeman splitting between $m_F = \pm 1/2$ states, spin composition of dressed state is nearly the same as that of the bare $m_F = 1/2$ state. By linearely turning on the power of Raman beams to its final value of 80 μW per arm, atoms are loaded on the dressed band which is indicated by brown arrow in Fig 7.2 (a). The waist of the Raman beams is 150 μm. Then we ramp down the bias magnetic field with a rate of $dB/dt = -67$ G/ms. After reaching a target magnetic field, we abruptly turn off the Raman beams and the bias field hence the atoms are projected to the bare spin and momentum states.

Figure 7.3 shows resulting spectrum as a function of a final magnetic fields. Each data for a magnetic field represents integrated optical density along the direction perpendicular to the Raman beams. At high magnetic fields, the momentum distribution of the sample is not changed. As we decrease the bias

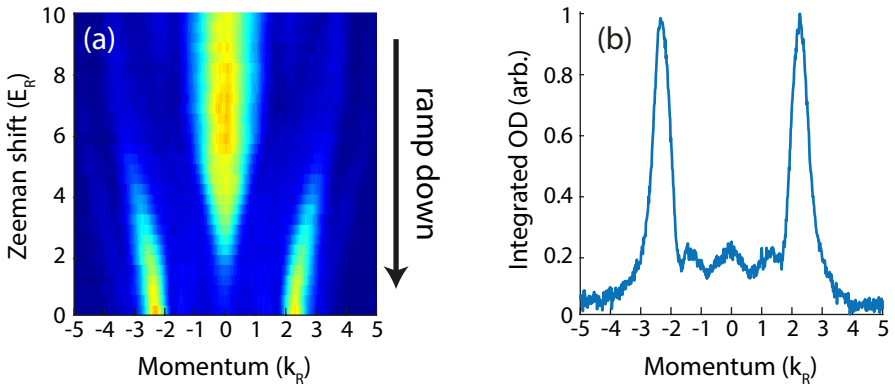

Figure 7.3: Spinful band structure of two level cases at $\Omega_+ = 1E_R/\hbar$, (a) $\delta = 10E_R/\hbar$, (b) $\delta = 8E_R/\hbar$, (c) $\delta = 6E_R/\hbar$, (d) $\delta = 4E_R/\hbar$, (e) $\delta = 2E_R/\hbar$, and (f) $\delta = 0.5E_R/\hbar$. The color of the curves represents the bare spin fraction of energy eigenstates: blue for spin-up and red for spin-down. The brown (green) arrows tracks same eigenstates as the bias field is changed. The bare spin fraction of the band indicated by brown arrow is altered from blue to red.

field, the higher momentum states start to be occupied at $|k| > |2k_R|$. At zero bias field, the momentum distribution is completely changed and all atoms have non-zero momenta only. The bare spin of the atoms at $B = 0$ is $m_F = -1/2$ states which is verified by optical blast sequence [55].

The result can be explained by Fig. 7.2. The blue and red spin on the Fig. 7.2 correspond to $m_F = \pm 1/2$, respectively. As long as the atoms are on the band on which we loaded initially, the final bare momentum state of the atoms would be $|k| > |2k_R|$ and the bare spin state become $m_F = -1/2$. The slopes of momentum distribution inside of each peak are sharper than the outer slope as shown in Fig. 7.3 because $|k| < |2k_R|$ is not allowed on the band which is not the case for $|k| > |2k_R|$.

Since the atoms are trapped in the optical dipole traps, the final momentum distribution is not an eigenstate. Therefore, within a timescale of few

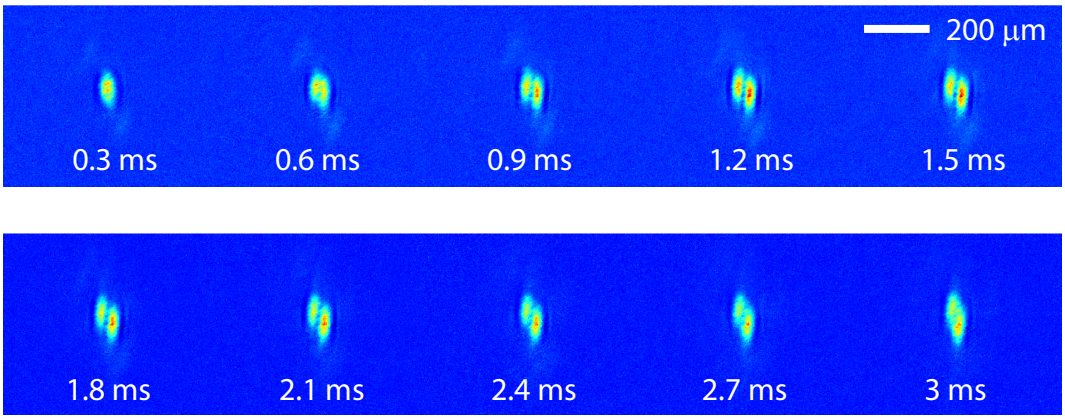

Figure 7.4: In situ images of atoms loaded on high momentum states $|k| > |2k_R|$. The bias magnetic field is turned off at $t = 0$ ms and the Raman lasers and the optical dipole traps are turned on during the measurements.

milliseconds determined by trapping frequency, the final momentum distribution is severely affected and dephased. We observed a swirling motion of atoms in the trap because the Raman beam axis is not a principal axis of the optical trap as shown in Fig. 7.4.

Note that if the ramp down rate of bias field is not slow enough, the atoms cannot follow the change of the initial band as shown in Fig. 7.5. Since there is a limitation on the field sweep rate experimentally, we control the power of Raman beams which vary the requirement on the field sweep rate. At low power case (Fig. 7.5 (a)) which require slower field sweep rate for the adiabatic process, we observe atoms with $|k| < 2k_R$ are populated. The position of the new peak corresponds to the energy minima position of the band indicated by green arrows in Fig. 7.2. We suspect that transition occurs though relatively small band gap between the brown band and the green band. Futher studies about the relaxation of single spin Fermi gas on the spinful band structure are needed and would be interesting.

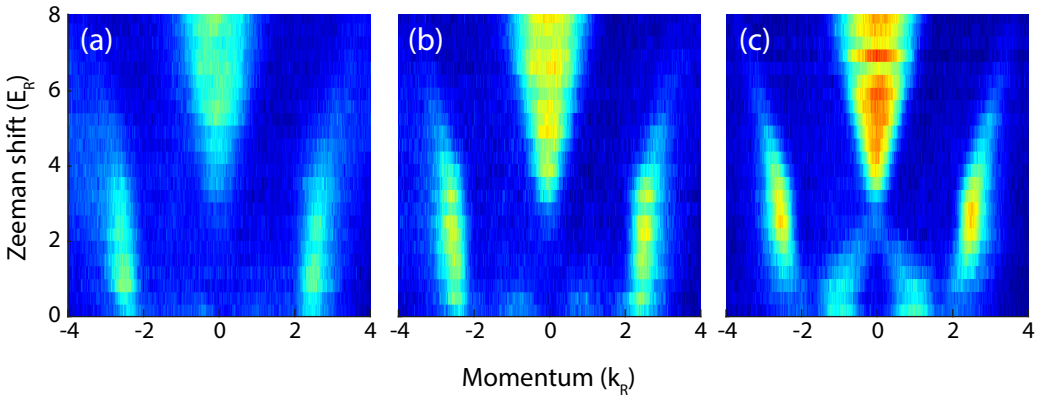

Figure 7.5: According to the power of Raman beams, diabatic transition between spinful band is observed. We ramp down a bias field with a constant rate $dB/dt = 14$ G/ms and powers of Raman beams are (a) $P = 108$ μW, (b) $P = 81$ μW, and (c) $P = 54$ μW.

We also loaded atoms on a band indicated by green arrows in Fig. 7.2. With $m_F = 1/2$ atoms at $\delta = 4E_R/\hbar$, the spin of the dressed band is remained almost $m_F = 1/2$ except near the $k = 0$. We slowly turn up the power of Raman beams and observed a majority of atoms are on a single dressed band as shown in Fig. 7.6 and minority of atoms are near $|k| = 2k_R$ which shows a loading on the adjacent bands. Starting from $\delta = 4E_R/\hbar$, we slowly ramp up and down the bias field with $dB/dt = \pm 25$ G/ms. As we ramp down the final bias field, population of $k_R < |k| < 2k_R$ is increased. This can be also explained by Fig. 7.2. From the center of the band, the momentum state of the band indicated by green arrows is contaminated by the $k_R < |k| < 2k_R$ states of $m_F = -1/2$, as we decrease the final bias field. For ramp up sequences, we can observe the outer region of the band near $|k| = k_R$ starts to decrease and the population of $|k| > 2k_R$ increases. This also consistent with the result expected from the calculated band structure in Fig. 7.2.

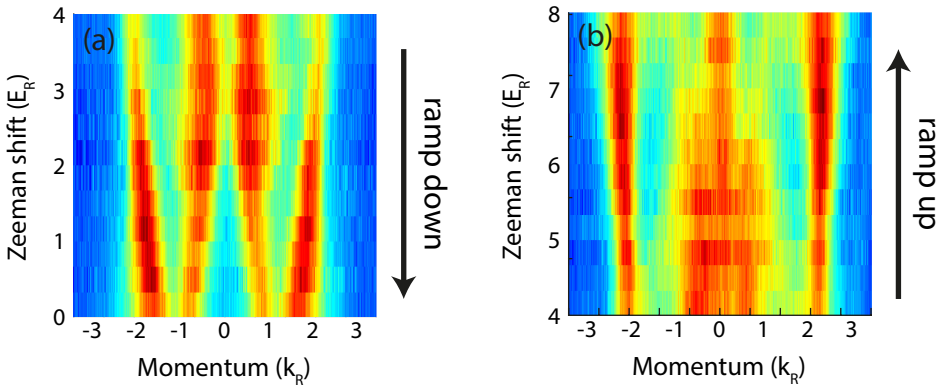

Figure 7.6: The spectrum of ramp down and up sequence from $\delta = 4E_R/\hbar$ at a rate of $dB/dt = \pm 25$ G/ms. The power of each Raman beam is 80 μW.

7.4 Summary and Outlook

To summarize, we discuss the spinful band structure and periodic SO coupled Hamiltonian by Raman lasers and a bias magnetic field. And experimentally, we observed the realization of spinful band structure and succeeded to load on spinful bands. After the atoms are loaded on a spinful band, we ramp up and down the bias magnetic field which induces a change of the bare momentum and bare spin compositions. Atoms occupying the trivial first band transferred to a third band accompanied by spin flip. In other words, with the aid of SO coupling, we succeeded to impart momentum to atoms and change momentum state of all atoms. The states where all atoms occupy higher band is equivalent to a negative temperature state which was demonstrated in [131].

This kind of dispersion engineering can be used to tune effective mass of the atoms and it might be possible to explore flat band dispersion. Heavy effective mass of fermions are desirable to study intriguing phenomena which are dominated by interactions [132]. Moreover, with an extention to two dimen-

sional cases, spin winding texture on bands allow to study nontrivial topology of bands [133] and topological insulators with ultracold atoms [23].

Chapter 8

Conclusion and outlooks

In this dissertation, we discussed basic concepts of degenerate Fermi gas and Raman transitions. The basic properties of Yb atoms are also covered which are related to achieving quantum degeneracy and to quantum gas experiments. Next, we introduced our experimental apparatus including a vacuum system, laser systems and an imaging system. With the apparatus described, degenerate quantum gases of Yb atoms are generated. About 10^5 atoms are succeeded to reach quantum degeneracy with $T/T_F < 0.1$. With the quantum degenerate atoms, nuclear spin detection and manipulation techniques are discussed and demonstrated.

With generated degenerate Fermi gases, we studied spin changing Raman transitions, or equivalently spin-orbit (SO) coupling. We observed two Raman transitions can be simultaneously resonant to atoms which we refer to a double resonance. One can find the meaning of the double resonance in an availability of making a periodic SO coupled Hamiltonian. With Raman lasers and a bias magnetic field, spinful band structure can be generated and we demonstrated adiabatic loading on a band. We also showed atoms follow an alteration of

spinful band as we sweep a bias field. Spinful flat band feature might be studied with this setup in the future.

An extension to two dimensional cases might open a new avenue of studies of SO coupling. The spin texture which we imprinted on a band structure in one dimension, can have nontrivial topological states when it is realied in two dimensions. Two dimensional extension of SO coupling studies are already realized so we expect our periodic SO coupling might provide a new way to generate nontrivial band topologies of a system. Moreover, variations of periodic SO coupling can be examined including a modulation on the frequency of Raman lasers or a coupling strength of Raman transitions which induce interband transition or change the strength of SO coupling as demonstrated in earlier works with a simple SO coupled atoms.

Aside from SO coupling physics, Yb can provide complementary features with alkali-metal atoms thanks to its different characteristics, such as an existence of narrow intercombination transitions, clock transitions and electron-spinless ground states. Especially, we expect that utilizing metastable states might widen the territory of Yb experiments, though it is not developed in our laboratory, yet. And, with a combination of nuclear spin states and excited states of a non-zero electronic spin offers various coupling pathways or multi-photon coupling schemes. As a promising example, a realization of nanostructure dark state optical lattices might be possible to realize with fermionic Yb in near future.

Bibliography

[1] M. H. Anderson, J. R. Ensher, M. R. Matthews, C. E. Wieman, and E. A. Cornell, "Observation of Bose-Einstein Condensation in a Dilute Atomic Vapor," *Science*, vol. 269, no. 5221, 1995.

[2] C. C. Bradley, C. A. Sackett, J. J. Tollett, and R. G. Hulet, "Evidence of Bose-Einstein Condensation in an Atomic Gas with Attractive Interactions," *Phys. Rev. Lett.*, vol. 75, no. 9, pp. 1687–1690, 1995.

[3] K. B. Davis, M. O. Mewes, M. R. Andrews, N. J. van Druten, D. S. Durfee, D. M. Kurn, and W. Ketterle, "Bose-Einstein Condensation in a Gas of Sodium Atoms," *Phys. Rev. Lett.*, vol. 75, no. 22, pp. 3969–3973, 1995.

[4] B. DeMarco and D. S. Jin, "Onset of Fermi Degeneracy in a Trapped Atomic Gas," *Science*, vol. 285, no. 5434, 1999.

[5] F. Schreck, L. Khaykovich, K. L. Corwin, G. Ferrari, T. Bourdel, J. Cubizolles, and C. Salomon, "Quasipure Bose-Einstein Condensate Immersed in a Fermi Sea," *Phys. Rev. Lett.*, vol. 87, no. 8, p. 080403, 2001.

[6] A. G. Truscott, K. E. Strecker, W. I. McAlexander, G. B. Partridge, and R. G. Hulet, "Observation of Fermi Pressure in a Gas of Trapped Atoms," *Science*, vol. 291, no. 5513, 2001.

[7] S. Giorgini, L. P. Pitaevskii, and S. Stringari, "Theory of ultracold atomic Fermi gases," *Rev. Mod. Phys.*, vol. 80, no. 4, pp. 1215–1274, 2008.

[8] I. Bloch, J. Dalibard, and W. Zwerger, "Many-body physics with ultracold gases," *Rev. Mod. Phys.*, vol. 80, no. 3, pp. 885–964, 2008.

[9] I. Bloch, "Ultracold quantum gases in optical lattices," *Nat. Phys.*, vol. 1, no. 1, pp. 23–30, 2005.

[10] K. M. O'Hara, S. L. Hemmer, M. E. Gehm, S. R. Granade, and J. E. Thomas, "Observation of a Strongly Interacting Degenerate Fermi Gas of Atoms," *Science*, vol. 298, no. 5601, 2002.

[11] C. Chin, R. Grimm, P. Julienne, and E. Tiesinga, "Feshbach resonances in ultracold gases," *Rev. Mod. Phys.*, vol. 82, no. 2, pp. 1225–1286, 2010.

[12] M. Greiner, O. Mandel, T. Esslinger, T. W. Hänsch, and I. Bloch, "Quantum phase transition from a superfluid to a Mott insulator in a gas of ultracold atoms," *Nature*, vol. 415, no. 6867, pp. 39–44, 2002.

[13] C. A. Regal, M. Greiner, and D. S. Jin, "Observation of Resonance Condensation of Fermionic Atom Pairs," *Phys. Rev. Lett.*, vol. 92, no. 4, p. 040403, 2004.

[14] M. Bartenstein, A. Altmeyer, S. Riedl, S. Jochim, C. Chin, J. H. Denschlag, and R. Grimm, "Crossover from a Molecular Bose-Einstein Condensate to a Degenerate Fermi Gas," *Phys. Rev. Lett.*, vol. 92, no. 12, p. 120401, 2004.

[15] M. W. Zwierlein, C. A. Stan, C. H. Schunck, S. M. F. Raupach, A. J. Kerman, and W. Ketterle, "Condensation of Pairs of Fermionic Atoms

near a Feshbach Resonance," *Phys. Rev. Lett.*, vol. 92, no. 12, p. 120403, 2004.

[16] J. Kinast, S. L. Hemmer, M. E. Gehm, A. Turlapov, and J. E. Thomas, "Evidence for Superfluidity in a Resonantly Interacting Fermi Gas," *Phys. Rev. Lett.*, vol. 92, no. 15, p. 150402, 2004.

[17] Q. Chen, J. Stajic, S. Tan, and K. Levin, "BCS–BEC crossover: From high temperature superconductors to ultracold superfluids," *Phys. Rep.*, vol. 412, no. 1, pp. 1–88, 2005.

[18] Y.-J. Lin, R. L. Compton, K. Jiménez-García, J. V. Porto, and I. B. Spielman, "Synthetic magnetic fields for ultracold neutral atoms," *Nature*, vol. 462, no. 7273, pp. 628–632, 2009.

[19] M. Aidelsburger, M. Atala, S. Nascimbène, S. Trotzky, Y.-A. Chen, and I. Bloch, "Experimental Realization of Strong Effective Magnetic Fields in an Optical Lattice," *Phys. Rev. Lett.*, vol. 107, no. 25, p. 255301, 2011.

[20] K. Jiménez-García, L. J. LeBlanc, R. A. Williams, M. C. Beeler, A. R. Perry, and I. B. Spielman, "Peierls Substitution in an Engineered Lattice Potential," *Phys. Rev. Lett.*, vol. 108, no. 22, p. 225303, 2012.

[21] J. Struck, C. Ölschläger, M. Weinberg, P. Hauke, J. Simonet, A. Eckardt, M. Lewenstein, K. Sengstock, and P. Windpassinger, "Tunable Gauge Potential for Neutral and Spinless Particles in Driven Optical Lattices," *Phys. Rev. Lett.*, vol. 108, no. 22, p. 225304, 2012.

[22] Y.-J. Lin, K. Jiménez-García, and I. B. Spielman, "Spin–orbit-coupled Bose–Einstein condensates," *Nature*, vol. 471, no. 7336, pp. 83–86, 2011.

[23] L. W. Cheuk, A. T. Sommer, Z. Hadzibabic, T. Yefsah, W. S. Bakr, and M. W. Zwierlein, "Spin-Injection Spectroscopy of a Spin-Orbit Coupled Fermi Gas," *Phys. Rev. Lett.*, vol. 109, no. 9, p. 095302, 2012.

[24] P. Wang, Z.-Q. Yu, Z. Fu, J. Miao, L. Huang, S. Chai, H. Zhai, and J. Zhang, "Spin-Orbit Coupled Degenerate Fermi Gases," *Phys. Rev. Lett.*, vol. 109, no. 9, p. 095301, 2012.

[25] M. A. Cazalilla, A. F. Ho, and M. Ueda, "Ultracold gases of ytterbium: Ferromagnetism and Mott states in an SU(6) Fermi system," *New J. Phys.*, vol. 11, 2009.

[26] M. A. Cazalilla and A. M. Rey, "Ultracold Fermi gases with emergent SU(N) symmetry," *Reps. Prog. Phys.*, vol. 77, no. 12, p. 124401, 2014.

[27] S. K. Yip, B. L. Huang, and J. S. Kao, "Theory of SU(N) Fermi liquids," *Phys. Rev. A - At. Mol. Opt. Phys.*, vol. 89, no. 4, 2014.

[28] A. Yamaguchi, *Metastable State of Ultracold and Quantum Degenerate Ytterbium Atoms: High-Resolution Spectroscopy and Cold Collisions*. PhD thesis, Kyoto University, 2008.

[29] A. V. Gorshkov, M. Hermele, V. Gurarie, C. Xu, P. S. Julienne, J. Ye, P. Zoller, E. Demler, M. D. Lukin, and A. M. Rey, "Two-orbital SU(N) magnetism with ultracold alkaline-earth atoms," *Nat. Phys.*, vol. 6, no. 4, pp. 289–295, 2010.

[30] T. Esslinger, "Fermi-Hubbard Physics with Atoms in an Optical Lattice," *Annu. Rev. Condens. Matter Phys.*, vol. 1, no. 1, pp. 129–152, 2010.

[31] A. O. Jamison, B. Plotkin-Swing, and S. Gupta, "Advances in precision contrast interferometry with Yb Bose-Einstein condensates," *Phys. Rev. A*, vol. 90, no. 6, p. 063606, 2014.

[32] Y. Takasu, K. Maki, K. Komori, T. Takano, K. Honda, M. Kumakura, T. Yabuzaki, and Y. Takahashi, "Spin-Singlet Bose-Einstein Condensation of Two-Electron Atoms," *Phys. Rev. Lett.*, vol. 91, no. 4, p. 040404, 2003.

[33] T. Fukuhara, Y. Takasu, M. Kumakura, and Y. Takahashi, "Degenerate Fermi gases of ytterbium.," *Phys. Rev. Lett.*, vol. 98, no. 3, p. 030401, 2007.

[34] K. Honda, Y. Takasu, T. Kuwamoto, M. Kumakura, Y. Takahashi, and T. Yabuzaki, "Optical dipole force trapping of a fermion-boson mixture of ytterbium isotopes," *Phys. Rev. A*, vol. 66, no. 2, p. 021401, 2002.

[35] S. Taie, Y. Takasu, S. Sugawa, R. Yamazaki, T. Tsujimoto, R. Murakami, and Y. Takahashi, "Realization of a SU(2)xSU(6) system of fermions in a cold atomic gas," *Phys. Rev. Lett.*, vol. 105, no. 19, p. 190401, 2010.

[36] T. Fukuhara, Y. Takasu, S. Sugawa, and Y. Takahashi, "Quantum Degenerate Fermi Gases of Ytterbium Atoms," *J. Low Temp. Phys.*, vol. 148, no. 3-4, pp. 441–445, 2007.

[37] H. Zhai, "Degenerate quantum gases with spin–orbit coupling: a review," *Reps. Prog. Phys.*, vol. 78, no. 2, p. 026001, 2015.

[38] M. Lee, J. H. Han, J. H. Kang, M.-S. Kim, and Y. Shin, "Double resonance of Raman transitions in a degenerate Fermi gas," *Phys. Rev. A*, vol. 95, no. 4, p. 043627, 2017.

[39] Y. Takasu, K. Komori, K. Honda, M. Kumakura, T. Yabuzaki, and Y. Takahashi, "Photoassociation Spectroscopy of Laser-Cooled Ytterbium Atoms," *Phys. Rev. Lett.*, vol. 93, no. 12, p. 123202, 2004.

[40] T. Takano, M. Fuyama, R. Namiki, and Y. Takahashi, "Spin Squeezing of a Cold Atomic Ensemble with the Nuclear Spin of One-Half," *Phys. Rev. Lett.*, vol. 102, no. 3, p. 033601, 2009.

[41] V. V. Ivanov, A. Khramov, A. H. Hansen, W. H. Dowd, F. Münchow, A. O. Jamison, and S. Gupta, "Sympathetic Cooling in an Optically Trapped Mixture of Alkali and Spin-Singlet Atoms," *Phys. Rev. Lett.*, vol. 106, no. 15, p. 153201, 2011.

[42] A. H. Hansen, A. Khramov, W. H. Dowd, A. O. Jamison, V. V. Ivanov, and S. Gupta, "Quantum degenerate mixture of ytterbium and lithium atoms," *Phys. Rev. A*, vol. 84, no. 1, p. 011606, 2011.

[43] A. H. Hansen, A. Y. Khramov, W. H. Dowd, A. O. Jamison, B. Plotkin-Swing, R. J. Roy, and S. Gupta, "Production of quantum-degenerate mixtures of ytterbium and lithium with controllable interspecies overlap," *Phys. Rev. A*, vol. 87, no. 1, p. 013615, 2013.

[44] A. Khramov, *Experiments in the Ultracold Lithium - Ytterbium System.* PhD thesis, University of Washington, 2013.

[45] A. H. Hansen, *Interacting Quantm Gases of Lithium and Ytterbium.* PhD thesis, University of Washington, 2013.

[46] W. H. Dowd, *Interactions in the Ultracold Lithium - Ytterbium 3P2 System.* PhD thesis, University of Washington, 2014.

[47] A. O. Jamison, *Precision Interferometry with Bose-Einstein Condensates*. PhD thesis, University of Washington, 2014.

[48] V. D. Vaidya, J. Tiamsuphat, S. L. Rolston, and J. V. Porto, "Degenerate Bose-Fermi mixtures of rubidium and ytterbium," *Phys. Rev. A*, vol. 92, no. 4, p. 043604, 2015.

[49] S. Dörscher, A. Thobe, B. Hundt, A. Kochanke, R. Le Targat, P. Windpassinger, C. Becker, and K. Sengstock, "Creation of quantum-degenerate gases of ytterbium in a compact 2D-/3D-magneto-optical trap setup," *Rev. Sci. Instrum.*, vol. 84, no. 4, p. 043109, 2013.

[50] S. Dörscher, *Creation of ytterbium quantum gases with a compact 2D-/3D-MOT setup*. PhD thesis, University of Hamburg, 2013.

[51] A. Thobe, *Ultracold Yb gases with control over spin and orbital degrees of freedom*. PhD thesis, University of Hamburg, 2014.

[52] F. Scazza, C. Hofrichter, M. Höfer, P. C. De Groot, I. Bloch, and S. Fölling, "Observation of two-orbital spin-exchange interactions with ultracold SU(N)- symmetric fermions," *Nat. Phys.*, vol. 10, no. 10, pp. 779–784, 2014.

[53] G. Cappellini, M. Mancini, G. Pagano, P. Lombardi, L. Livi, M. Siciliani de Cumis, P. Cancio, M. Pizzocaro, D. Calonico, F. Levi, C. Sias, J. Catani, M. Inguscio, and L. Fallani, "Direct Observation of Coherent Interorbital Spin-Exchange Dynamics," *Phys. Rev. Lett.*, vol. 113, no. 12, p. 120402, 2014.

[54] G. Pagano, M. Mancini, G. Cappellini, P. Lombardi, F. Schäfer, H. Hu, X.-j. Liu, J. Catani, C. Sias, M. Inguscio, and L. Fallani, "A one-dimensional liquid of fermions with tunable spin," *Nat. Phys.*, vol. 10, no. 3, pp. 198–201, 2014.

[55] M. Mancini, G. Pagano, G. Cappellini, L. Livi, M. Rider, J. Catani, C. Sias, P. Zoller, M. Inguscio, M. Dalmonte, and L. Fallani, "Observation of chiral edge states with neutral fermions in synthetic Hall ribbons," *Science*, vol. 349, no. 6255, pp. 1510–1513, 2015.

[56] C. Hofrichter, L. Riegger, F. Scazza, M. Höfer, D. R. Fernandes, I. Bloch, and S. Fölling, "Direct Probing of the Mott Crossover in the SU (N) Fermi-Hubbard Model," *Phys. Rev. X*, vol. 6, no. 2, p. 021030, 2016.

[57] L. F. Livi, G. Cappellini, M. Diem, L. Franchi, C. Clivati, M. Frittelli, F. Levi, D. Calonico, J. Catani, M. Inguscio, and L. Fallani, "Synthetic Dimensions and Spin-Orbit Coupling with an Optical Clock Transition," *Phys. Rev. Lett.*, vol. 117, no. 22, p. 220401, 2016.

[58] B. Song, C. He, S. Zhang, E. Hajiyev, W. Huang, X.-J. Liu, and G.-B. Jo, "Spin-orbit-coupled two-electron Fermi gases of ytterbium atoms," *Phys. Rev. A*, vol. 94, no. 6, p. 061604, 2016.

[59] F. Wilczek, "Quantum Mechanics of Fractional-Spin Particles," *Phys. Rev. Lett.*, vol. 49, no. 14, pp. 957–959, 1982.

[60] M. V. N. Murthy, J. Law, M. Brack, and R. K. Bhaduri, "Quantum spectrum of three anyons in an oscillator potential," *Phys. Rev. Lett.*, vol. 67, no. 14, pp. 1817–1820, 1991.

[61] R. Pathria, *Statistical Mechanics*. Elsevier, 1996.

[62] D. A. Butts and D. S. Rokhsar, "Trapped Fermi gases," *Phys. Rev. A*, vol. 55, no. 6, pp. 4346–4350, 1997.

[63] B. DeMarco, *Quantum Behavior of an Atomic Fermi Gas*. PhD thesis, University of Colorado, 2001.

[64] D. A. Steck, *Quantum and Atom Optics*. 2007.

[65] C. R. Hammond, *The Elements, in Handbook of Chemistry and Physics 81st edition*. CRC press, 2000.

[66] "Ytterbium MSDS."

[67] C. J. Foot, *Atomic Physics*. 2005.

[68] S. G. Porsev, Y. G. Rakhlina, and M. G. Kozlov, "Electric-dipole amplitudes, lifetimes, and polarizabilities of the low-lying levels of atomic ytterbium," *Phys. Rev. A*, vol. 60, no. 4, pp. 2781–2785, 1999.

[69] F. Scazza, *Probing SU(N)-symmetric orbital interactions with ytterbium Fermi gases in optical lattices*. Ph. d. thesis, Ludwig-Maximilians-Universität München, 2015.

[70] W. F. Meggers and J. L. Tech, "The first spectrum of ytterbium (Yb I)," *J. Res. Natl. Bur. Stand. (1934).*, vol. 83, 1978.

[71] S. Sugawa, R. Yamazaki, S. Taie, and Y. Takahashi, "Bose-Einstein condensate in gases of rare atomic species," *Phys. Rev. A*, vol. 84, no. 1, p. 011610, 2011.

[72] T. Fukuhara, S. Sugawa, Y. Takasu, and Y. Takahashi, "All-optical formation of quantum degenerate mixtures," *Phys. Rev. A*, vol. 79, no. 2, p. 021601, 2009.

[73] S. Sugawa, K. Inaba, S. Taie, R. Yamazaki, M. Yamashita, and Y. Takahashi, "Interaction and filling induced quantum phases of dual Mott insulators of bosons and fermions," *Nat. Phys.*, vol. 7, no. 8, pp. 642–648, 2011.

[74] J. Emsley, *The Elements, Oxford Chemistry Guides*. Oxford University Press, 1995.

[75] M. Kitagawa, K. Enomoto, K. Kasa, Y. Takahashi, R. Ciuryło, P. Naidon, and P. S. Julienne, "Two-color photoassociation spectroscopy of ytterbium atoms and the precise determinations of s -wave scattering lengths," *Phys. Rev. A*, vol. 77, no. 1, p. 012719, 2008.

[76] M. W. Zwierlein, J. R. Abo-Shaeer, A. Schirotzek, C. H. Schunck, and W. Ketterle, "Vortices and superfluidity in a strongly interacting Fermi gas," *Nature*, vol. 435, no. 7045, pp. 1047–1051, 2005.

[77] C. A. Regal, M. Greiner, and D. S. Jin, "Observation of Resonance Condensation of Fermionic Atom Pairs," *Phys. Rev. Lett.*, vol. 92, no. 4, p. 040403, 2004.

[78] P. O. Fedichev, Y. Kagan, G. V. Shlyapnikov, and J. T. M. Walraven, "Influence of Nearly Resonant Light on the Scattering Length in Low-Temperature Atomic Gases," *Phys. Rev. Lett.*, vol. 77, no. 14, pp. 2913–2916, 1996.

[79] K. M. Jones, E. Tiesinga, P. D. Lett, and P. S. Julienne, "Ultracold photoassociation spectroscopy: Long-range molecules and atomic scattering," *Rev. Mod. Phys.*, vol. 78, no. 2, pp. 483–535, 2006.

[80] K. Enomoto, K. Kasa, M. Kitagawa, and Y. Takahashi, "Optical Feshbach Resonance Using the Intercombination Transition," *Phys. Rev. Lett.*, vol. 101, no. 20, p. 203201, 2008.

[81] M.-S. Kim, J. Lee, J. H. Lee, Y. Shin, and J. Mun, "Measurements of optical Feshbach resonances of ˆ{174}Yb atoms," *Phys. Rev. A*, vol. 94, no. 4, p. 042703, 2016.

[82] M. Höfer, L. Riegger, F. Scazza, C. Hofrichter, D. R. Fernandes, M. M. Parish, J. Levinsen, I. Bloch, and S. Fölling, "Observation of an Orbital Interaction-Induced Feshbach Resonance in 173Yb," *Phys. Rev. Lett.*, vol. 115, no. 26, p. 265302, 2015.

[83] G. Pagano, M. Mancini, G. Cappellini, L. Livi, C. Sias, J. Catani, M. Inguscio, and L. Fallani, "Strongly Interacting Gas of Two-Electron Fermions at an Orbital Feshbach Resonance.," *Phys. Rev. Lett.*, vol. 115, no. 26, p. 265301, 2015.

[84] K. I. Kugel and D. I. Khomskii, "Crystal structure and magnetic properties of substances with orbital degeneracy," *Sov. Phys. JETP*, vol. 64, pp. 1429–1439, 1973.

[85] Y. Tokura and N. Nagaosa, "Orbital Physics in Transition-Metal Oxides," *Science*, vol. 288, no. 5465, 2000.

[86] M. A. Ruderman and C. Kittel, "Indirect Exchange Coupling of Nuclear Magnetic Moments by Conduction Electrons," *Phys. Rev.*, vol. 96, no. 1, pp. 99–102, 1954.

[87] S. Doniach, "The Kondo lattice and weak antiferromagnetism," *Phys. B+C*, vol. 91, pp. 231–234, 1977.

[88] A. C. Hewson, *The Kondo Problem to Heavy Fermions*. Cambridge University Press, 1993.

[89] H. Tsunetsugu, M. Sigrist, and K. Ueda, "The ground-state phase diagram of the one-dimensional Kondo lattice model," *Rev. Mod. Phys.*, vol. 69, no. 3, pp. 809–864, 1997.

[90] J. B. Marston and I. Affleck, "Large-n limit of the Hubbard-Heisenberg model," *Phys. Rev. B*, vol. 39, no. 16, pp. 11538–11558, 1989.

[91] N. Read and S. Sachdev, "Spin-Peierls, valence-bond solid, and Néel ground states of low-dimensional quantum antiferromagnets," *Phys. Rev. B*, vol. 42, no. 7, pp. 4568–4589, 1990.

[92] K. Harada, N. Kawashima, and M. Troyer, "Néel and Spin-Peierls Ground States of Two-Dimensional SU(N) Quantum Antiferromagnets," *Phys. Rev. Lett.*, vol. 90, no. 11, p. 117203, 2003.

[93] M. Hermele, V. Gurarie, and A. M. Rey, "Mott insulators of ultracold fermionic alkaline earth atoms: Underconstrained magnetism and chiral spin liquid," *Phys. Rev. Lett.*, vol. 103, no. 13, p. 135301, 2009.

[94] X. Zhang, M. Bishof, S. L. Bromley, C. V. Kraus, M. S. Safronova, P. Zoller, A. M. Rey, and J. Ye, "Spectroscopic observation of SU(N)-

symmetric interactions in Sr orbital magnetism," *Science*, vol. 345, no. 6203, 2014.

[95] A. O. Jamison, *Precision Interferometry with Bose-Einstein Condensates*. PhD thesis, University of Washington, 2014.

[96] R. Grimm, M. Weidemüller, and Y. B. Ovchinnikov, "Optical Dipole Traps for Neutral Atoms," *Adv. At. Mol. Opt. Phys.*, vol. 42, no. C, pp. 95–170, 2000.

[97] H. J. Metcalf and P. van der Straten, *Laser Cooling and Trapping*. Graduate Texts in Contemporary Physics, Springer, 1999.

[98] M. Pizzocaro, D. Calonico, P. C. Pastor, J. Catani, G. A. Costanzo, F. Levi, and L. Lorini, "Efficient frequency doubling at 399 nm," *Appl. Opt.*, vol. 53, no. 16, p. 3388, 2014.

[99] M.-S. Kim, *Generation of degenerate quantum gases of ytterbium atoms*. PhD thesis, Seoul National University, 2016.

[100] B. E. A. Saleh and M. C. Teich, "Fundamentals of Photonics, 2nd Edition," 2007.

[101] G. D. Boyd and D. A. Kleinman, "Parametric Interaction of Focused Gaussian Light Beams," *J. Appl. Phys.*, vol. 39, no. 8, pp. 3597–3639, 1968.

[102] D. J. McCarron, S. A. King, and S. L. Cornish, "Modulation transfer spectroscopy in atomic rubidium," *Meas. Sci. Technol.*, vol. 19, no. 10, p. 105601, 2008.

[103] W. Setiawan, *Fermi Gas Microscope*. PhD thesis, Harvard University, 2012.

[104] M. Scholl, *Probing an ytterbium Bose-Einstein condensate using an ultranarrow optical line : Towards artificial gauge fields in optical lattices*. PhD thesis, Ecole Normale Superieure College de France, 2014.

[105] M.-S. Kim, M. Lee, J. H. Han, and Y.-i. Shin, "Experimental apparatus for generating quantum degenerate gases of ytterbium atoms," *J. Korean Phys. Soc.*, vol. 67, no. 10, pp. 1719–1725, 2015.

[106] S. J. Krinner, *Towards Quantum Degenerate Gases of Ytterbium Atoms*. PhD thesis, École Normale Supérieure, 2010.

[107] M. Reina, *Optical trapping of ytterbium atoms*. PhD thesis, University of Washington, 2003.

[108] J. W. Cho, H.-g. Lee, S. Lee, J. Ahn, W.-K. Lee, D.-H. Yu, S. K. Lee, and C. Y. Park, "Optical repumping of triplet- P states enhances magneto-optical trapping of ytterbium atoms," *Phys. Rev. A*, vol. 85, no. 3, p. 035401, 2012.

[109] T. Kuwamoto, K. Honda, Y. Takahashi, and T. Yabuzaki, "Magneto-optical trapping of Yb atoms using an intercombination transition," *Phys. Rev. A*, vol. 60, no. 2, pp. R745–R748, 1999.

[110] J. Lee, J. H. Lee, J. Noh, and J. Mun, "Core-shell magneto-optical trap for alkaline-earth-metal-like atoms," *Phys. Rev. A*, vol. 91, no. 5, p. 053405, 2015.

[111] S. Stellmer, *Degenerate quantum gases of strontium dissertation.* PhD thesis, University of Innsbruck, 2013.

[112] M. Scholl, *Probing an ytterbium Bose-Einstein condensate using an ultra-narrow optical line: Towards artificial gauge fields in optical lattices.* PhD thesis, Ecole Normale Superieure, 2014.

[113] P. O. Fedichev, M. W. Reynolds, and G. V. Shlyapnikov, "Three-Body Recombination of Ultracold Atoms to a Weakly Bound s Level," *Phys. Rev. Lett.*, vol. 77, no. 14, pp. 2921–2924, 1996.

[114] J. Weiner, V. S. Bagnato, S. Zilio, and P. S. Julienne, "Experiments and theory in cold and ultracold collisions," *Rev. Mod. Phys.*, vol. 71, no. 1, pp. 1–85, 1999.

[115] R. Yamamoto, J. Kobayashi, T. Kuno, K. Kato, and Y. Takahashi, "An ytterbium quantum gas microscope with narrow-line laser cooling," *New J. Phys.*, vol. 18, no. 2, p. 023016, 2016.

[116] M. Miranda, R. Inoue, Y. Okuyama, A. Nakamoto, and M. Kozuma, "Site-resolved imaging of ytterbium atoms in a two-dimensional optical lattice," *Phys. Rev. A*, vol. 91, no. 6, p. 063414, 2015.

[117] Y. K. Kato, R. C. Myers, A. C. Gossard, and D. D. Awschalom, "Observation of the Spin Hall Effect in Semiconductors," *Science*, vol. 306, no. 5703, 2004.

[118] M. König, S. Wiedmann, C. Brüne, A. Roth, H. Buhmann, L. W. Molenkamp, X.-L. Qi, and S.-C. Zhang, "Quantum Spin Hall Insulator State in HgTe Quantum Wells," *Science*, vol. 318, no. 5851, 2007.

[119] M. Z. Hasan and C. L. Kane, "Colloquium: Topological insulators," *Rev. Mod. Phys.*, vol. 82, no. 4, pp. 3045–3067, 2010.

[120] N. Goldman, G. Juzelinas, P. Öhberg, and I. B. Spielman, "Light-induced gauge fields for ultracold atoms," *Reps. Prog. Phys.*, vol. 77, no. 12, p. 126401, 2014.

[121] N. Q. Burdick, Y. Tang, and B. L. Lev, "Long-Lived Spin-Orbit-Coupled Degenerate Dipolar Fermi Gas," *Phys. Rev. X*, vol. 6, no. 3, p. 031022, 2016.

[122] L. Huang, Z. Meng, P. Wang, P. Peng, S.-L. Zhang, L. Chen, D. Li, Q. Zhou, and J. Zhang, "Experimental realization of two-dimensional synthetic spin–orbit coupling in ultracold Fermi gases," *Nat. Phys.*, vol. 12, no. 6, pp. 540–544, 2016.

[123] Y. Cao, S.-H. Zou, X.-J. Liu, S. Yi, G.-L. Long, and H. Hu, "Gapless Topological Fulde-Ferrell Superfluidity in Spin-Orbit Coupled Fermi Gases," *Phys. Rev. Lett.*, vol. 113, no. 11, p. 115302, 2014.

[124] Y. Xu, L. Mao, B. Wu, and C. Zhang, "Dark Solitons with Majorana Fermions in Spin-Orbit-Coupled Fermi Gases," *Phys. Rev. Lett.*, vol. 113, no. 13, p. 130404, 2014.

[125] R. Zhang, Y. Cheng, H. Zhai, and P. Zhang, "Orbital Feshbach Resonance in Alkali-Earth Atoms.," *Phys. Rev. Lett.*, vol. 115, no. 13, p. 135301, 2015.

[126] S. H. Autler and C. H. Townes, "Stark Effect in Rapidly Varying Fields," *Phys. Rev.*, vol. 100, no. 2, pp. 703–722, 1955.

[127] K. Jiménez-García, L. J. LeBlanc, R. A. Williams, M. C. Beeler, A. R. Perry, and I. B. Spielman, "Peierls substitution in an engineered lattice potential," *Phys. Rev. Lett.*, vol. 108, no. 22, p. 225303, 2012.

[128] S. Stellmer, R. Grimm, and F. Schreck, "Detection and manipulation of nuclear spin states in fermionic strontium," *Phys. Rev. A*, vol. 84, no. 4, p. 043611, 2011.

[129] M. Mancini, *Quantum Simulation with Ytterbium Atoms in Synthetic Dimensions*. PhD thesis, University of Florence, 2015.

[130] G. Veeravalli, E. Kuhnle, P. Dyke, and C. J. Vale, "Bragg Spectroscopy of a Strongly Interacting Fermi Gas," *Phys. Rev. Lett.*, vol. 101, no. 25, p. 250403, 2008.

[131] S. Braun, J. P. Ronzheimer, M. Schreiber, S. S. Hodgman, T. Rom, I. Bloch, and U. Schneider, "Negative Absolute Temperature for Motional Degrees of Freedom," *Science*, vol. 339, no. 6115, 2013.

[132] P. Gegenwart, Q. Si, and F. Steglich, "Quantum criticality in heavy-fermion metals," *Nat. Phys.*, vol. 4, no. 3, pp. 186–197, 2008.

[133] J. D. Sau, R. Sensarma, S. Powell, I. B. Spielman, and S. Das Sarma, "Chiral Rashba spin textures in ultracold Fermi gases," *Phys. Rev. B*, vol. 83, no. 14, p. 140510, 2011.

초 록

라만 전이란, 두 개의 광자를 동시에 먹고 내보내는 과정을 통해서 물질의 상태를 바꿀 수 있는 방법으로써, 물리학 뿐만 아니라 생물학, 화학, 공학 등에서 아주 광범위하게 쓰이고 있는 기술이다. 특히 물리학에 있어서는 시스템의 양자역학적 상태를 조절하는 데 쓰이는 핵심적인 기술 중 하나이다.

라만 전이가 연결하는 두 개의 상태가 서로 다른 스핀으로 기술될 수 있으면서, 동시에 운동량을 주고받아야만 전이가 일어날 경우, 스핀과 운동량은 서로 별개의 물리량이 아니게 된다. 이와 같이 스핀과 운동량이 서로 얽혀있게 되면, 원자의 분산 관계가 일반적인 경우와 큰 차이를 보이게 된다. 이러한 현상은 스핀-궤도 결합이라고 불리우며, 원자 물리에서의 미세 구조의 기본 원리이기도 하면서 위상학적 부도체의 기본 원리이기도 하므로 많은 연구들이 진행되어 왔다. 특히 극저온 원자 기체들을 이용한 양자 시뮬레이터의 관점에서 스핀-궤도 결합은 많은 연구들이 진행되어 왔으며, 알칼리 원자의 보즈 아인슈타인 응집체에서 뿐만 아니라 알칼리 원자의 겹친 페르미 기체에서도 구현된 바 있다. 최근에 들어서는 알칼리 금속 외에도 Dy 같은 란탄족 페르미온도 스핀-궤도 결합이 구현되었으며, Yb 나 Sr 같은 알칼리 토금속류 원자들의 상대적으로 강한 스핀-궤도 결합 세기, 준안정 상태의 존재, 전자 스핀이 없는 바닥상태의 특징 등을 이용하여 스핀-궤도 결합과 관련된 연구가 활발히 진행되고 있다.

본 연구에서는 첫째로 위와 같은 스핀-궤도 결합 연구를 하기 위한 Yb 원자의 양자 기체 생성 장치 개발의 자세한 과정과 그 일련의 원리을 다룬다. 제작한 양자 기체 생성 장치로 보즈 아인슈타인 응집체를 생성하였으며, 10^5개 정도의 원자들을 $T/T_F < 0.1$ 정도의 온도를 갖는 ^{173}Yb 원자들의 겹친 페르미 기체를 생성하는 것에도 성공하였다. 생성된 겹친 페르미 기체상태의 원자들을 이용하여 이터븀 원자의 바닥 상태의 핵 스핀들을 모두 분리하여 관측하는 광학

적 슈테른-겔라흐 분리법을 논하고, 스핀 상태의 상대적인 비율을 바꿀 수 있는 광 펌핑 기술을 함께 소개한다.

본 연구의 두 번째 주제는 생성된 이터븀 겹친 페르미 기체를 이용한 라만 전이의 이중 공명 현상이다. 두 개의 라만 전이가 동시에 같은 원자들에게 공명 조건을 만족하는 이중 공명점에서는, 라만 전이의 스펙트럼이 서로를 교차하지 못하고 밀어내는 모습을 보이며, 이것은 Raman coupling에 의한 light shift를 통해 정량적 설명이 가능하다. 본 연구에서는 라만 전이의 이중 공명이 기존에 제시된 추가적인 rf 전이를 이용하지 않고도 주기적인 스핀-궤도 결합을 구현하는 역할을 함을 논한다. 또한 이 방법을 이용하여 스핀들이 섞여있는 밴드 구조를 조절하는 방법과, 원자들을 단열적으로 밴드 위에 위치시키는 방법을 함께 다룬다.

주요어 : 겹친 페르미 기체, 페르미 양자 기체, 이터븀, 스핀-궤도 결합, 라만 전이

학 번 : 2011-20414